DISSERTATION

# Multi-Directional Crack Model for Cementitious Composites in Consideration of Shear Graveling

せん断による砂利化を考慮したセメント複合体の多方向ひび割れモデル

Central Research Institute of Electric Power Industry

Yuto Yamanoi

Supervisor
Prof. Koichi Maekawa

September 2022

# Table of Contents

## Table of Figures and Tables

## List of Symbols

| Symbol | Description | Commonly used unit |
|---|---|---|
| $\sigma_{ij}$ ; $\varepsilon_{ij}$ | stress and strain tensor | -; - |
| $I_1$ | first invariant of stress tensor, equal to $\sigma_{ii}$ | kPa, MPa |
| $\sigma_\mathrm{m}$ ; $\varepsilon_\mathrm{m}$ | mean principal stress and strain, equal to $\sigma_{ii}/3$ ; $\varepsilon_{ii}/3$ | -; - |
| $\delta_{ij}$ | Kronecker's delta | - |
| $s_{ij}$ ; $e_{ij}$ | deviatoric stress and strain tensor, equal to $\sigma_{ij} - \sigma_m\delta_{ij}$ ; $\varepsilon_{ij} - \varepsilon_m\delta_{ij}$ | -; - |
| $J_2$ ; $J_{2s}$ | Second invariants of deviatoric stress and strain tensor, equal to $\sqrt{\frac{1}{2}s_{ij}s_{ij}}$ ; $\sqrt{\frac{1}{2}e_{ij}e_{ij}}$ | kPa, MPa |
| $J_{3s}$ | third invariant of elastic deviatoric strain tensor, equal to $\sqrt[3]{\frac{1}{3}e_{ij}e_{jk}e_{ki}}$ | MPa |
| $f'_\mathrm{c}$; $f_\mathrm{t}$ | uniaxial compressive and tensile strength | MPa |
| $K, K^\mathrm{m}$ (m $= 0{\sim}6$) | fracture parameter | - |
| $\nu_0$ | initial poison's ratio | - |
| $E_0$ ; $G_0$ ; $K_0$ | initial young's modulus; shear stiffness; volumetric stiffness | GPa, MPa |
| $\varepsilon_\mathrm{peak}$ | uniaxial strain at the compressive strength | |
| $\varepsilon_\mathrm{max}^\mathrm{m}$ | maximum compressive strain experienced along the m-th crack plane | |
| $G_\mathrm{f}$ | fracture energy | N/m |
| $d_\mathrm{max}$ | size of maximum coarse aggregate | mm |
| $L_\mathrm{e}$ | reference length of the finite element | mm |
| $L^\mathrm{ref}$ | reference length on which the constitutive model based | mm |
| $\sigma_{\mathrm{rc}ij}$ | stress tensor calculated by the reinforced concrete model | - |
| $\sigma_{\mathrm{c}ij}$ | stress allocated to concrete | - |
| $\sigma_{\mathrm{r}ij}$ | stress allocated to reinforcement bar | - |
| $\sigma_{\mathrm{s}ij}$ | stress tensor calculated by a perfect elasto-perfect plastic model assuming sand-like materials | - |
| $\sigma_\mathrm{t}$ | uniaxial tensile stress | MPa |
| $\sigma'_\mathrm{l}$ | lateral confining pressure | MPa |
| $\varepsilon_\mathrm{t}$ | uniaxial tensile strain | - |
| $\varepsilon_\mathrm{tu}$ | tensile strain at beginning of the softening | - |
| $\varepsilon_\mathrm{te}$ | upper limit strain for convenience of calculation | - |
| $\varepsilon'_\mathrm{e}$ | equivalent compressive strain normalized by peak strain | - |
| $\gamma_\mathrm{u}$ | ultimate shear strain (engineering strain) | - |
| $c_\mathrm{t}$ ; $c_\mathrm{c}$ ; $c_\mathrm{s}$ | softening parameter for tension, compression and shear | - |

| | | |
|---|---|---|
| $R'_c$ | contact force of a contact unit | MPa |
| $\omega$ | opening width | mm |
| $\delta$ | shear slip | mm |
| $\theta_s$ | direction of the contact stress (0 corresponds to the horizontal plane and $\pi/2$ corresponds to the vertical plane.) | rad, deg |
| $\tau_f$ | shear strength | kPa, MPa |
| $\sigma_n$ | normal stress to the shear plane | kPa, MPa |
| $K_s^c$ ; $K_s^o$ ; $K_n^c$ ; $K_n^o$ | shear and normal stiffness on the joint interface ("c" and "o" mean closure and opening mode) | MPa/m |
| $c$ | cohesion | kPa, MPa |
| $\phi$ | friction angle | rad, deg |
| $\mu$ | coefficient of friction | - |
| $e$ | void ratio | - |
| $\rho_d$ | dry density | ton/m³ |
| $D_r$ | relative density | % |
| $\phi_{res}$ | friction angle at residual strength | rad, deg |
| $p$ | mean confining pressure | kPa, MPa |
| $\varepsilon_p$ | mean strain derived from consolidation evolved by the changes of effective stress | - |
| $\varepsilon_v$ | mean strain derived from dilatancy provoked by shear | - |
| $\varepsilon_{vc}$ | mean strain representing the unrecoverable negative dilatancy | - |
| $\varepsilon_{vd}$ | mean strain representing the recoverable positive dilatancy | - |
| $\varepsilon_{vdp}$ | uniform dilatational strain of the entire reference volume | - |
| $\varepsilon_{vdf}$ | dilatational strain of the shear band | - |
| $J_{2sp}$ | second invariant of the total deviatoric strain at the peak | kPa, MPa |
| $J_{2sf}$ | second invariant of the total deviatoric strain where the dilatancy becomes steady | kPa, MPa |
| $L_{sb}$ | width of the shear band | mm |

Common rule

| | | |
|---|---|---|
| Subscript "e" and "p" | elastic and plastic | - |
| Superscript "ref" | reference value | |
| prime | positive in compression | - |
| d$X$ | incremental form of $X$ | - |
| Suffix "ini" | initial state | - |
| Suffix "lim" | limit state | - |

# 1 Introduction

## 1.1 Damage assessment of concrete structures in ultimate state

It is fresh in our memory that the Great East Japan Earthquake which was an unexpected scale cause a great damage to the civil engineering structures. In Japan, where there are more than 2000 active faults, it is almost impossible to predict all of these movements, so there is a great possibility that unexpected large earthquakes and fault displacements will occur in the future. As we have experienced in the cases of Chernobyl and Fukushima Daiichi, nuclear power plants where one accident can lead to catastrophic damage cannot be tolerated of "unexpected" damage in any case. Nonlinear 3D FEM analysis is one of the powerful tools that can predict the ultimate state of structures and has been used to check the seismic resistance of critical civil engineering structures in nuclear power plants (Japan Society of Civil Engineering, 2021). The sophistication of evaluation methods is still being promoted.

Today, the advanced constitutive model has been developed that can accurately represent complex fractures of reinforced concrete (RC) structures. Basically, it is possible to evaluate the response up to the ultimate state of the RC structure, but there is still room for expansion. For example, concrete is mainly composed of sand and gravel, so as the fracture progresses, its mechanical properties should become similar to the constituent materials. To my best knowledge, there is no numerical model that can take into account such disintegration levels other than fatigue fracture. In order to evaluate the response of the structure until collapse, it is necessary for analytical model to be able to cover these extreme cases. Since numerical models are becoming more sophisticated in each discipline, it is possible to integrate interdisciplinary knowledge to expand the scope of the model. Furthermore, due to the improvement in computing power, large-scale analysis with advanced constitutive model has been recently possible.

## 1.2 Examples of structures outside the scope of existing concrete models

### 1.2.1 Structure made of materials with weak cementation

Artificial soft rocks are sometimes used as ground improvement materials when constructing structures on bedrock. At the Kashiwazaki Nuclear Power Station, low-strength concrete with compressive strength of about 5 MPa, which is called man-made rock (MMR), is placed under some buildings (Kishi, 1995; Kurihara et al., 1994). CSG (Cemented Sand and Gravels) is used for RCC (roller compacted concrete) dam as a cement composite material with similar strength (Fujisawa et al., 2004; Hirose et al., 2003). The old buildings made of the low- strength concrete of 10 MPa or less have also been reported. (Araki, 2016; Taniguchi et al., 2008).

On the other hand, the constitutive model has generally targeted concrete with compressive strength of 15 MPa or more. Therefore, the applicability of low-strength cementitious materials at the time of large deformation has been less verified. In particular, the hardened cement paste phase is crushed in the shear localization band and aggregate interlocking of concrete cracks is broken. At this time, the sensitivity of the shear strength to the confinement changes compared with that of concrete. Similar degradation has been reported for concrete bridge decks under high cycle fatigue loads (Terada et al., 2019). Furthermore, stagnant water on the decks is known to accelerate the graveling of concrete. Then, a model considering the cumulative fatigue damage due to the micro-pore pressure in concrete composite has been proposed similar to the damages of freezing and thawing actions, and the accuracy of predicting the fatigue life of the deck has been improved (Takahashi et al., 2018). It is predicted that disintegration of low-strength concrete will occur even if the number of repetitions is small. In fact, the authors observed graveling of the low-

strength concrete with compressive strength of 8 MPa in the shear band experimentally as described later.

Previously, constitutive modeling for soft rocks and cement improved ground has been proposed (Abdulla and Kiousis, 1997; Hirai et al., 1989; Namikawa and Mihira, 2007; Shen et al., 2019; Sun and Matsuoka, 1999) . And some of them consider the transition of mechanical properties by introducing a parameter representing the damage degree of cementation. (Adachi and Oka, 1995; Desai and Toth, 1996; Yu et al., 1998). The applicable range of these models is limited to uniaxial compressive strength of 2 MPa or less and elasto-plasticity being the basis of the formulation. These models are not sufficient to properly evaluate anisotropic behaviors of structural concrete in which cracks are introduced in multiple directions. These models for the weak strength cementitious materials are workable for geotechnical foundation with higher confinement and less localization but cannot be applied to the structural concrete with less confinement which may cause localization in progress. In order to meet the challenge to simulate the post-peak behaviors, the modeling of the wide applicability is required.

The authors focused on low-strength concrete and proposed a transition model that defines the transient shift from hardened concrete composite to disintegrated graveling (Yamanoi and Maekawa, 2020). By combining the existing concrete model and elasto-perfect plastic model for the granular material according to the damage index of concrete, the transient disintegration of localized shear bands was mechanically modeled in structural analyses.

### 1.2.2 Structure with local weaknesses

In general, RC structures made of homogeneous materials show great anisotropy after occurrence of cracks. In keeping with the fact that cracks are dispersed in the concrete volume due to the presence of reinforcing bars, a constitutive model representing the average behavior of the coupled system of concrete and reinforcement has been proposed (Okamura and Maekawa, 1991). In this model, it is assumed that the non-linearity of the most open cracks dominates the non-linearity of the entire structure even in the multi-directional crack situation. This assumption makes it possible to explicitly calculate the stress of a complex crack field, which is called the active crack method.

However, if the plain concrete subjected to localized large shear deformation is disintegrated into a gravel-like material, such an assumption will no longer hold. In this case, the proposed transition model is expected to be useful. The authors focused on three examples of structures that cause shear deformation locally beyond the scope of the existing concrete constitutive model. First, the Double-Beam Coupling Beam (DBCB) which has been proposed based on the idea of improving the seismic resistance of members by providing local weak parts was targeted. In DBCB, reinforcement cages are arranged in two stages, and the central part is unreinforced. The unreinforced part may absorb the shear deformation, and the upper and lower parts are bent and damaged like double beams (Choi and Chao, 2020). The unreinforced part is subject to model applicability verification.

Second, the masonry structure has a lot of local weakness of mortar joints distributed in a grid pattern. Many analytical models have been proposed to deal with the local deformation of mortar joints (Lourenço et al., 2007). However, these models focus on the nonlinearity of mortar joint and constituent blocks are represented by elastic bodies or nonlinear materials that allow for cracking in one direction. In order to evaluate complicated situation where the slip in mortar joints and failure of component blocks simultaneously occur, the constitutive model of concrete with the multi-directional crack extended to the masonry model. Here, the proposed transition model was applied to the shear transfer model of the cracks in the mortar joint direction.

Finally, attention was paid not only to concrete but also to the crush zone in the bedrock. The fault fracture zone is usually modeled by the joint interface element, but attempts have been made to replace it with a solid element using a transition model. This replacement not only reduces computational cost, but also facilitates mesh discretization.

## 1.3    Purpose and dissertation structure

The purpose of this study is to improve model accuracy for concrete structures in the ultimate state by developing the numerical model which represent the transient characteristics of cracked concrete undergoing graveling in shear and extend its applicability. Consideration of the changes in material properties associated with shear localization is necessary for structural analysis to assess the residual risk beyond design loads. Especially, the occurrence of crushed areas caused by ground rock faults is an important factor in the risk assessment of underground structures during earthquakes.

With these improvements the transition model, the authors hope to have reliable computational modeling to reproduce the post-peak softening of structural concrete. Concrete, mortar, cement-improved soil, artificial soft rock and CSG are being used as major construction materials for building, infrastructures, foundation and dams, and each has its own industrial technology with its definition to assure the quality. And models for performance assessment have been developed almost independently to meet the industrial needs of design and construction management. However, all these are the cementitious composites in view of the material science and technology. In some cases, we encounter engineering difficulty at the boundaries in between different categories.

In this study, it is expected to merge the industrial boundaries between conventional concrete and lower strength construction materials for future progress in line with the cementitious composites. Opening/exploring a way to comprehensively deal with such aspects to meet future needs is another purpose of this study.

As shown in Fig. 1-1, **Chapter 2**, following this chapter, provides the details of the proposed model. In **Chapter 3**, a monotonic loading experiment of multi-layer composites with low-strength concrete was performed and experimental verification was carried out together with the previously conducted experiments (Yamanoi and Maekawa, 2020). In **Chapter 4**, structural experiments involving localized shear bands with normal strength concrete were conducted for further verification of the proposed model with a focus on graveling. Next, **Chapters 5 and 6** show the results of applying the proposed model to masonry structures, and fault crush zones and artificial soft rocks, respectively. Finally, **Chapter 7** presents the conclusions of the entire research and future prospects.
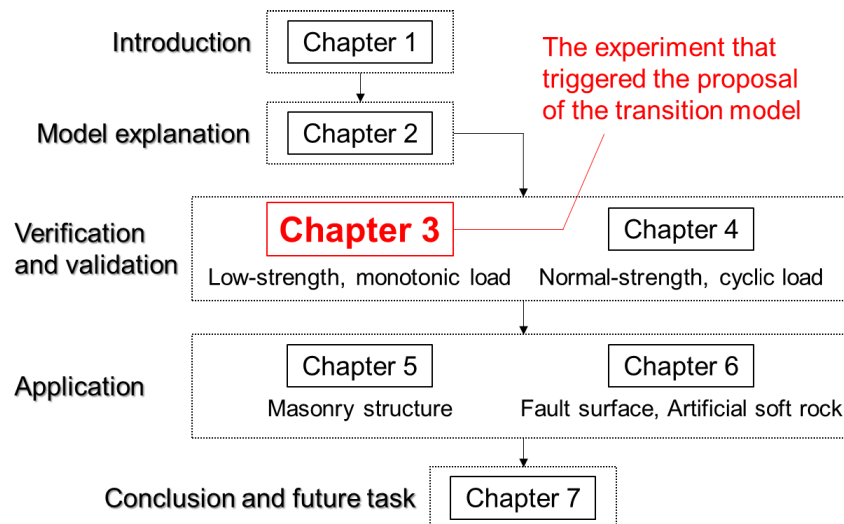
**Fig. 1-1  Dissertation structure**

References of Chapter 1

Abdulla, A.A., Kiousis, P.D., 1997. Behavior of cemented sands - II. Modelling. *International Journal for Numerical and Analytical Methods in Geomechanics 21*, 549–568. https://doi.org/10.1002/(SICI)1096-9853(199708)21:8<549::AID-NAG890>3.0.CO;2-7

Adachi, T., Oka, F., 1995. An elasto-plastic constitutive model for soft rock with strain softening. *International Journal for Numerical and Analytical Methods in Geomechanics 19*, 233–247. https://doi.org/10.2208/jscej.1992.445_9

Araki, H., 2016. Properties of concrete obtained from existing building constructed in 1964, in: *Fourth International Conference on Sustainable Construction Materials and Technologies*. Las Vegas.

Choi, Y., Chao, S.H., 2020. Analysis and design of double-beam coupling beams. *ACI Structural Journal 117*, 79–95. https://doi.org/10.14359/51725985

Desai, C.S., Toth, J., 1996. Disturbed state constitutive modeling based on stress-strain and nondestructive behavior. *International Journal of Solids and Structures 33*, 1619–1650. https://doi.org/10.1016/0020-7683(95)00115-8

Fujisawa, T., Nakamura, A., Kawasaki, H., Hirayama, D., Yamaguchi, Y., Sasaki, T., 2004. Material properties of CSG for the seismic design of trapezoid-shaped CSG dam, in: *13th World Conference on Earthquake Engineering*, Vancouver.

Hirai, H., Takahashi, M., Yamada, M., 1989. An elastic-plastic constitutive model for the behavior of improved sandy soils. *Soils and Foundations 29*. https://doi.org/10.3208/sandf1972.29.2_69

Hirose, T., Fujisawa, T., Yoshida, H., Kawasaki, H., Hirayama, D., Sasaki, T., 2003. Concept of CSG and its material properties, in: *Berga, L., Buil, J., Jofre, C., Chonggang, S. (Eds.), RCC Dams - Roller Compacted Concrete Dams*. Routledge, London, pp. 465–474. https://doi.org/10.1201/9780203741276

Japan Society of Civil Engineering, 2021. *Recommended code and manual for seismic performance verification of outdoor important structures of nuclear power plants*, 2021st ed. JSCE, Japan.

Kishi, K., 1995. Development of artificial soft rock. *Doboku Gakkai Ronbunshu 1995*. https://doi.org/10.2208/jscej.1995.522_45

Kurihara, H., Kikuchi, K., Fukazawa, E., 1994. Experimental study on durability of artificial soft rock. *Doboku Gakkai Ronbunshu 1994*, 85–94. https://doi.org/10.2208/jscej.1994.486_85

Lourenço, P.B., Milani, G., Tralli, A., Zucchini, A., 2007. Analysis of masonry structures: review of and recent trends in homogenization techniques. *Masonry. Canadian Journal of Civil Engineering 34*, 1443–1457. https://doi.org/10.1139/L07-097

Namikawa, T., Mihira, S., 2007. Elasto-plastic model for cement-treated sand. *International Journal for Numerical and Analytical Methods in Geomechanics 31*, 71–107. https://doi.org/10.1002/nag.550

Okamura, H., Maekawa, K., 1991. *Nonlinear Analysis and Constitutive Models of Reinforced Concrete*. Gihodo-Shuppan Co, Japan.

Shen, Z., Jiang, M., Wang, S., 2019. Static and kinematic damage characterization in structured sand. *Acta Geotechnica 14*, 1403–1421. https://doi.org/10.1007/s11440-018-0730-x

Sun, D., Matsuoka, H., 1999. Elastoplastic model for frictional and cohesive materials and its application to cemented sands. *Mechanics of Cohesive-Frictional Materials 4*, 525–543. https://doi.org/10.1002/(SICI)1099-1484(199911)4:6<525::AID-CFM72>3.0.CO;2-X

Takahashi, Y., Tanaka, Y., Maekawa, K., 2018. Fatigue life assessment of initially and time-dependently deteriorated RC decks by data assimilation, in: *The International Federation for Structural Concrete 5th International Fib Congress*.

Taniguchi, H., Yasojima, A., Araki, H., 2008. Seismic performance of reinforced concrete beams with low strength concrete, in: *The 14th World Conference on Earthquake Engineering*, Beijing.

Terada, M., Watanabe, S., Yabu, M., 2019. Study on the influence factor of pavement on deterioration and damage of the deck. *Journal of Japan Society of Civil Engineers, Ser. E1 (Pavement Engineering) 75*, I_201-I_207. https://doi.org/10.2208/jscejpe.75.2_I_201

Yamanoi, Y., Maekawa, K., 2020. Shear bifurcation and graveling of low-strength concrete. *Journal of Advanced Concrete Technology 18*, 767–777. https://doi.org/10.3151/JACT.18.767

Yu, Y., Pu, J., Ugai, K., 1998. A damage model for soil-cement mixture. *Soils and Foundations 38*. https://doi.org/10.3208/sandf.38.3_1

## 2    Transition Model from Concrete to Gravels in Shear

2.1    Different shear transfer mechanism between crack surface of concrete and cohesionless geomaterials

Concrete and sand have different shear resistant mechanisms in the deformed localized bands (Fig. 2-1). The former transmits shear force mainly by the aggregate interlock, and the latter mainly by the contact friction between particles. In the former, the rotation of aggregates is constrained by the cement paste binder, and some analytical models have been proposed based on this mechanism (Bažant and Gambarova, 1980; Tassios and Vintzēleou, 1987; Walraven and Reinhardt, 1981). The contact density model of cracked concrete (Bujadham et al., 1992; Li et al., 1989) is the one where crack surface geometry is stochastically idealized as shown in Fig. 2-2 (a) and (b). In this model, the shear and contact stresses transferred on the crack surface are represented by the integral of the local stresses of the infinite component with different crack angles as following equation.

$$\tau = \int_{-\frac{\pi}{2}}^{\frac{\pi}{2}} R'_\text{c}(\omega, \delta, \theta_\text{s}) \sin\theta_\text{s} \mathrm{d}\theta_\text{s}$$

$$\sigma' = \int_{-\frac{\pi}{2}}^{\frac{\pi}{2}} R'_\text{c}(\omega, \delta, \theta_\text{s}) \cos\theta_\text{s} \mathrm{d}\theta_\text{s} \tag{2-1}$$

where, all symbols conform to Fig. 2-2 (a). In addition to representing the geometric shape of the crack surface with trigonometric functions, it has been assumed that at each contact surface, the frictional force and the elastic components of contact stress can be ignored (Fig. 2-2 (b) and (c)). By these assumptions, each stress expressed by Eq. (2-1) is finally simplified to the following equations and the loading function can be drawn as shown in Fig. 2-2 (d)

$$\tau/m = \frac{\varphi^2}{1+\varphi^2}, \qquad \sigma'/m = \frac{\pi}{2} - \cot^{-1}\varphi - \frac{\varphi}{1+\varphi^2} \tag{2-2}$$

$$\sigma'/m = \frac{\pi}{2} - \tan^{-1}(m/\tau - 1)^{1/2} - \frac{(m/\tau - 1)^{\frac{1}{2}}}{m/\tau} \tag{2-3}$$

where, $\varphi = \delta/\omega$; $m = 3.83 f'^{1/3}_\text{c}$ [MPa]. Prime means that the compression is positive. Here, it should be noted that the ultimate maximum shear strength is determined by the material constant expressed as a function of compressive strength. Moreover, the confinement stress when the shear strength reaches the maximum one is about 1.57 times the shear strength. As a result, the confinement effect on shear transfer along concrete cracks may be comparatively lower than that of sand particle assembly when the confinement is higher and maximum shear strength is lower.

For sand-like granules, many fracture problems have been solved according to the Mohr-Coulomb equation below.

$$\tau_\text{f} = c + \sigma'_\text{n} \tan\phi \tag{2-4}$$

where, $\tau_\text{f}$ and $\sigma_\text{n}$ are the shear strength and normal stress to the fracture plane; $c$ and $\phi$ are the cohesion and friction angle. There is almost proportional relationship between restraint pressure and shear strength, and elasto-plastic constitutive models that follow the Mohr-Coulomb or Drucker-Prager failure criteria fit well. In this equation, soil is regarded as a frictional material, and shear failure is mainly assumed. This assumption makes sense if the aggregate does not shatter and can rotate freely. However, it has also been reported that the confinement dependency of strength and stiffness changes when sand undergoes chemical cementation (Shibuya et al., 2001). This study focused on the transition of shear transfer characteristics between two different mechanisms associated with the failure of chemical cementation.
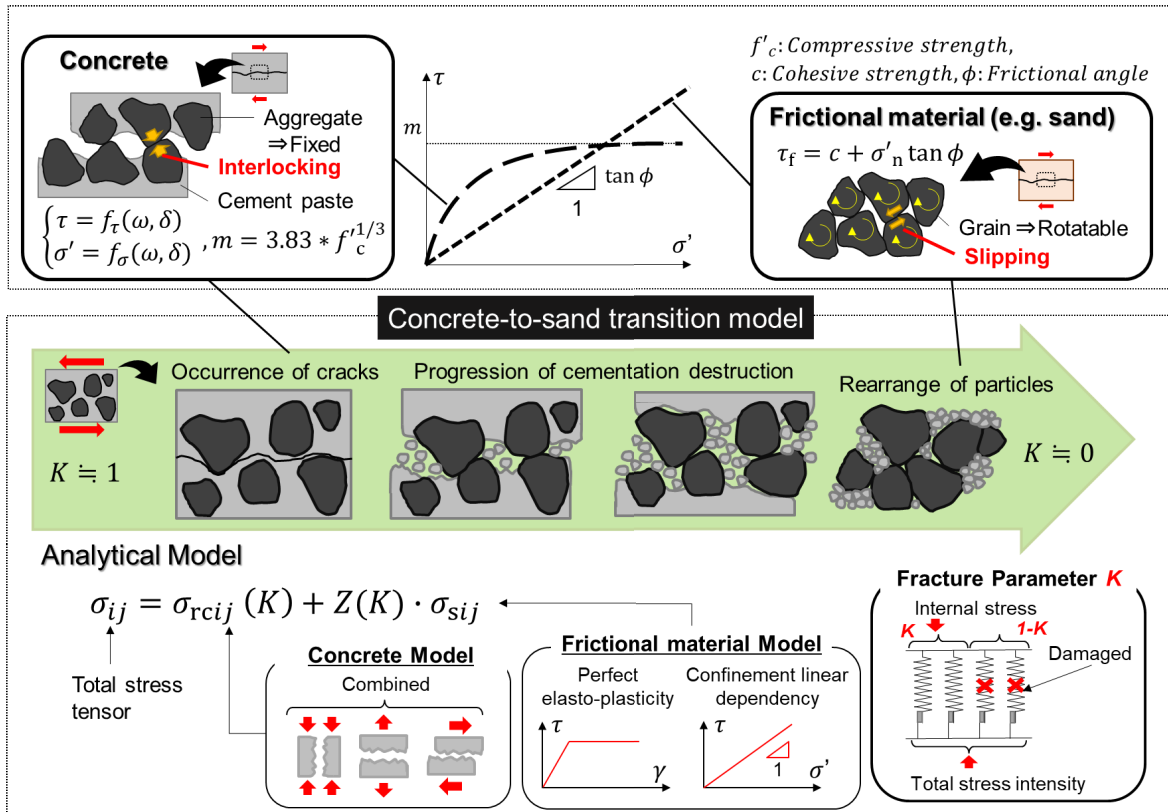
**Fig. 2-1  Outline of modeling over the ultimate state of concrete under shear**



(a)  Geometry of concrete crack surface

(b)  Contact density function



(c)  Constitutive model for the contact stress

(d)  Confinement dependency
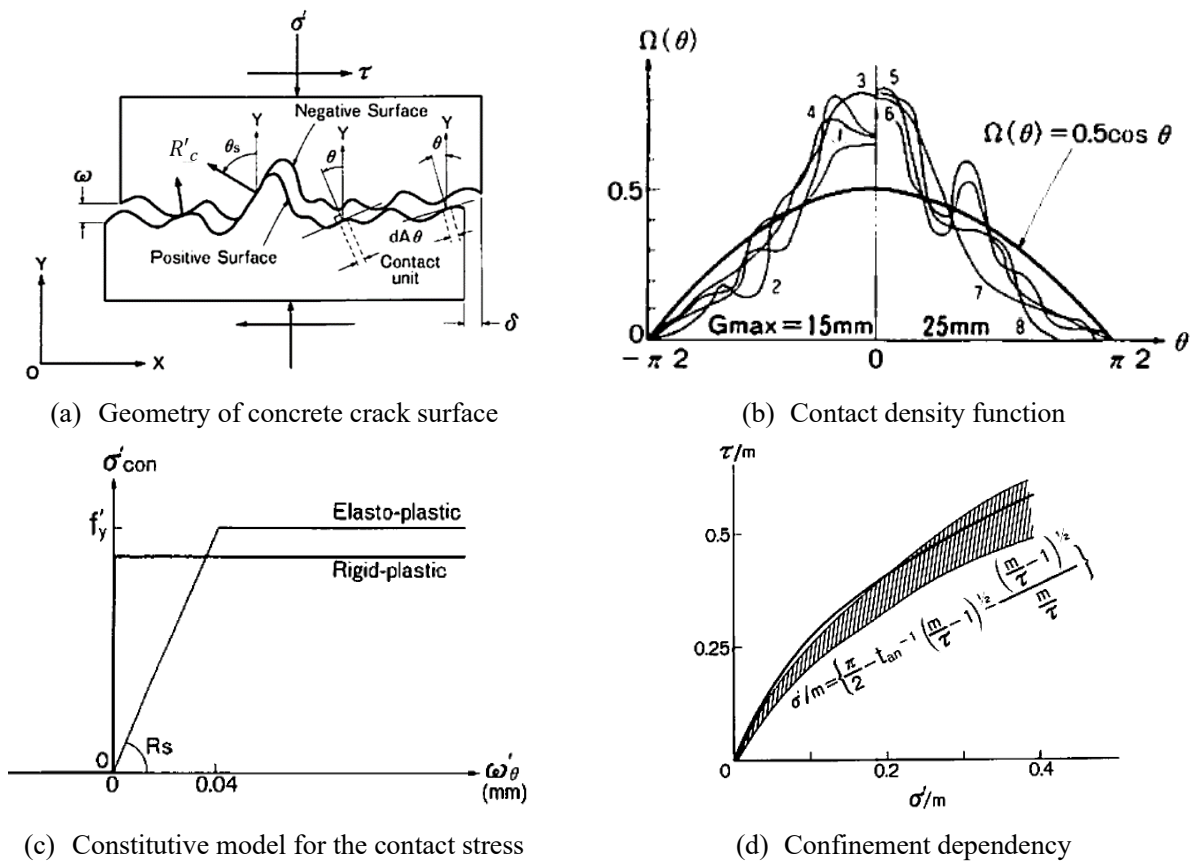
**Fig. 2-2  Contact density model representing shear transfer on the crack surface** (Li et al., 1989)

## 2.2 Advanced constitutive model of concrete with multi-directional cracks

At present, an advanced concrete constitutive model that can consider cracks in up to 6 directions has been developed (Maekawa and Fukuura, 2013), and is adopted as the framework of the proposed model. This model calculates the spatially averaged stress of plain or reinforced concrete element according to the cracking state as shown in Fig. 2-3. Before cracking, the 3D elasto-plastic fracture model based on the continuum mechanics is adopted for the uncracked concrete (Maekawa et al., 2003). After cracking, since the anisotropy due to cracking is strong, the stress of cracked concrete is calculated based on the crack coordinate system, which can be regarded as a modified stress method in a broad sense (Tobita et al., 2003). In order to deal with multi-directional crack condition, the active crack method has been proposed. Even if cracks intersect in multiple directions, most non-linearity is assumed to be concentrated in cracks with wide openings since the shear rigidity on the crack surface is highly dependent on the crack width. In the original active crack method, the local crack axis that governs the non-linearity is selected according to the strain state, and the slippage of cracks in other directions is ignored (Okamura and Maekawa, 1991). This method has been extended to allow for more cracks in 3D stress fields by Maekawa and Fukuura (2013).

As shown in Fig. 2-4, first crack axis is introduced when the maximum principal stress calculated by the 3D elasto-plastic fracture model exceeds the tensile strength for the first time. The x-axis is assigned to the maximum principal stress direction, which is the normal direction of the cracked surface, and the y-axis is assigned to the second principal stress direction. The z-axis is determined by the cross product of the vectors of both axes, and then the first crack coordinate system is defined. The stress of cracked concrete is obtained by combining the plane stress model of uncracked concrete in the y-z plane, the compression / tension model in the x direction (normal to the cracked surface), and the shear transfer model in the x-y and z-x directions as indicated in Fig. 2-3. The compressive stress-strain model used for cracked concrete is described in reference to the transverse tensile strain normal to the compressive principal stress axis in order to express the decay of compression load-carrying mechanism due to the widened crack opening (Miyahara et al., 1988; Vecchio and Collins, 1986).

If more than one cracks occur, the multi-directional crack model shown in Fig. 2-5 is activated. A new crack plane is introduced when the angle between the principal stress axis and all existing cracked axes is greater than a certain angle (22.5 deg). The crack axis vectors up to 6 directions are stored individually, and 3 cracks that are close to orthogonal are associated as one crack coordinate system as illustrated in Fig. 2-4. First, the active crack is selected based on the crack opening strain (Fig. 2-5 (b)), and the x-axis is assigned to the active crack axis. As with the first crack, the y-axis is assigned in the direction of the second principal stress and the z-axis is determined accordingly. The coordinate system including the active crack axis is defined as the active crack coordinate system, and the non-linearity of the crack corresponding to the y and z axes is also taken into consideration. Here, it is noted that since the y and z-axis directions do not always exactly match the normal vectors of the corresponding crack planes, these crack directions are not strictly considered. The cracked concrete stress is calculated from the spatially averaged RC constitutive model with quasi-orthogonal bi-directional cracking as shown in Fig. 2-6 (Maekawa et al., 2003).

16
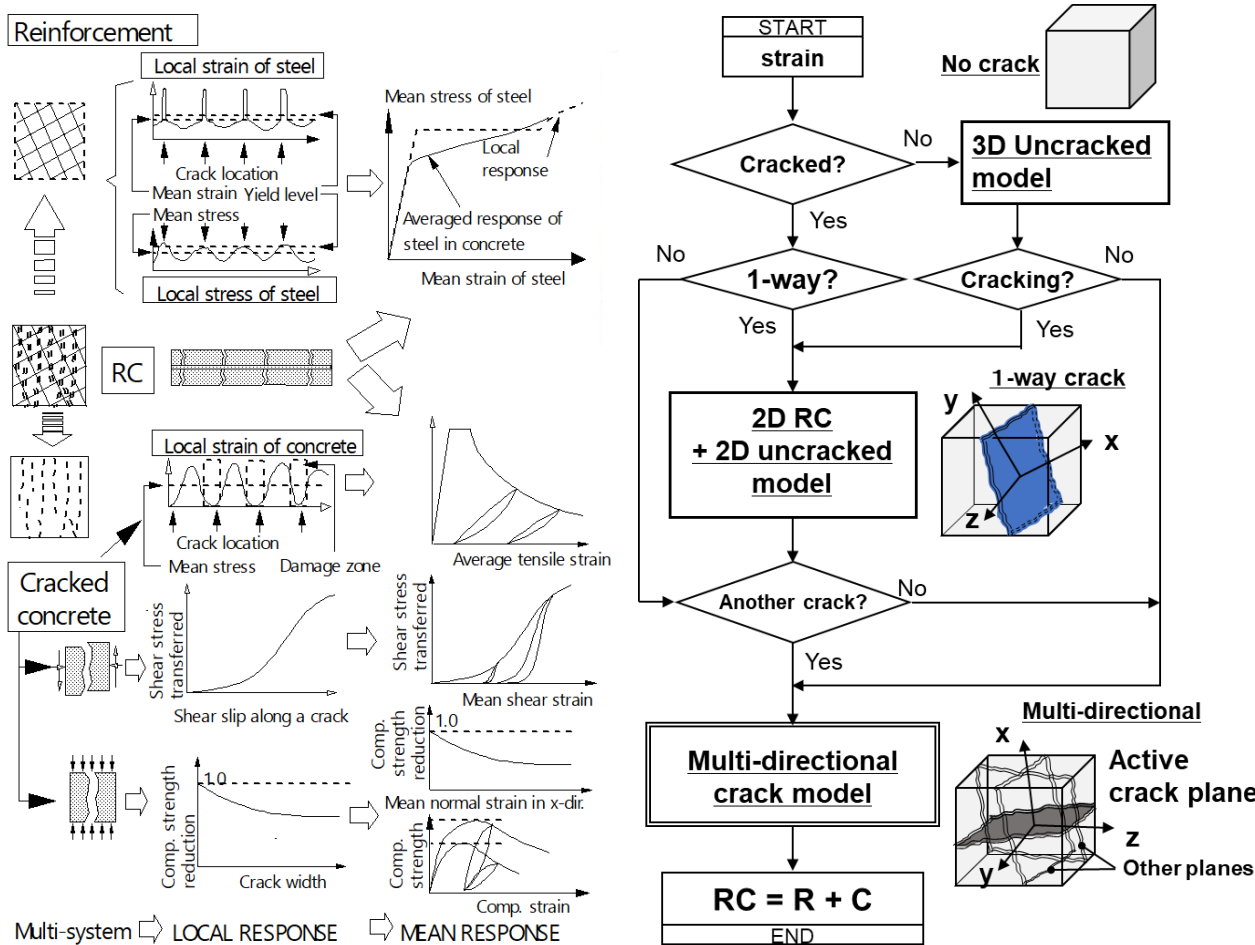
(a) Spatially averaged RC element stress      (b) Stress calculation flow

**Fig. 2-3    Overview of the advanced RC model** (Maekawa et al., 2003)
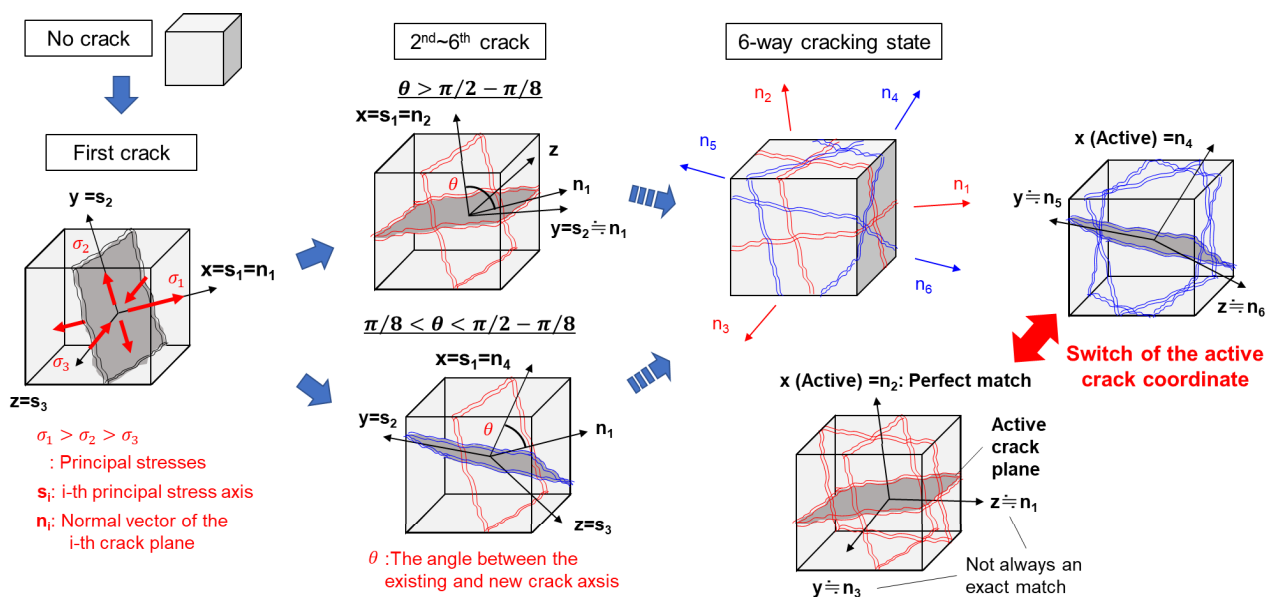


**Fig. 2-4    Multi-directional crack within the reference volume**

## Multi-directional crack model

**Strain and present active crack**

**Judgement of active crack based on the normal strain**

Calculation of the stress based on the active crack-coordinate

**New crack ?** — No

Yes

Setting of new crack plane

*1

**Judgement of active crack based on the normal stress**

Yes *1

**Is active crack changed ?** — No

**Stress of the multi-directional cracked concrete**

*1: Only once in one iterative calculation

(a) Algorithm for stress calculation of multi-directional cracked concrete

$X_c$  $Y_c$  $Y_c$  $X_c$

$\varepsilon_2$  $\varepsilon_1$  Switch of active crack  $\varepsilon_2$  $\varepsilon_1$

$\varepsilon_1 > \varepsilon_2$  $\varepsilon_1 < \varepsilon_2$

RC shear wall under cyclic loading
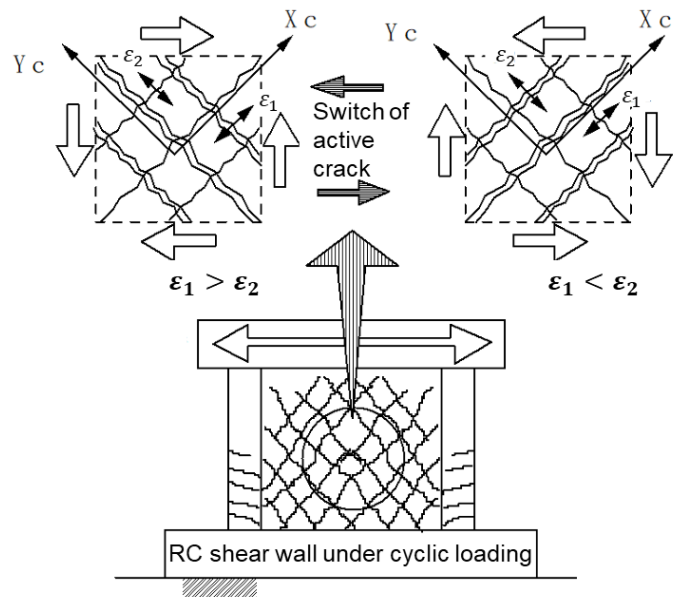
(b) Selection of active crack based on the tensile strain

**i) When active crack is under loading**

Active crack | $(\varepsilon_{tmax,0}, \sigma_{tmax,0})$:

$\sigma_{t,1}$

$\sigma_{tmax,0}$

$\sigma_{n,1} = \sigma_{tmax}$

$\varepsilon_{t,1}$

$\varepsilon_{tmax,0}$  $\varepsilon_{t,1} = \varepsilon_{tmax}$

Largest strain experienced and corresponding stress

loading => No shift of active crack plane
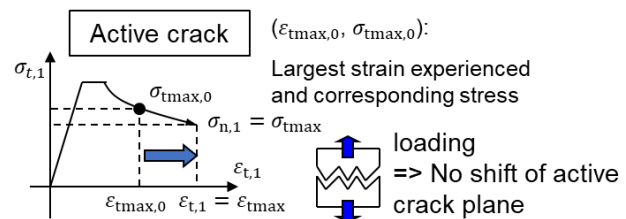
**ii) When active crack is not under loading**

i-th crack

$\sigma_{t,i}$

$\sigma_{n,i}$

$\sigma_{tmax,0}$

$\sigma_{n,i}$

$\varepsilon_{tmax,0}$  $\varepsilon_{t,i}$

loading =>active crack shift

un/re-loading => No shift of active crack plane
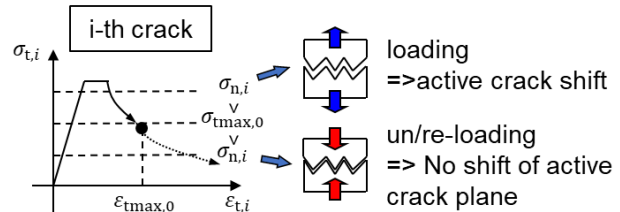
(c) Selection of active crack based on the tensile stress

**Fig. 2-5  Multi-directional crack model based on the active crack method** (Maekawa et al., 2003)

The stress calculated based on the active crack coordinate system is converted into the stress in the normal direction of each crack plane, and the active crack is re-judged according to the loading condition as shown in Fig. 2-5 (c). If a new crack occurs or the active crack axis changes, the stress is recalculated only once during one iterative calculation as indicated in Fig. 2-5 (a). This method makes it possible to reproduce the complex mechanical behavior of cracked concrete while ensuring good convergence and practical accuracy as illustrated in Fig. 2-7.

For ordinary concrete structures, there is almost no need to consider cracks in more than 6 directions, but it is not sufficient when concrete is crushed into gravels (in a sense, there are cracks in infinite directions). The transition model was devised to cope with low-strength concrete with weak cement paste bonding force and cases where

18

fracture progresses locally in weak parts of the structure.
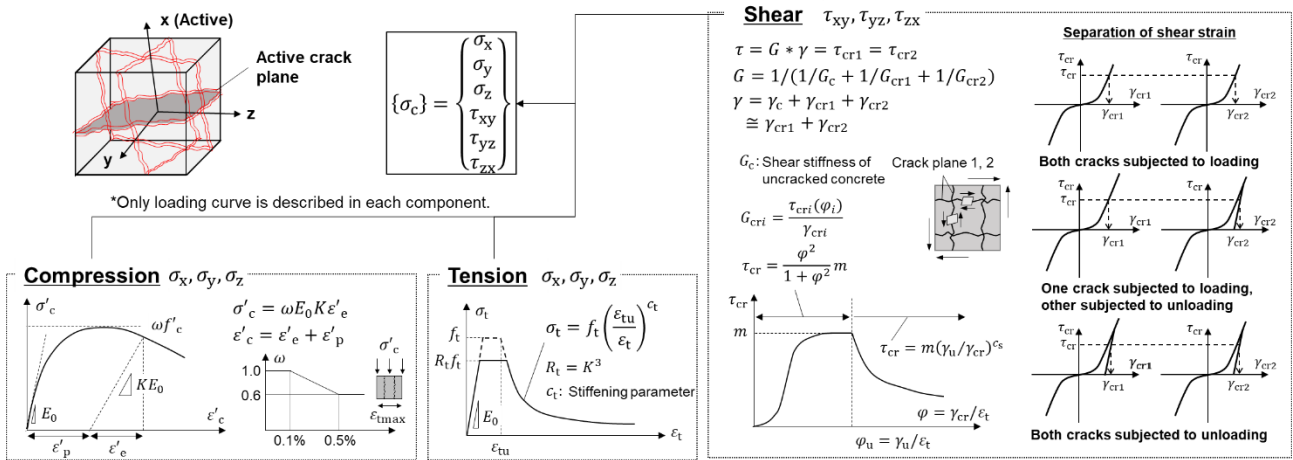


**Fig. 2-6    Calculation of cracked concrete stress based on the active crack**
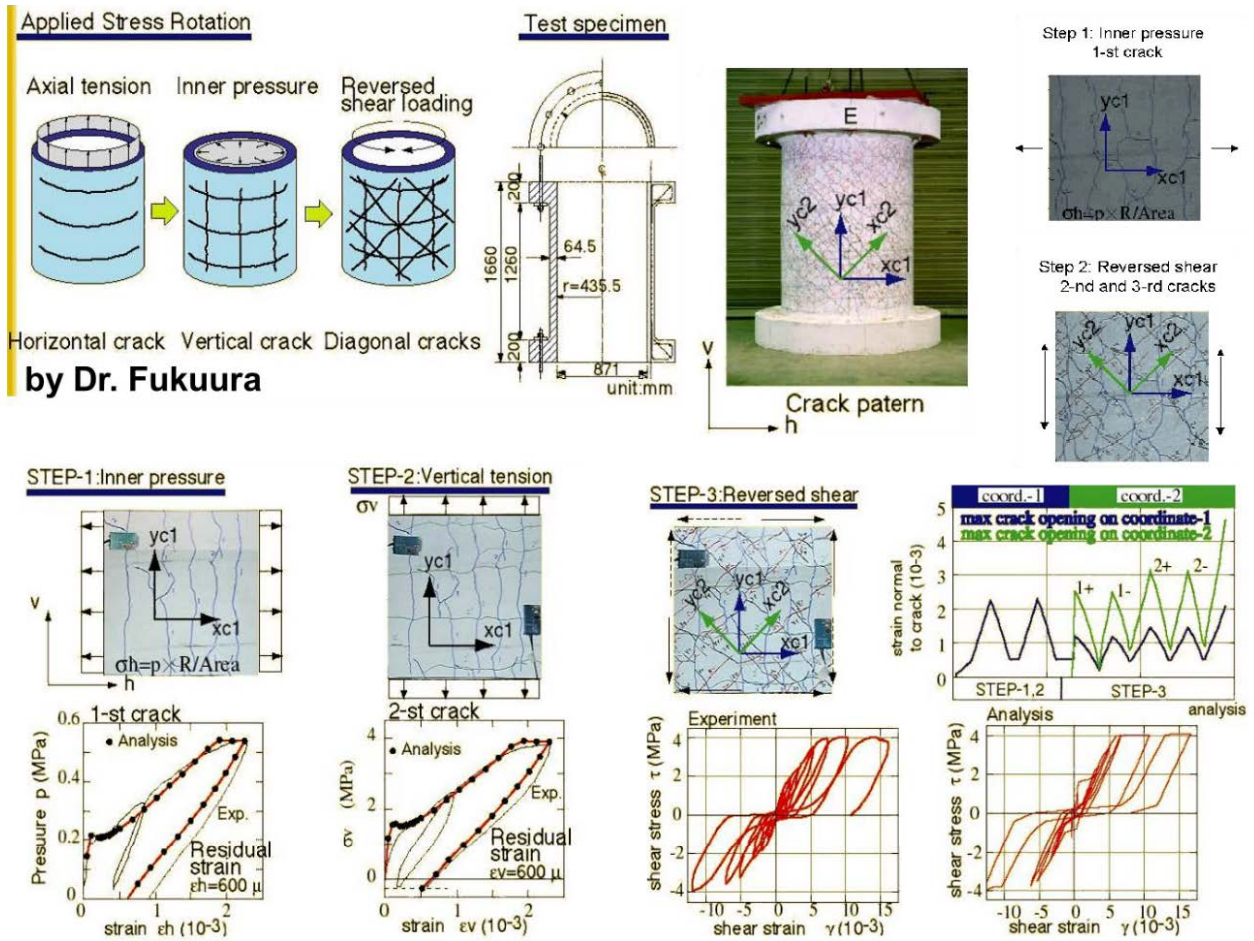


**Fig. 2-7    Verification of the multi-directional fixed crack model** (Maekawa and Fukuura, 2013)

## 2.3 The proposed transition model

As mentioned above, the difference in shear transfer mechanism is thought to be due to the degree of suppression of aggregate rotation in the progressive shear band. When concrete is deteriorated to disintegrated graveling, the rotational restraint of the aggregate is loosened at particle-to-particle contact accompanying the damage of cement paste, and the concrete composite is brought closer to the granular particles (Maekawa and Fujiyama, 2013). The transition model is formulated based on this idea (Yamanoi and Maekawa, 2020). In this model, the total stress tensor $\sigma_{ij}$ of the localized bands is expressed as,

$$\sigma_{ij} = \sigma_{rcij}(K) + Z(K)\sigma_{sij}, \qquad \sigma_{sij} = s_{ij} + \sigma_m \delta_{ij} \qquad (2-5)$$

where $\sigma_{rcij}$ is the stress tensor yielded by constitutive model for cracked and uncracked concrete introduced in the former section; $\sigma_{sij}$ is the stress yielded by an elasto-perfect plastic model assuming sand; $s_{ij}$ is the deviatoric stress tensor; $\sigma_m$ is the mean stress; $\delta_{ij}$ is Kronecker's delta; $K$ is a fracture parameter calculated in the original concrete model to indicate the residual shear-mode elasticity, which is equivalent to the remaining volume conserving the shear elastic energy after damage as shown in Fig. 2-8 (a).

Regarding the volumetric elasticity of uncracked concrete, no damage is assumed and the whole volume of concrete is idealized to be able to conserve the volumetric elastic energy under isotropic compression. In the multi-directional cracking state, where the stress is calculated based on the local crack coordinate system, the compressive normal stress along the crack plane is calculated by assuming the uniaxial condition due to stress release in the orthogonal direction. This idealization follows the compression field theory (Vecchio and Collins, 1986). In this state with strong anisotropy, the concrete fracture reduces both apparent volumetric and shear stiffness. Details of the equations in Fig. 2-8 are given in **Appendix A**. As a whole, the parameter $K$ in Eq. (2-5) is the damage representative in the mode of shear to resist against the change of shape. $Z(K)$ is a function that expresses the degree of transition. The two extreme states, the no damaged state and the completely disintegrated state, are linearly interpolated as shown in Eq. (2-6).

$$Z(K) = 1 - K \qquad (2-6)$$

The algorithm for calculating stress is shown in Fig. 2-9. Before cracking where concrete is primally in compression, fracture parameter denoted by $K$ is computed by empirical equation (Eq. (2-7)) (Maekawa et al., 2003). In this case, some tension whose stress is less than the tensile strength may develop, but it is within elasticity. Then, the strain invariant denoted by $E$, which express the shear elastic intensity, is used for estimating the fracture parameter as expressed by Eq. (2-8), where the volumetric first invariant is used to consider the effect of confinement on the evolution of damage.

$$K^0 = \exp\left[-\frac{E}{3.25}\left\{1 - \exp\left(-\frac{E}{0.8}\right)\right\}\right] \qquad (2-7)$$

$$E = \frac{\sqrt{2}J_{2es}}{0.23\varepsilon_0 + \sqrt{3}|\varepsilon_{em}|}\left(\frac{6 + \cos 3\theta}{5}\right) \qquad (2-8)$$

$$\varepsilon_0 = 1.6(1 + \nu_0)\frac{f'_c}{E_0} \qquad (2-9)$$

$$\cos 3\theta = \frac{2\sqrt{3}}{2}\left(\frac{J_{3es}}{J_{2es}}\right)^3 \qquad (2-10)$$

where $K$ in Eq.(2-5) is equal to $K^0$ of the parameter before cracking; $\varepsilon_{em}$ is the mean elastic strain and equal to $\varepsilon_{eii}/3$; $J_{2es}$ and $J_{3es}$ are the second and third invariant of elastic deviatoric strain tensor; $\nu_0$, $f'_c$ and $E_0$ are the initial poison's ratio, uniaxial compressive strength and initial Young's modulus, respectively. The sound state of no damage corresponds to $K = 1$ where the entire volume can conserve the shear elastic energy, and the damage transition up to the graveling is complete at $K = 0$. where the shear elasticity is lost and only the volumetric elasticity remains. This state corresponds to the complete loss of cementation by hydrated cement paste in concrete composite.

After cracking, however, tensorial invariants cannot be used because of strong anisotropy which depends on crack-orientation. Then, the non-orthogonal multi-directional crack plane model is applied (Maekawa and Fukuura, 2013). Here, the fracture parameter for each crack plane is computed just based upon the compressive stress-strain path along its plane as illustrated in Fig. 2-9. The minimum value of the fracture parameters of developing multi-planes denoted by $K^m$ is used as the referential parameter of damage as expressed by Eq. (2-11).

$$K^m = \exp\left[-0.73\frac{\varepsilon_{max}^m}{\varepsilon_{peak}}\left\{1 - \exp\left(-1.25\frac{\varepsilon_{max}^m}{\varepsilon_{peak}}\right)\right\}\right], \qquad m = 1\sim6 \qquad (2-11)$$

where multi-directional non-orthogonal crack planes are accepted up to 6, $\varepsilon_{peak}$ is the uniaxial strain at the compressive strength and $\varepsilon_{max}^m$ is the maximum compressive strain experienced along the m-th crack plane.

The transition of volumetric stiffness according to the concrete fracture is shown in Fig. 2-8 (b). As fracture progresses, the contribution of gravels to volumetric stiffness increases. The total volumetric stiffness gradually decreases because the stiffness of the assembly of gravels is usually lower than that of sound concrete. Strictly speaking, as concrete fracture progresses without discrete cracks, an increase in total volumetric stiffness occurs. The rigidity of the geomaterial increases due to the solidification associated with the negative dilatancy. This phenomenon has also been reported in concrete. By applying the transition model, it becomes possible to qualitatively consider the increase in volume stiffness due to consolidation, which was not considered in the previous model. Although its quantitative validity has not been guaranteed, it was judged that it would not have a significant effect on the analysis results because it can be regarded as a rare situation that structural concrete undergoes the fracture without any cracks. And a simple model that does not consider the crack situation has been adopted. When applying this model to rocks that are subject to large confining pressure, it may be necessary to improve the transition of volume stiffness under triaxial compressive stress.

As is clear from Fig. 2-8, the shear rigidity of concrete decreases monotonically with the progress of fracture, and the contribution of gravel increases. The magnitude relation of the shear rigidity of the cracked concrete and gravels largely depends on the confining pressure and the fracture level.

This approach makes it possible to represent the highly anisotropic damage of concrete under the multi-directional cracking states and to reasonably integrate it with the post-graveling model of isotropy. In other words, if the stiffness would be solely and phenomenologically modeled based upon the isotropic model for soil, the anisotropic damage of the graveling concrete cannot be identified logically. This logic from anisotropy to isotropy of damage information is the original point of the proposed model, and the authors could not find related references.

## Fracture parameter $K$

: Represents the remaining volume which may conserve the shear elastic energy after damage
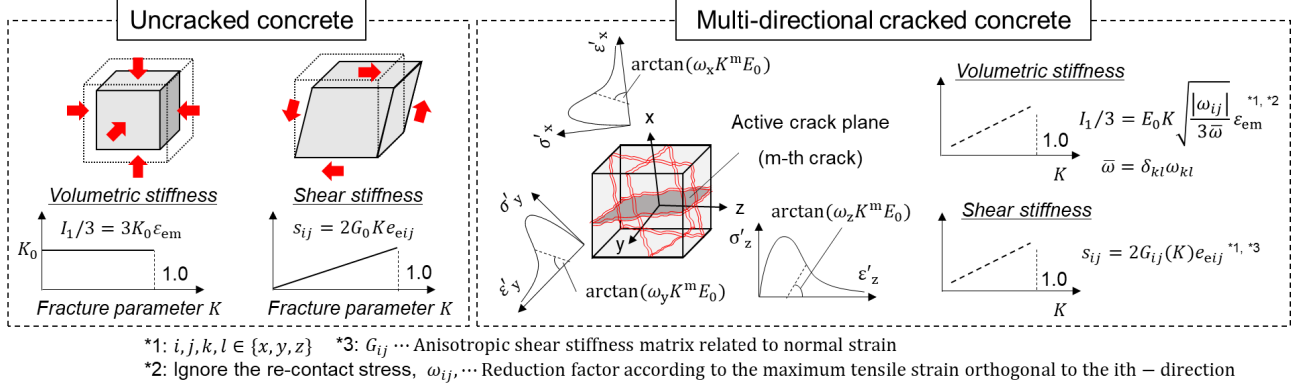


(a) Relationship between the fracture parameter and stiffness in the original model
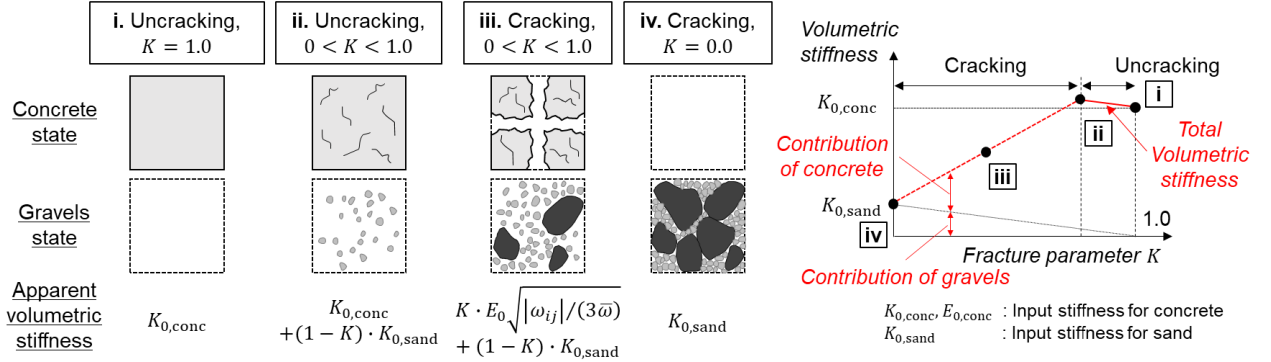


(b) Transition of volumetric stiffness according to the fracture parameter and cracking state

**Fig. 2-8   Relationship between the fracture parameter and stiffness**

The stress component of disintegrated graveling ($\sigma_{sij}$) is obtained by elasto-plastic modeling for soil foundation. Assuming isotropy, the stress increment is expressed by a combination of deviatoric and volumetric components as,

$$\mathrm{d}\sigma_{sij} = 2G_0\mathrm{d}e_{eij} + 3K_0\delta_{ij}\mathrm{d}\varepsilon_{em} \qquad (2-12)$$

where, $G_0$ and $K_0$ are the initial shear and volumetric stiffness, respectively; $e_{eij}$ is the elastic deviatoric strain tensor and equal to $\varepsilon_{eij} - \varepsilon_{em}$; $\varepsilon_{em}$ is the elastic mean volumetric strain and equal to $\varepsilon_{eii}/3$. In this study, plastic flow normal to the deviatoric plane of stresses and Drucker-Prager's yield criterion is adopted. The mathematical form of yield surface is show in Eq. (2-13). Since large shear deformation has developed when the graveling disintegration had proceeded, the authors may assume similar to the geomaterials that further dilatancy does not progress after the completed transition to graveling.

$$F = J_2 - S_u = J_2 - A + BI_1, \qquad J_2 = \sqrt{\frac{1}{2}s_{ij}s_{ij}}, \qquad I_1 = 3\sigma_m \leq 0 \qquad (2-13)$$

where, $A, B$ are constants of the largest yield surface; $\varepsilon_{ij}$ is the total strain tensor. $\sigma_m$ is calculated based on the mean strain of concrete as $K_0\varepsilon_{cii}$. In the case of dry sand particle assembly, parameters $A$ and $B$ specify the yield surface decided based upon the cohesive strength denoted as c and the internal friction angle denoted as $\phi$. Thus, the

simple model, $A = c = 0$ and $B = \tan\phi/3 = \mu/3$ ($\mu$: frictional coefficient), was adopted. The set yield surface approximately circumscribes the Mohr-Coulomb yield surface on the plane perpendicular to the hydrostatic pressure axis.

In the elastic state (that is, satisfying $F(J_2) < 0$, the stress can be obtained by using the relation of $e_{eij} = e_{ij}$. In the elastic-plastic state, the flow rule and consistency conditions are expressed by the following equations based on the elasto-plastic theory.

$$de_{\mathrm{p}ij} = d\lambda \cdot \frac{\partial F}{\partial \sigma_{sij}} = d\lambda \cdot \frac{s_{ij}}{2J_2} \qquad Flow\ rule \qquad (2-14)$$

$$dF(J_2) = d(J_2 - S_{\mathrm{u}}) = dJ_2 = 0 \qquad Consistency\ condition \qquad (2-15)$$

where $e_{\mathrm{p}ij}$ is the plastic deviatoric tensor; $d\lambda$ is the plasticity evolution scalar and derived from the combination of the consistency condition and the relation of $de_{eij} = de_{ij} - de_{\mathrm{p}ij}$.

$$2J_2 dJ_2 = d(J_2)^2 = s_{ij} ds_{ij} = 0 \quad \because dJ_2 = 0$$

$$\therefore \frac{s_{ij} ds_{ij}}{2G_0} = s_{ij}(de_{eij}) = s_{ij}(de_{ij} - d\lambda s_{ij}/2J_2) = 0 \quad \because ds_{ij} = 2G_0 de_{eij}$$

$$\therefore d\lambda = \frac{s_{ij} de_{eij}}{J_2} \quad \because s_{ij}s_{ij} = 2J_2^2,\ J_2 = S_{\mathrm{u}} \qquad (2-16)$$

By combining Eq. (2-12) and (2-16), the incremental elasto-plastic stress is expressed as:

$$d\sigma_{sij} = 2G_0 \left( de_{ij} - s_{ij} \frac{s_{kl} de_{kl}}{2S_{\mathrm{u}}^2} \right) + 3K_0 \delta_{ij} d\varepsilon_{\mathrm{m}} \qquad (2-17)$$

The strain softening of reinforced concrete (RC) accompanying the deformational localization in finite elements is considered in tension (An et al., 1997), shear transfer (Li et al., 1989) and compression (Maekawa and El-Kashif, 2004) perpendicular to and along crack planes. Here, the softening is described by the spatial averaged constitutive model in accordance with the element size in order to have the consistency of fracture energy (Maekawa et al., 2003; Maekawa and Fukuura, 2013). On the other hand, the elasto-perfect plasticity modeling to represent the graveling state after the shear deterioration assumes isotropy with non-localized nature. Therefore, the size-dependency is not considered in this stage, and it changes gradually according to the damage evolution from RC to granular disintegrated graveling. The validity of this assumption is discussed in later section.

**INPUT: Strain $\varepsilon_{ij}$**

Original concrete model developed by Maekawa et al., (2003)

Is there crack ?

Yes — No

**3D EPF model of concrete before cracking**

$$K^0 = \exp\left[-\frac{E}{3.25}\left\{1 - \exp\left(-\frac{E}{0.8}\right)\right\}\right]$$

where $E = f(\varepsilon_{em}, J_{2es}, J_{3es})$

**Cracked concrete model** developed by Maekawa and Fukuura (2013)

$$K^m = \exp\left[-0.73\frac{\varepsilon_{max}^m}{\varepsilon_{peak}}\left\{1 - \exp\left(-1.25\frac{\varepsilon_{max}^m}{\varepsilon_{peak}}\right)\right\}\right]$$

where m = 1~6: crack number

Compression and tension

$\sigma_x, \sigma_y, \sigma_z$
$\varepsilon_x, \varepsilon_y, \varepsilon_z$

Shear transfer

$\tau_{xy}, \tau_{yz}, \tau_{zx}$
$\gamma_{xy}, \gamma_{yz}, \gamma_{zx}$

$\tau = G * \gamma$
$G = 1/(1/G_c + 1/G_{cr1} + 1/G_{cr2})$

Crack plane 1, 2

$\sigma_{rcij}, \varepsilon_{rcij}$
$K = \text{MIN}(K^0, K^1, \cdots, K^6)$

**Calculation of stress $\sigma_{sij}$**

$$F = J_2 - A + BI_1, \qquad J_2 = \sqrt{\frac{1}{2}s_{ij}s_{ij}}, \qquad I_1 = 3\sigma_m$$

$$d\sigma_{sij} = 2G_0\left(de_{ij} - s_{ij}\frac{s_{kl}de_{kl}}{2S_u^2}\right) + 3K_0\delta_{ij}d\varepsilon_m$$

**Transition model**

**Combined stress**

$$\sigma_{ij} = \sigma_{rcij}(K) + (1 - K)\sigma_{sij}$$

**OUTPUT: Stress $\sigma_{ij}$**

**Fig. 2-9　Algorithm for calculating stress**

## 2.4　Identification of the ultimate frictional coefficient in the proposed model

(1) Previous shear tests of concrete

The transition model is established on the assumption that the dominant shear transfer mechanism in post-gravelized concrete is frictional force. Here, the cohesion and friction coefficient under the perfectly disintegrated condition are the most important parameters. The push-off test is often adopted to investigate the shear transfer on the crack surface of concrete or joint interface (Mattock and Hawkins, 1972; Resende et al., 2021; Walraven and Reinhardt, 1981; Yang et al., 2012). The main focus of these studies is on pre-peak shear transfer mechanism and characteristics such as the shear strength, confinement dependency, dilatancy, dowel resistance. Residual shear resistance in the ultimate state is mentioned in limited studies. (Kang et al., 2017; Lim et al., 1987; Rahal et al., 2016).

Lim et al., (1987) distinguished ultimate shear strength and residual shear strength into the different shear transfer mechanics. The former is called "Continuum Mechanics" and the latter is called "Stable Discontinuous Mechanics (Friction)". They proposed the analytical model based on the similar concepts to the transition model and conducted push-off test with no stirrups across the shear plane to verify its validity (Fig. 2-10 (a)). As a result, the cohesion and friction coefficient under the stable condition after the ultimate shear strength were idealized to 0 and 1.0, respectively. Rahal et al., (2016) investigated both ultimate and residual strength of normal and self-compacting concrete. They compared the experimental result with the value calculated by various analytical equation (Fig. 2-10 (b)). In their study, it was concluded that the residual strength can be evaluated regardless of the type of concrete by a friction model in which the adhesive force is ignored, and the friction coefficient is set to 1.0. A similar tendency can be seen in the experiments by Kang et al., (2017). It should be noted that in the latter two cases, the residual strength of the shear plane in the experiment also includes the dowel resistance of the reinforcing bar.

(2) Identification of the ultimate frictional coefficient

Fig. 2-10 (c) shows an example of the finite element discretization of the push-off test. Fig. 2-11 (a) shows the shear strength normalized by uniaxial compressive strength. The maximum shear strength is about 1/10 of the uniaxial compressive strength under no confinement, and the increment of the capacity is almost proportional to the confinement pressure. The computed nominal strength by the concrete constitutive model used and the tested strength before disintegration are almost the same. Focusing on the residual shear strength, the adhesive strength becomes zero, and the restraining effect on the residual shear strength is clarified.

The maximum shear strength before disintegration can be evaluated by the existing model, and it is confirmed that the transition model is required in considering the residual strength characteristics for post-peak analysis as shown in Fig. 2-11 (b). Here, the residual shear strength calculated by the post-peak analysis is the stress when the shear slip has progressed to about 10 mm. The average coefficient of friction in the graveling state varies from 1.0 to 0.6 depending on the experiment. In this study, the disintegrated graveling friction in the shear localization bands is tentatively set to 1.0, and subsequent verification will be conducted. An example of a difference in analysis results with and without consideration of concrete graveling is shown in Fig. 2-12. It is clear that the difference between the transition and non-transition model appears in the post-peak behavior.

Next, the average coefficient of friction of mortar is discussed. According to the experimental one case result shown in Fig. 2-11, it seems to match that of concrete. However, the number of cases is too small to judge its validity. When it comes to other materials, it has been reported that the post-peak internal friction angle of sand is about 30 to 35 degrees (Rowe, 1962; Schanz and Vermeer, 1996), which corresponds to a friction coefficient of 0.6 to 0.7. On the other hand, in the case of clay with a large amount of fine particles, the friction angle is about 10 degrees ($\approx$ friction coefficient 0.20: (Skempton, 1985)). The internal friction angle increases as the particle size distribution increases (Miura et al., 1990). Since the disintegrated graveling with crushed cement powder may be between pure sand and silt, the authors set 0.4 for the average friction coefficient of the mortar in the shear localization region.



(a) Test specimen of Lim et al., (1987)

(b) Test specimen of Rahal et al., (2016)
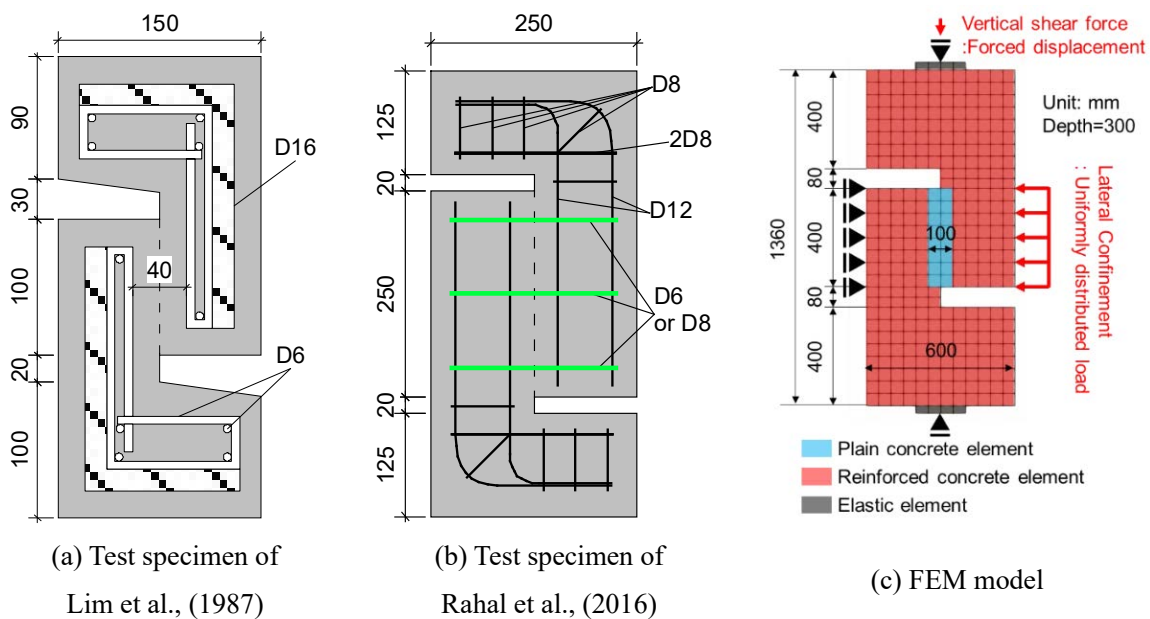
(c) FEM model

**Fig. 2-10    Test specimens of previous experimental studies and FEM model compared to them**

The identified values are compared with the ones of various materials in Fig. 2-13. The friction coefficients proposed in two different codes (ACI committee 318, 2019; Randl, 2013) where the model based on the friction law is used for evaluating interface shear transfer, are also described in the figure. Roughly speaking, the values set for concrete are equivalent to the values at the properly treated joint interface or dense sand, while the values set for mortar are slightly lower than the values at the smooth joint interface. It is speculated that the friction coefficient is higher than that of natural sand due to the fact that the aggregate is angular and the crushed cement increases the contact surface area.



(a) Shear capacity  (b) Residual strength
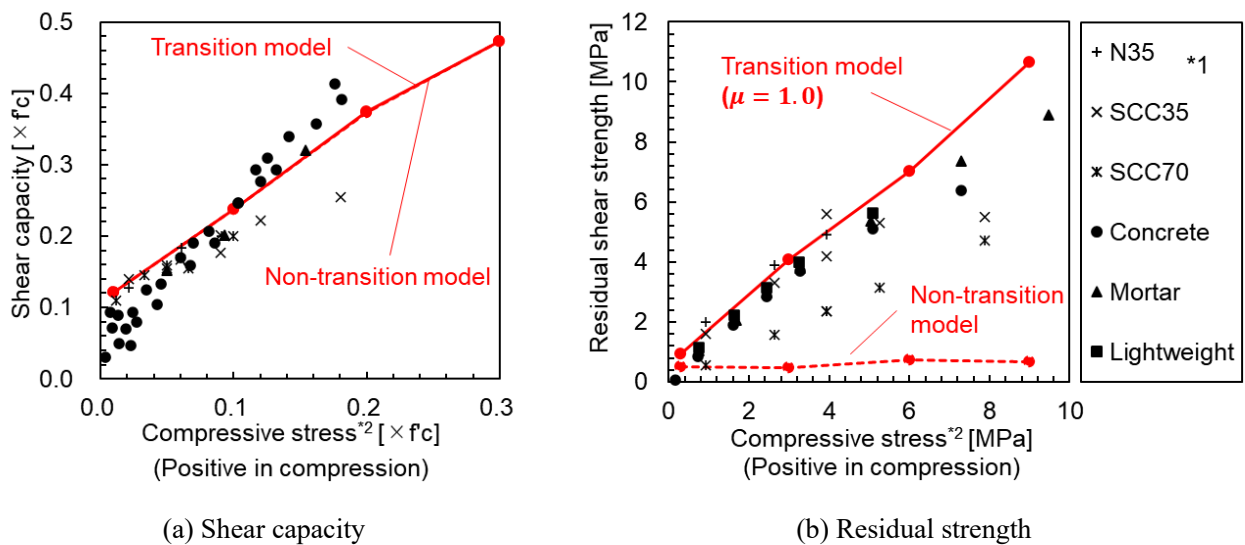
**Fig. 2-11　Confinement-dependency of shear strength of push-off type specimen *1: SCC35, SCC70 and N35 are the experimental data of Rahal et al. (2016), the others are those of Lim et al (1987), *2: $\rho_v f_{yv}$ in the original paper (Rahal et al. 2016)**
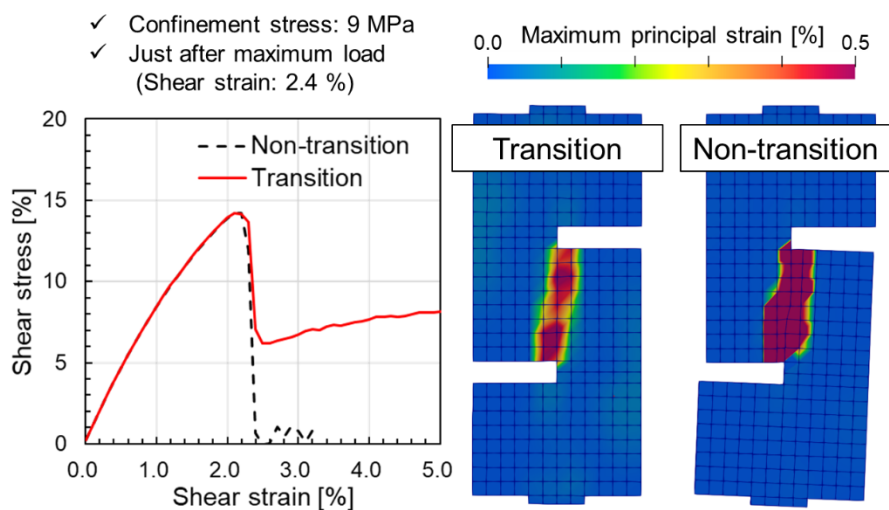


**Fig. 2-12　Simulation results of the push-off test obtained by transition and non-transition model**
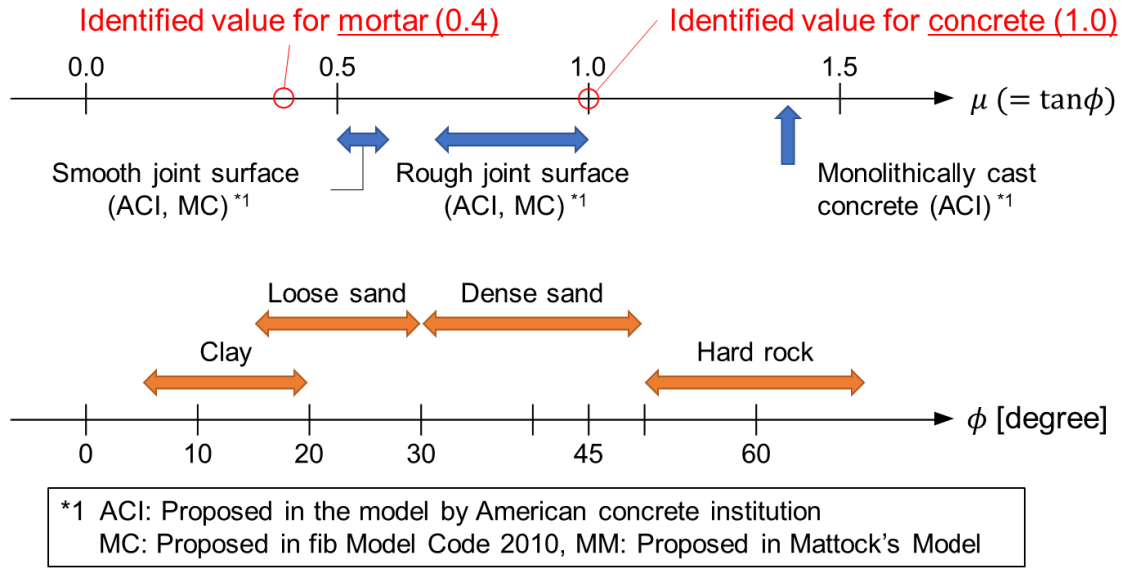
**Fig. 2-13   Identified friction coefficient for the proposed model compared with various material values.**

## 2.5   Mesh sensitivity

It is important the analytical result is independent of the mesh size. In the case of concrete whose rigidity is greatly reduced due to the occurrence of cracks, the fracture progresses at the cracked surface in the reference volume, while the concrete around it is unloaded. This problem is solved by setting the softening branch according to the element length so that the fracture energy is constant (Japan Society of Civil Engineers, 2010). As indicated in Fig. 2-6, the original model also follows this method, and the softening parameter according to the reference length is set for tension, compression, and shear (An et al., 1997). In the case of proposed model, since the softening behavior has been almost finished at the stage where the elasto-plastic model become dominant, the mesh size dependency is not considered in the model after graveling. Here, the sensitivity of mesh size is investigated by using the push-off test model same as previous section.

A fine mesh size model with a reference length that is half the previous one (Fig. 2-10 (c)) was additionally prepared. In order to determine the tensile softening factor, the fracture energy was calculated by the following equation according to the JSCE standard.

$$G_{\mathrm{f}} = 10 d_{\mathrm{max}}^{\frac{1}{3}} f'^{\frac{1}{3}}_{\mathrm{c}} \tag{2-18}$$

where, $G_{\mathrm{f}}$ is the fracture energy in N/m; $d_{\mathrm{max}}$ is the size of maximum coarse aggregate and set as 25 mm in all cases. The tensile softening factor corresponding to each reference length is determined so as to satisfy the following equation.

$$\int \sigma_{\mathrm{t}} \mathrm{d}\varepsilon_{\mathrm{t}} \approx \int_{\varepsilon_{\mathrm{tu}}}^{\varepsilon_{\mathrm{te}}} f_{\mathrm{t}} \left(\frac{\varepsilon_{\mathrm{tu}}}{\varepsilon_{\mathrm{t}}}\right)^{c_{\mathrm{t}}} \mathrm{d}\varepsilon_{\mathrm{t}} = \frac{G_{\mathrm{f}}}{L_{\mathrm{e}}} \tag{2-19}$$

where, $\sigma_{\mathrm{t}}$ and $\varepsilon_{\mathrm{t}}$ are tensile stress and strain, respectively; $f_{\mathrm{t}}$ is tensile strength; $\varepsilon_{\mathrm{tu}}$ and $\varepsilon_{\mathrm{te}}$ are the tensile strain at beginning of the softening and the upper limit strain for convenience of calculation, respectively; $L_{\mathrm{e}}$ is the reference length; $c_{\mathrm{t}}$ is the tensile softening parameter.

The non-linearity of concrete under compression is borne by plasticity and fracture. Based on the experimental fact that the constraint effect appears only in fracture, the equation of fracture parameter was developed from the original equation (Eq. (2-20)). In addition, a compressive softening factor that takes into account the material-specific fracture energy has been incorporated to accommodate arbitrary reference lengths (Maekawa et al., 2009). Finally, the fracture parameter for cracked concrete is expressed by the following equation.

$$K = \exp[-0.73\beta\{1 - \exp(-1.25\beta)\}], \qquad \beta = -\frac{1}{0.35}\left\{\ln\left(1 - \frac{7\varepsilon_{ec}}{20}\right)\right\} \qquad (2-20)$$

$$\varepsilon_{ec} = \varepsilon_e^{\Omega} \quad if \ \varepsilon_e \geq \Re; \quad \varepsilon_{ec} = \varepsilon_e \quad if \ \varepsilon_e < \Re \qquad (2-21)$$

$$\Re = 2.00 - 1.15\chi^{0.3}, \qquad \chi = \frac{f'_c}{f'_c + 4\sigma'_1} \qquad (2-22)$$

$$\Omega = \left\{0.75 + 0.87\exp\left(-\frac{\varepsilon'_e}{0.8\Re}\right)\right\}^{c_c} \qquad (2-23)$$

where, $K$ is the fracture parameter; $\varepsilon'_e$ is the equivalent compressive strain normalized by peak strain; $f'_c$ is the uniaxial compressive strength; $\sigma'_1$ is the lateral confining pressure.; $c_c$ is the compressive softening parameter The original model is based on the specified fracture energy in the case of reference length with 200 mm (Lertsrisakulrat et al., 2000). The compressive softening parameter can be calculated as well as tension, and the explicit-type computational formula has been proposed as below (Maekawa et al., 2009).

$$c_c = 1.25 - 0.62\left(\frac{L_e}{L^{ref}}\right)^2 - 0.63\left(\frac{L_e}{L^{ref}}\right) \qquad (2-24)$$

where, $L^{ref}$ is reference length on which the constitutive model based and set as 200 mm. Fig. 2-14 shows the changes in the softening curves of compression and tension due to the difference in softening parameter. Roughly speaking, the larger the tensile softening parameter or the smaller the compression one, the steeper the softening gradient.

In the shear transfer model, the shear softening is inherently considered under the constant confinement condition since the crack width increases as the shear slip increases. On the other hand, the shear stress under a constant crack opening width converges to the ultimate shear strength and no shear softening occurs. Then, ultimate shear strain is defined to macroscopically reduce shear stress as below, so that softening is reproduced even in the latter case.

$$\tau = \tau_{max}(\gamma_u/\gamma)^{c_s} \qquad (2-25)$$

where, $\tau_{max}$ is the maximum shear stress calculated by Eq. (2-2).; $\gamma_u$ is the ultimate shear strain, and 0.04% for plain concrete and 0.4% for reinforced concrete are assumed.; $c_s$ is the shear softening parameter. Here, the shear softening is taken into consideration only when the crack opening strain is greater than 0.1%, so there is almost no meaning in the case of unreinforced concrete with a small ultimate shear strain. The same softening parameter as tension is tentatively adopted according to An et al (1997).

28
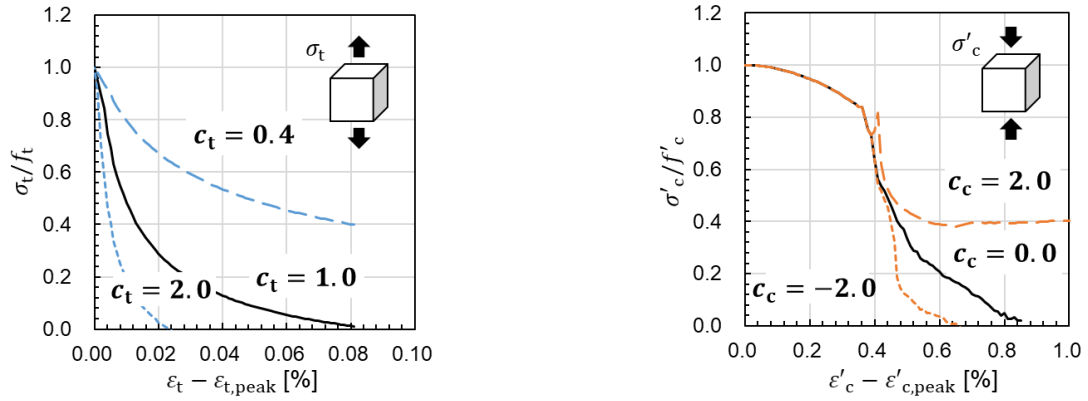
(a) Tension softening

(b) Compression softening

**Fig. 2-14 The effect of softening parameter on tension and compression softening**
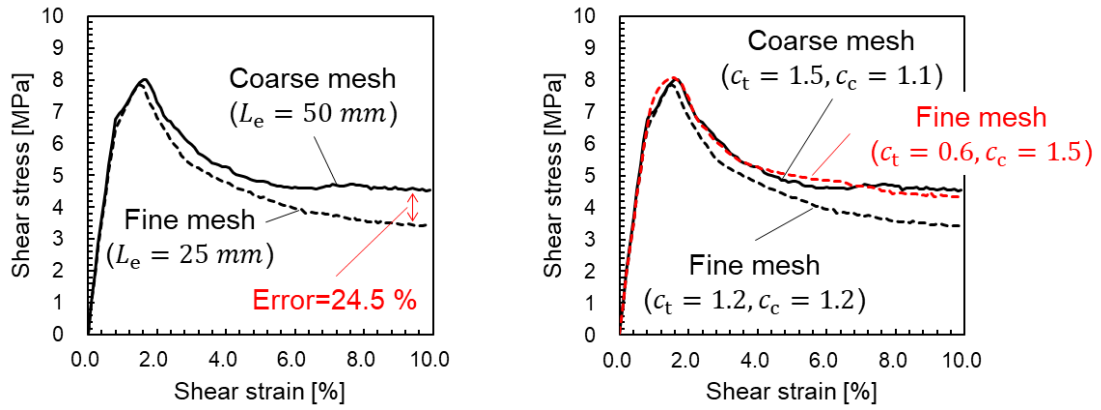


(a) Shear stress-shear strain relation

(b) Deformation and strain distribution

**Fig. 2-15 Comparison of analytical results obtained from models with different mesh size**

**(Confinement stress: 3 MPa)**



**Fig. 2-16 Deformation and strain distribution obtained from models with different mesh size**

**(Confinement stress: 3 MPa)**

29

The analytical results obtained from models with different mesh size are compared in Fig. 2-15. Although the stress-strain relation was not changed in the ascending part, there were some differences in the softening branch. However, the error in residual strength in the case of fine mesh with respect to the case of coarse mesh is about 25%, which is within the range of variation between specimens. Moreover, it was confirmed that it is possible to reduce the error by adjusting the softening coefficient built into the original model as shown in Fig. 2-15 (b). A finer mesh can reproduce the local strain distribution as shown in Fig. 2-16, but the failure mode is the same regardless of the mesh size. It was proved that it is not necessary to consider the influence of mesh size in the post-transition model. If the softening behavior is incorporated in the model after the transition, it will be necessary to consider the fracture energy according to the mesh size.

## 2.6    Summary of Chapter 2

Assuming that graveling progresses with the disintegration of concrete, a simple constitutive model that represents the transition of physical properties from concrete to ground material has been proposed. The validity of the model was verified by comparison with the past push-off test results, and the residual friction coefficient of concrete was identified as 1.0. Furthermore, from the results of the ana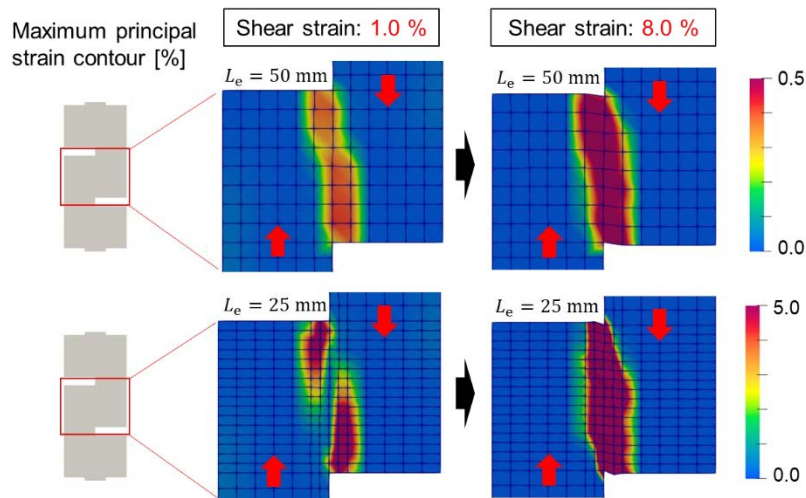lysis models with different mesh sizes, it is clarified that it is not necessary to consider the mesh size dependency in the elasto-plastic model after the transition.

## References of Chapter 2

ACI committee 318, 2019. *Building Code Requirements for Structural Concrete and Commentary (ACI 318-19)*. American Concrete Institute.

An, X., Maekawa, K., Okamura, H., 1997. Numerical simulation of size effect in shear strength of RC beams. *Doboku Gakkai Ronbunshu 1997*, 297–316. https://doi.org/10.2208/jscej.1997.564_297

Bažant, Z.P., Gambarova, P., 1980. Rough cracks in reinforced concrete. *Journal of the Structural Division 106*. https://doi.org/10.1061/JSDEAG.0005400

Bujadham, B., Mishima, T., Maekawa, K., 1992. Verification of the universal stress transfer model. *Doboku Gakkai Ronbunshu 1992*, 289–300. https://doi.org/10.2208/jscej.1992.451_289

Japan Society of Civil Engineers, 2010. *Standard Specifications for Concrete Structures-2007, "Design." Japan Society of Civil Engineer*s, Tokyo, Japan.

Kang, S.-B., Tan, K.H., Zhou, X.-H., Yang, B., 2017. Experimental investigation on shear strength of engineered cementitious composites. *Engineering Structures 143*, 141–151. https://doi.org/10.1016/j.engstruct.2017.04.019

Lertsrisakulrat, T., Watanabe, K., Matsuo, M., Niwa, J., 2000. Localization effects and fracture mechanics of concrete in compression. *Proceedings of the Japan Concrete Institute 22*, 145–150.

Li, B., Maekawa, K., Okamura, H., 1989. Contact density model for stress transfer across cracks in concrete. *Journal of Faculty of Engineering*, The University of Tokyo 40, 9–52.

Lim, T.B., Li, B., Maekawa, K., 1987. Mixed-mode strain softening model for shear fracture band of concrete subjected to in-plane shear and normal compression, in: *Proc. of Int. Conf. on Computational Plasticity*. Barcelona, Spain, pp. 1431–1443.

Maekawa, K., El-Kashif, K.F., 2004. Cyclic cumulative damaging of reinforced concrete in post-peak regions. *Journal of Advanced Concrete Technology 2*, 257–271. https://doi.org/10.3151/jact.2.257

Maekawa, K., Fujiyama, C., 2013. Rate‐dependent model of structural concrete incorporating kinematics of ambient water subjected to high‐cycle loads. *Engineering Computations 30*. https://doi.org/10.1108/EC-06-2012-0125

Maekawa, K., Fukuura, N., 2013. Nonlinear modeling of 3D structural reinforced concrete and seismic performance assessment, in: *Infrastructure Systems for Nuclear Energy*. John Wiley & Sons, Ltd, Chichester, UK, pp. 153–184. https://doi.org/10.1002/9781118536254.ch11

Maekawa, K., Ishida, T., Kishi, T., 2009. *Multi-Scale Modeling of Structural Concrete*, 1st ed. Taylor & Francis, Oxford.

Maekawa, K., Pimanmas, A., Okamura, H., 2003. *Nonlinear Mechanics of Reinforced Concrete*. CRC Press Taylor and Francis Group, London.

Mattock, A.H., Hawkins, N.M., 1972. Shear transfer in reinforced concrete -recent research. *PCI Journal 17*, 55–75. https://doi.org/10.15554/pcij.03011972.55.75

Miura, K., Hasegawa, K., Matsumoto, Y., Toki, S., 1990. The influence of grain shape and grain size distribution on the mechanical properties of sands. *Bulletin of the Faculty of Engineering*, Hokkaido University.

Miyahara, T., Kawakami, T., Maekawa, K., 1988. Nonlinear behavior of cracked reinforced concrete plate element under uniaxial compression. *Concrete Library of JSCE*, 131–144.

Okamura, H., Maekawa, K., 1991. *Nonlinear Analysis and Constitutive Models of Reinforced Concrete*. Gihodo-Shuppan Co, Japan.

Rahal, K.N., Khaleefi, A.L., Al-Sanee, A., 2016. An experimental investigation of shear-transfer strength of normal and high strength self compacting concrete. *Engineering Structures 109*, 16–25. https://doi.org/10.1016/j.engstruct.2015.11.015

Randl, N., 2013. Design recommendations for interface shear transfer in fib Model Code 2010. *Structural Concrete 14*, 230–241. https://doi.org/10.1002/suco.201300003

Resende, T.L., Cardoso, D.C.T., Shehata, L.C.D., 2021. Experimental and theoretical investigation on the stress transfer across cracks due to combined action of steel fibers and aggregate interlock. *Cement and Concrete Composites 124*, 104239. https://doi.org/10.1016/j.cemconcomp.2021.104239

Rowe, P.W., 1962. The stress-dilatancy relation for static equilibrium of an assembly of particles in contact. *Proceedings of the Royal Society of London. Series A*. Mathematical and Physical Sciences 269, 500–527. https://doi.org/10.1098/rspa.1962.0193

Schanz, T., Vermeer, P.A., 1996. Angles of friction and dilatancy of sand. *Géotechnique 46*. https://doi.org/10.1680/geot.1996.46.1.145

Shibuya, S., Mitachi, T., Ozawa, H., 2001. Time/stress-history dependency of deformation-strength characteristics of cement-mixed sand. *Doboku Gakkai Ronbunshu 2001*, 249–257. https://doi.org/10.2208/jscej.2001.687_249

Skempton, A.W., 1985. Residual strength of clays in landslides, folded strata and the laboratory. *Géotechnique 35*. https://doi.org/10.1680/geot.1985.35.1.3

Tassios, T.P., Vintzēleou, E.N., 1987. Concrete-to-concrete friction. *Journal of Structural Engineering 113*. https://doi.org/10.1061/(ASCE)0733-9445(1987)113:4(832)

Tobita, Y., Yamaguchi, A., Fujii, N., Kanahara, M., 2003. A simple method for description of anisotropic behavior of engineering materials: modified stress method with an emphasis on geomaterials. *J Appl Mech 6*, 407–418. https://doi.org/10.2208/journalam.6.407

Vecchio, F.J., Collins, M.P., 1986. The modified compression-field theory for reinforced concrete elements subjected to shear. *Journal of the American Concrete Institute*, ACI.

Walraven, J.C., Reinhardt, H.W., 1981. Theory and experiments on the mechanical behavior of cracks in plain and reinforced concrete subjected to shear loading. *HERON 26*, 25417.

Yamanoi, Y., Maekawa, K., 2020. Shear bifurcation and graveling of low-strength concrete. *Journal of Advanced Concrete Technology 18*, 767–777. https://doi.org/10.3151/JACT.18.767

Yang, K.-H., Sim, J.-I., Kang, J.-H., Ashour, A.F., 2012. Shear capacity of monolithic concrete joints without transverse reinforcement. *Magazine of Concrete Research 64,* 767–779. https://doi.org/10.1680/macr.11.00107

# 3 Model Verification and Validation for Low-strength Concrete Subjected to Monotonic Load

## 3.1 Experiment of multi-layer composite

### (1) Overview

In order to qualitatively quantitatively validate the proposed model, the multi-layer composite experiment was carried out. Here, this experiment has analogy to both the shear bifurcation and dispersion of artificial soft rock made by low-strength concrete when localized fault displacement acts as shown in Fig. 3-1. The low-strength concrete is expected to absorb the energy to stop the fault propagation to the large structural slabs of some power plants line a seismic isolation. In this case, the graveling of concrete is expected to absorb much energy. This is the engineering background of this experiments.

A total of 4 specimens consisting of 3 layers were created as summarized in Table 3-1. In all specimens, the bottom layer is high-strength concrete that replicates the rock mass, and the upper layer is normal strength concrete that stands for a duct. A weak layer assuming the artificial soft rock was placed as the intermediate layer, and the low-strength concrete or mortar used in this layer is the main target of the model verification.
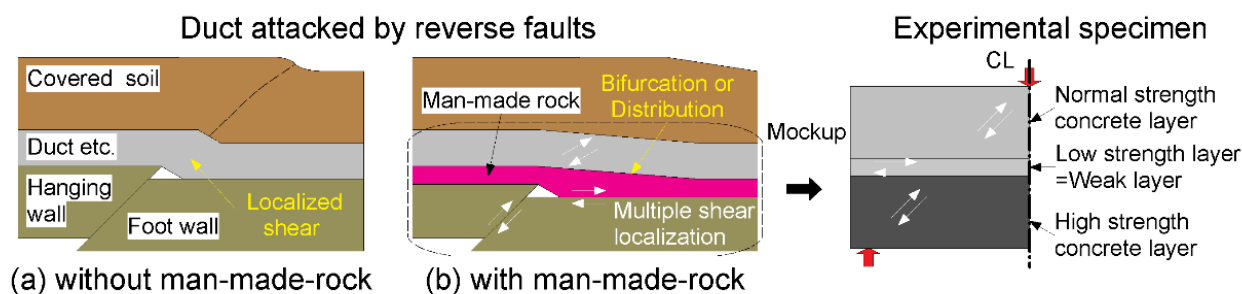


**Fig. 3-1 Bifurcation of man-made rock and mock-up specimen**

**Table 3-1 Summary of the experiment**

| Case name | Material used in each layer[*1] | | | Shape[*1] | Year | Memo |
|---|---|---|---|---|---|---|
| | Intermediate | Upper | Bottom | | | |
| FL-8C-O | L-8C-a | N-a | H-a | A | 2018 | Smooth joint surface |
| FL-8C | L-8C-b | N-b | H-b | B | 2019 | Rough joint surface |
| FL-2C | L-2C | N-c | H-c | C | 2020 | Intermediate layer : Weakest concrete |
| FL-2M | L-2M | N-c | H-c | C | 2020 | Intermediate layer: Mortar |

*1 Distinguished names correspond to the ones in Table 3-2 and 3-4.

(2) Test specimens

The mechanical properties obtained from the composition of each layer and the tested compressive strength are listed in Table 3-2. Dimensions and the rebar arrangement of each specimen are indicated in Fig. 3-2. The compressive strength of the weak layer was about 8 MP or about 2 MPa. In the case of a weak layer with a compressive strength of 8 MPa, there were two cases, one with a strong joint interface and the other with a weak one. In addition, in order to investigate the effect of coarse aggregate, two cases were prepared, one is the case where the weak layer is concrete with a coarse aggregate with a maximum particle size of 20 mm (FL-2C), and the other is the case of mortar (FL-2M), when the compressive strength of the weak layer was 2 MPa. All specimens were designed so that shear failure predominates, and no stirrup was provided. Only FL-2C and FL-2M were provided with compressive reinforcement so as to increase the shear to the weak layer. Although the effective depth or reinforcement arrangement varied, the ratio of shear span to effective depth was set to 1.0 in all cases. Here, "F" of the notation means strength, "L" means low, numerical values represents the compressive strength, and "C" or "M" means concrete or mortar, respectively.

The high-strength concrete of bottom layer was firstly cast, and then weak layer and the normal-strength concrete of upper layer were cast every other day (every few days in the case of FL-8C-O). In order to make the joint interface strong enough, chemical retarder was sprayed on each joint surface and the laitance was removed by water jet. As a result, the aggregate was exposed at a height of about 5~10 mm from the joint surface in FL-8C, FL-2C and FL-2M, while about 2~3mm in FL-8C-O. After the formwork was removed one day after the upper layer was cast, the specimen was cured while maintaining humidity by spraying with water and wrapping for 28 days. After a sufficient curing period has passed, the specimen was statically and monotonically loaded.

(3) Measurement items and loading method

A mosaic pattern was painted onto one surface of the specimens (Fig. 3-3), and image measurement, which is called Digital Image Correlation (DIC) method, was used to measure the displacement of the entire surface of the specimens (Sutton et al., 2009). By shooting one measurement surface with two cameras, 3D distortion at any point can be measured over the entire surface. Except the case of FL-8C-O, each shear span was photographed with a separate camera due to the convenience of the loading machine. A total of 4 cameras were used in these cases. A high resolution camera was used so that the maximum displacement measurement error is less than about 50 μm. To double-check precision, displacement was measured by using grounded displacement gauges installed at several locations, including near the specimen supports.

After applying a preload with a load of about 100 kN, a monotonic load was statically applied by displacement control. Photographs for strain measurement were acquired for each fixed load (20~50 kN) and manually linked with the load value.

**Table 3-2  Details of the concrete or mortar used in the experiment**

| \Property Layer\ | Proportion | | Unit amount [kg/m$^3$] | | | | | | Mechanical properties | | |
|---|---|---|---|---|---|---|---|---|---|---|---|
| | W/C | S/A | C | LS | W | S | G | Ad | $f'_c$ | $E_0$ | $f_t$ |
| | % | % | kg | kg | kg | kg | kg | kg | MPa | GPa | MPa |
| N-a | 52.0 | 44.4 | 323 | 0 | 168 | 798 | 1026 | 0.485 | 46.1 | 31.4 | 3.43 |
| N-b | 60.0 | 48.0 | 283 | 0 | 168 | 861 | 958 | 2.270 | 44.5 | 35.6 | 3.03 |
| N-c | " | " | " | " | " | " | " | " | 44.1 | 34.1 | 4.70 |
| H-a | 23.0 | 42.8 | 739 | 0 | 170 | 652 | 896 | 11.824 | 110 | 45.7 | 6.05 |
| H-b | 23.0 | 43.0 | 739 | 0 | 170 | 598 | 815 | 11.100 | 104 | 42.0 | 4.89 |
| H-c | " | " | " | " | " | " | " | " | 123 | 43 | 7.7 |
| L-8C-a | 150 | 47.6 | 109 | 105 | 163 | 899 | 1018 | 0.218 | 7.86 | 17.1 | 0.96 |
| L-8C-b | 150 | 48.0 | 113 | 110 | 170 | 870 | 968 | 0.340 | 8.16 | 30.1 | 0.97 |
| L-2C | 300 | 48.0 | 57 | 186 | 170 | 867 | 964 | 0.170 | 2.17 | 3.51 | 0.42 |
| L-2M | 300 | 100 | 80 | 263 | 239 | 1530 | 0 | 0.800 | 2.30 | 4.40 | 0.52 |

W/C: Water to cement ratio, S/A: Volume ratio of sand in total aggregate

C: Cement, LS: Limestone, W: Water, S: Sand, G: Gravel, Ad: Admixture

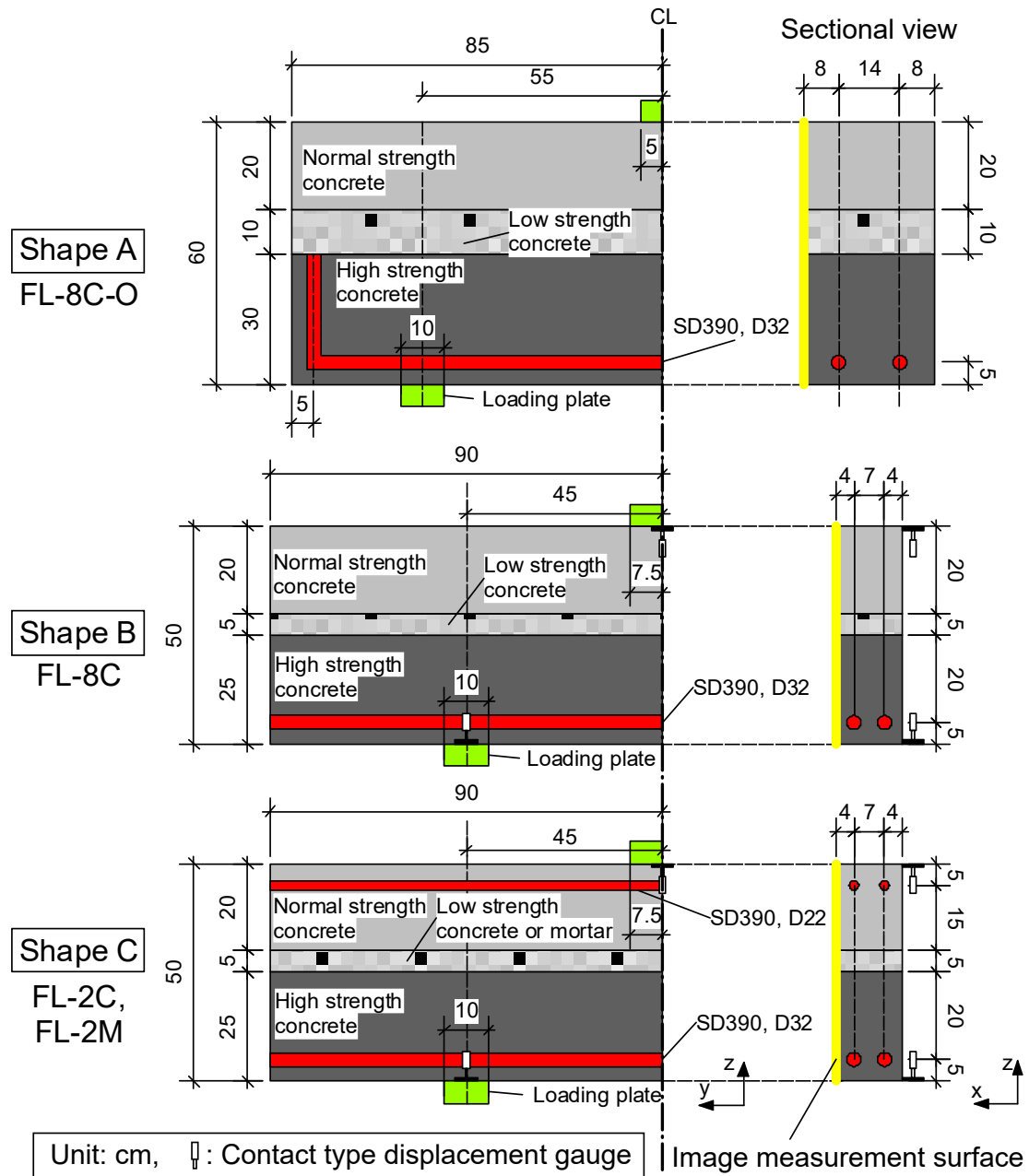$f'_c$: Compressive strength, $E_0$: Young's modulus, $f_t$: Tensile strength
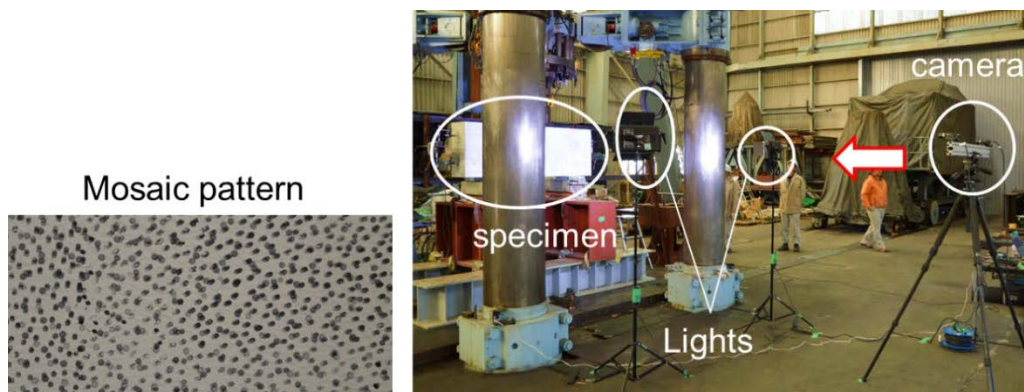
**Fig. 3-2  Test specimens (unit: cm)**



**Fig. 3-3  Image measurement instrument setup and mosaic pattern (FL-8C-O).**

(4) Experimental results

The test results of the case of FL-8C-O and FL-8C have been already reported in (Yamanoi and Maekawa, 2020a, 2020b, 2016). The results of FL-2C and 2M are compared with FL-8C here.

Fig. 3-4 shows the load-displacement relation of each specimen. Although there is no empirical formula to assess the shear capacity of the multi-layered beam for practice, comparison of the experimentally obtained data with the monolithically constructed beam of the unique material strength will be useful. Then, as a reference, Fig. 3-4 also shows the design capacity of the homogeneous beam calculated by JSCE code specification (Japan Society of Civil Engineers, 2010) with the compressive strength of 44.1 MPa (equal to the normal strength of concrete in this experiment as indicated in Table 3-2). In the case of weak layer with 8 MPa (FL-8C) as previously reported, the load capacity was equivalent to the JSCE computed design one. When the strength of the weak layer is reduced to about 1/4 (FL-2C), it can be seen that the rigidity and load bearing capacity are slightly reduced, but the difference is not so big. On the other hand, when the weak layer was mortar (FL-2M), the rigidity and load bearing capacity were greatly reduced, and the fracture mode was also changed.
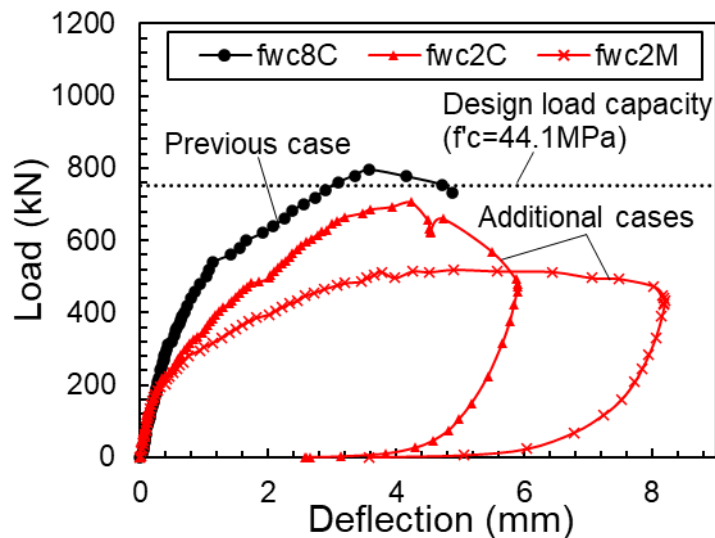


**Fig. 3-4   Experimental load-deflection relations**

Fig. 3-5 and Fig. 3-6 show the shear strain distributions of weak concrete with coarse aggregate and weak mortar, which is measured by the image correlation method. As each shear span was photographed with a separate camera, the two photographs were juxtaposed. Another strain is also summarized in **Appendix B**.

When the weak layer was concrete with compressive strength of 2 MPa (FL-2C), large strain evolved in the weak layer as the load increased, and shear cracks were confirmed in the bottom layer of the left span when the load was 200 kN (Point a in Fig. 3-5). After that, shear cracks also occurred in the bottom layer of the right span, and when the load reached 500 kN, the shear cracks penetrated into the upper layer (Point b in Fig. 3-5). Shear damage in the weak layer reached the edge of the beam and was visually confirmed. Eventually, shear cracks grew and opened on the line connecting the loading point and the support, leading to brittle fracture (Point c in Fig. 3-5).

Fig. 3-7 shows the test specimen after failure. In the case of FL-2C (Fig. 3-7 (b)), at the loading point, peeling of

the surface concrete, which seems to be crushed, was also observed. This is similar to the fracture mode of homogeneous deep beams (Lertsrisakulrat et al., 2002; Zhang and Tan, 2007). Even after the visible cracks occurred over the entire weak layer, the load increased by about 200 kN, leading to shear failure penetrating the upper and bottom layers. Despite the absence of shear reinforcement, two distinct shear cracks occurred in the bottom layer of each span. These behaviors were also observed in the case of FL-8C. It is probable that the weak layer would maintain shear stress transfer even after peak loading. The photo on the right of Fig. 3-7 (b) is an enlargement of the weak layer. The surface layer had already peeled off, but the core had closed cracks. This means that some confinement might remain even after the shear disintegrated graveling. The effect of confinement on the shear transfer characteristics of the weak layer is thought to be worth investigating.

When the weak layer was made of a mortar with compressive strength of 2 MPa (FL-2M), shear cracks in the bottom layer and the beam flexural cracks in the center of the upper span were confirmed when the load was about 200 kN, similar to FL-2C (Point a in Fig. 3-6). After that, the shear cracks in the bottom layer became larger, and at the same time, the damage in the weak layer extended to the edge (Point b in Fig. 3-6). The width of the bending cracks in the upper layer increased as the load increased, and after the cracks reached the edge through the weak layer, the load did not increase any more (Point c in Fig. 3-6).

Unlike FL-2C, there was no shear crack in the upper layer until the ultimate state and there was only one major shear crack in the bottom layer of each span. Fig. 3-7 (c) shows smooth cracked surfaces due to the absence of coarse aggregate. It has been reported that shear transfer is significantly reduced when the crack surface is smooth, such as in the case of mortar and high-strength concrete (Bujadham et al., 1992). Due to the decrease in shear transfer, the integrity of the upper and bottom layers was lost, resulting in a lap beam state. Even in this case, the weak layer maintained constant shear transfer, and shear cracks also occurred in the upper layer at the ultimate state. It is clarified that even in the mortar where sufficient aggregate interlock cannot be expected, frictional action plays a major role in shear stress transfer.

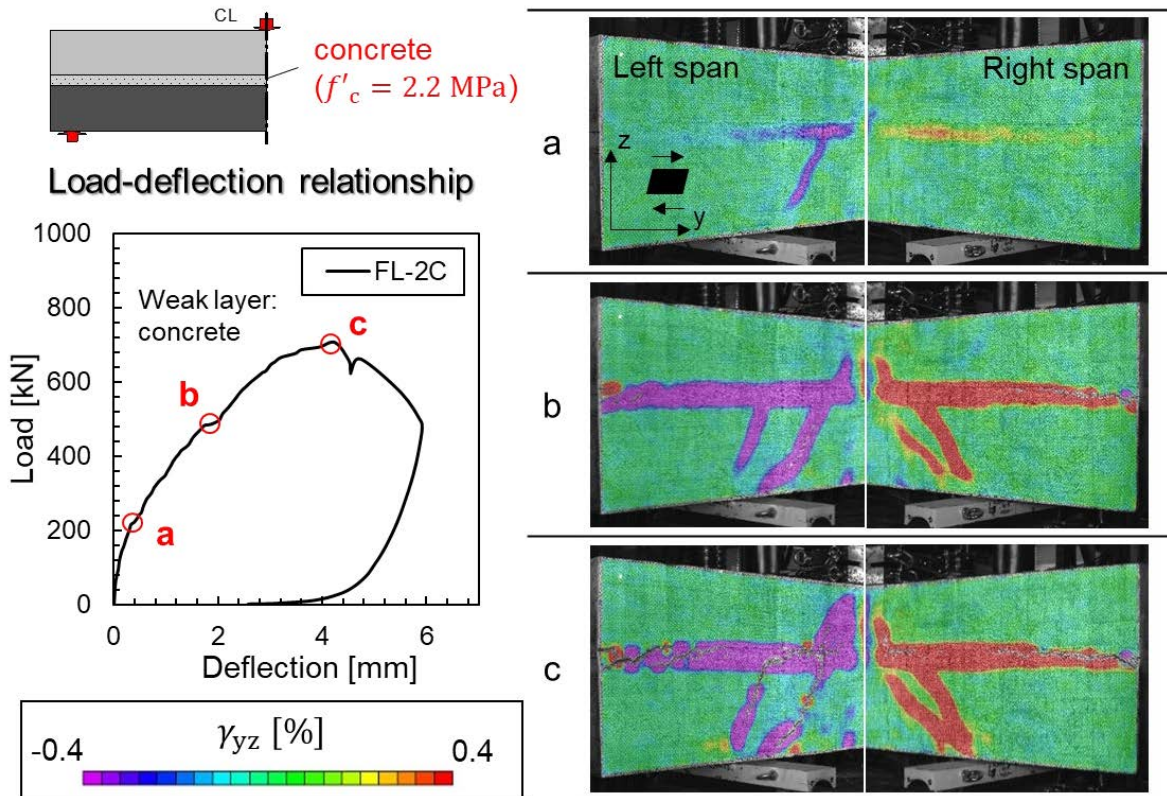## Load-deflection relationship

concrete ($f'_c = 2.2$ MPa)



Fig. 3-5  Experimental strain distribution in the case of FL-2C

## Load-deflection relationship
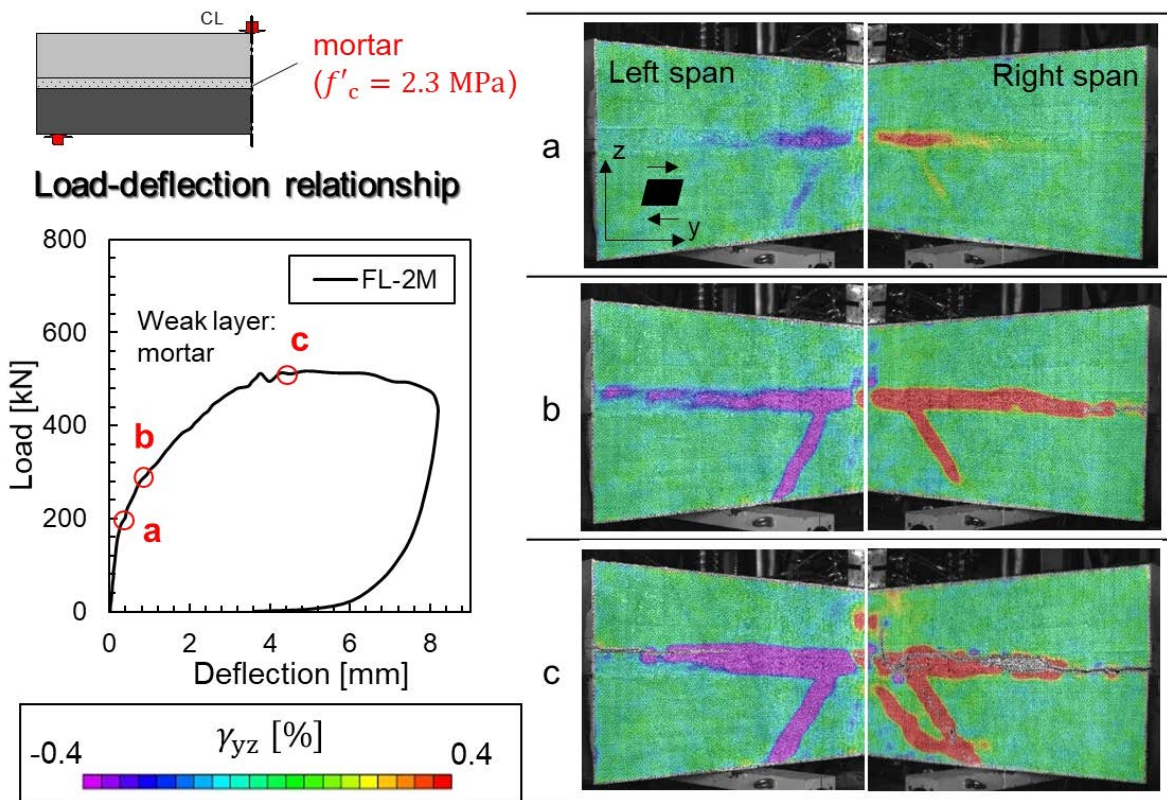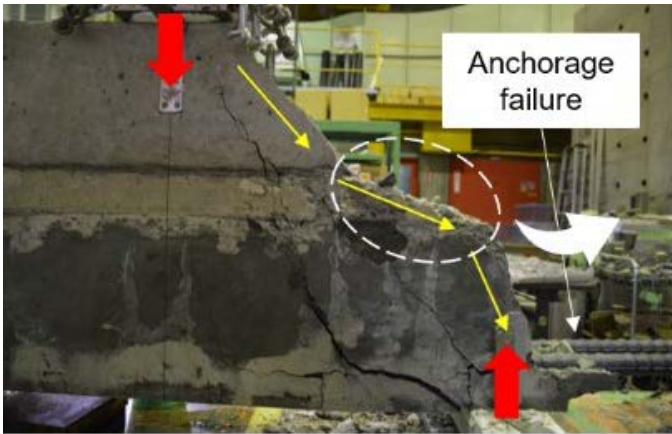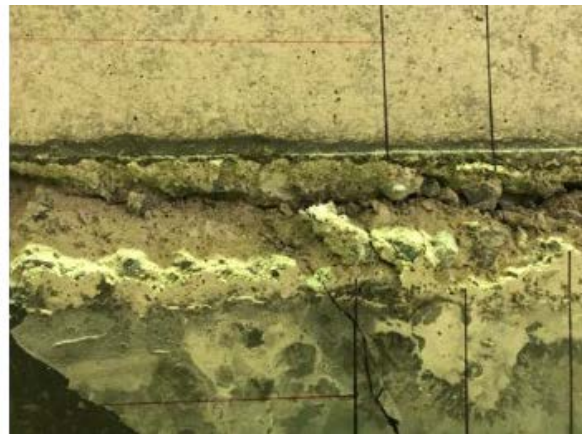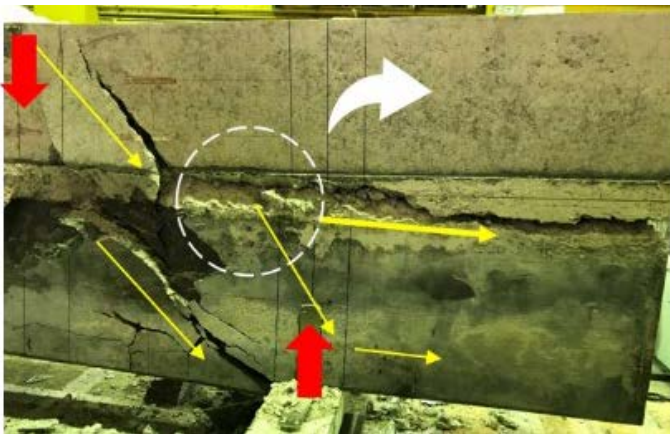
mortar ($f'_c = 2.3$ MPa)



Fig. 3-6  Experimental strain distribution in the case of FL-2M

(a) FL-8C



(b) FL-2C



(c) FL-2M

**Fig. 3-7　Failure mode of each specimen**

3.2    Verification of the proposed model

(1)  Analysis without failure of joint surface (FL-8C, FL-2C and FL-2M)

In this section, FE analysis of multi-layer composite experiments is performed. In the analysis, moisture migration and thermodynamic equilibrium are calculated by considering concrete composition, hydration reaction and curing conditions, and the strength and shrinkage of structural concrete are calculated from the thermodynamic model. This allows us to reproduce the different drying shrinkages of the various layers and reflect them in the structural analysis (Maekawa et al., 2009; Yoneda et al., 2013). Table 3-3 lists the main mechanical models incorporated in the constitutive model.

**Table 3-3    Major component of material models** (Maekawa et al., 2003)

| Material | Constitutive Model | Memo |
|---|---|---|
| Uncracked concrete | 3D elasto-plastic fracture model | Nonlinearity= Plasticity + Continuum fracturing |
| Cracked concrete | Elasto-plastic fracture model | Compression behavior |
| | Tension stiffening model | Tension behavior |
| | Contact density model | Shear transfer along crack surface |
| Reinforcement | Multi-surface plasticity model | Assuming tension stiffening by covered concrete |

For step-by-step process of searching nonlinear solutions, the total strain method was used (Cervenka, 2002; Maekawa and Fukuura, 2013; Vecchio and Selby, 1991). The path of strain at each point from the one of the previous time to the updated one is assumed to vary linearly. On this path of the finite strain increment, crack occurrence, yield of reinforcement and elasticity degradation by compressive crushing of concrete are checked and the corresponding total stresses of cracked concrete is computed by integrating the constitutive models of shear transfer along crack plane and tension softening normal to it as stated in **Chapter 2**. The concrete surrounded by multi-directional crack planes are treated as continuum media.

In the iterative process of searching the equilibrium solution, path-dependent parameters were not changed during the iteration process with the assumed total strains but were revised and renewed at the next time step after the convergence. The dynamic effect of inertia was also implemented, and the acceleration term of equilibrium was evaluated by using Newmark-beta (=0.7) algorithm. In this analysis, since structural snap-back behaviors have not occured, the volume control method (Song et al., 2002) was not used but the modified Newton method was applied according to the unbalanced nodal forces during the iterative process. About 40 steps of time interval were set up till the peak loads. A sufficiently short sequence of the load step was examined that the load-displacement curve did not change with it.

The physical characteristics used in the analysis are given in Table 3-4. The input water-cement ratio was identified from the experimentally obtained compressive strength. The shear transfer characteristics are defined by the contact density function of the cracked surface. Since the mortar crack surface is smooth, its shear strength is about 1/5 that of concrete. From the curing conditions of the experiment, the humidity was 99 % relative humidity for 21 days after demolding. After two months of sealing and curing until the loading date, the specimen was cured at a relative humidity of 70% (1 to 2 months).

41

The finite element discretization used is shown in Fig. 3-8. The loading plate was made of an elastic body, and a joint interface element was placed between the loading plate and the multi-layer composite to allow for local separation and slippage as in reality. A cracked concrete model that allows for six-directional cracking was applied (Maekawa and Fukuura, 2013). An elasto-plastic constitutive model of reinforcement was applied to the part where the reinforcing bars were arranged (Maekawa et al., 2003).

Table 3-4　Input values in each case

| \Property<br>Layer\ | Input values | | | | | | | Calculated Value[1] | |
|---|---|---|---|---|---|---|---|---|---|
| | WP | BLN | P3A | P3S | P4AF | P2S | PPCS2H | $f'_c$ | $\varepsilon_{s,mean}$ |
| | % | cm$^2$/g | % | % | % | % | % | MPa | μ |
| N-a | 52.0 | 3350 | 9.00 | 56.0 | 9.00 | 18.0 | 3.40 | 41.2 | -177 |
| N-b | 50.0 | 4210 | 9.00 | 63.0 | 8.00 | 12.0 | 6.45 | 48.3 | -171 |
| N-c | 58.0 | 3340 | 9.00 | 56.0 | 9.00 | 18.0 | 8.00 | 45.0 | -173 |
| H-a | 23.0 | 3250 | 4.00 | 43.0 | 10.0 | 37.0 | 6.00 | 114 | -68.9 |
| H-b | 23.0 | 4210 | 9.00 | 63.0 | 8.00 | 12.0 | 6.45 | 115 | -65.6 |
| H-c | 25.5 | 3180 | 3.00 | 43.0 | 13.0 | 36.0 | 5.00 | 122 | -115 |
| L-8C-a | 52.0 | 3350 | 9.00 | 56.0 | 9.00 | 18.0 | 3.40 | 8.04 | -118 |
| L-8C-b | 90.0 | 4210 | 9.00 | 63.0 | 8.00 | 12.0 | 6.45 | 8.74 | -119 |
| L-2C,M[2] | 148 | 3340 | 9.00 | 56.0 | 9.00 | 18.0 | 8.00 | 2.07 | -148 |

WP: Water to cementitious powder ratio, BLN: Effective Blaine values of each cement powder, P3A, P3S, P4AF, P2S, PPCS2H: Weight percentage of mineral compounds as C3A, C3S, C4AF, C2S and gypsum, $\varepsilon_{s,mean}$: Average shrinkage strain of each layer just before shear loading, [1]: Calculated in the no-transition model, [2]: Only in the case of mortar (-2M), shear reduction factor of 4.0 is considered.
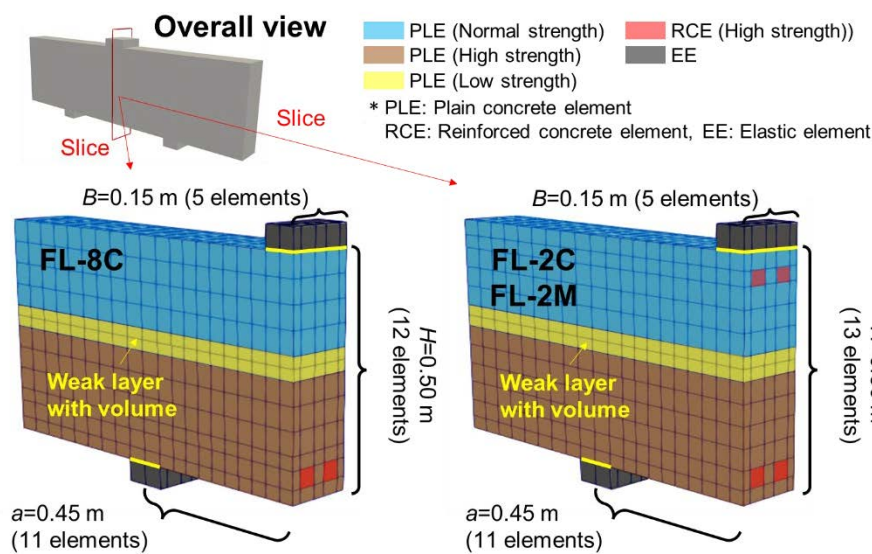


Fig. 3-8　Mesh discretization of each case

The proposed model applies only to the middle layer (weak layer). Here, it is necessary to set the elastic stiffness

and the coefficient of friction for the disintegrated graveling. In this study, $E_0 = 0.4\,\text{GPa}$ was set so as to be at the same level as the Young's modulus of gravel with reference to the experimental results (Shibuya et al., 1992). Poisson's ratio was set to 0.3, and the volume stiffness $K_0$ and the shear stiffness $G_0$ are derived by the following equations. The ultimate frictional angle was set to 1.0 for concrete and 0.4 for mortar as identified in **Chapter 2**.

$$K_0 = \frac{E_0}{3(1 - 2v_0)}, \qquad G_0 = \frac{E_0}{2(1 + v_0)} \tag{3-1}$$

Fig. 3-9 shows a comparison of the load-displacement relation of the experiment and the analysis in each case. The analysis when the transition model is not applied to the weak layer is shown by the broken line. In all cases, the experimental results can be reproduced well by applying the transition model. In particular, when the strength of the weak layer is smaller for concrete and mortar (FL-2C and FL-2M), non-transition models bring about similar capacity although the much less shear transfer for mortar is assumed rather than that of concrete. This apparently contradictory results attribute to the fact that the member capacity is chiefly carried by the upper and bottom layers and the central weak later works just to transfer normal stresses based upon the volumetric stiffness rather than the shear actions. Under this lower strength, the absolute shear transfer is so small for both concrete and mortar. But the transition model gives rise to the higher capacity for both cases. Then, it is definitely necessary to apply a transition model to improve accuracy for low strength cementitious composites. This is the clear evidence how the transition modeling is indispensable.

For the case of FL-8C of higher strength closer to the normal strength, the structural rigidity is computationally estimated a bit less than the reality. Then, the authors conducted the sensitivity analysis with the greater numerical value of $E_0$=20 GPa in Eq. (3-1) as shown in Fig. 3-9 (a). The trial analysis brings about the high consistency (Yamanoi and Maekawa, 2020b). Thus, the authors conclude that Eq. (3-1) has room for further improvement to cover the whole range of concrete strength in future. More discussion is carried on in Section 3.3.

Fig. 3-10 - Fig. 3-12 show the computed shear strain distribution. The crack path of the experiment is shown by the white dotted lines in the deformational diagram at the final state. In the case of FL-8C, it was possible to reproduce by the analysis how the shear damage that penetrates the upper and bottom layers increases while the damage is concentrated in the weak layer (see Fig. 3-10). However, the cracks propagating from the central weak layer to the bottom layer just above the support plate are not so clear.

In the case of FL-2C, in addition to the damage of the weak layer extending to the end of the specimen, the shear damage of the upper and bottom layers could be reproduced as shown in Fig. 3-11. The shear strain distribution is also consistent with the experimental cracking process. The shear localization extending from the weak layer to the bottom one is smaller than in reality. For the case of FL-2M, with no shear cracking in the upper layer, the analysis was able to reproduce the strain distribution (see Fig. 3-12).

Fig. 3-11 and Fig. 3-12 also show the post-peak analysis results when the existing concrete model is applied to the weak layer (non-transition). In this case, no cracking in the bottom layer appeared. When the transition model is applied, the simulation is well improved. It was confirmed that the experimental results can be roughly reproduced with a simple transition model even for low-strength concrete with compressive strength of only about 2 MPa.
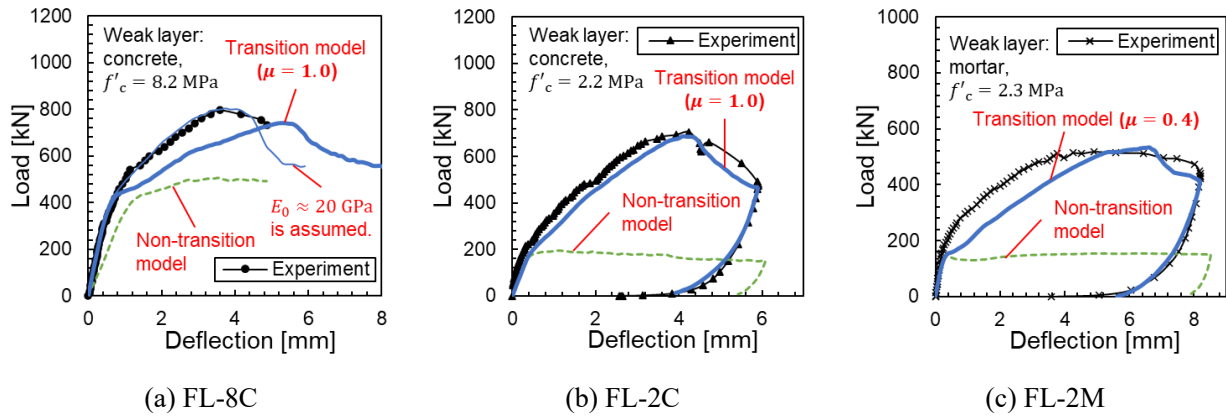
43

(a) FL-8C         (b) FL-2C         (c) FL-2M

**Fig. 3-9    Comparison of the load-deflection relations between experimental and analytical results**



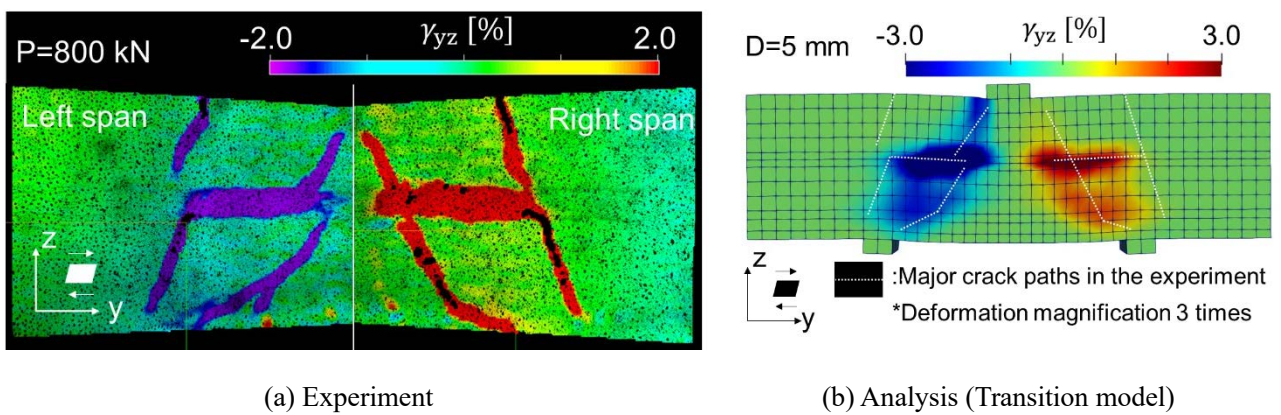(a) Experiment           (b) Analysis (Transition model)

**Fig. 3-10    Comparison of shear strain distribution between experiment and analysis (FL-8C)**
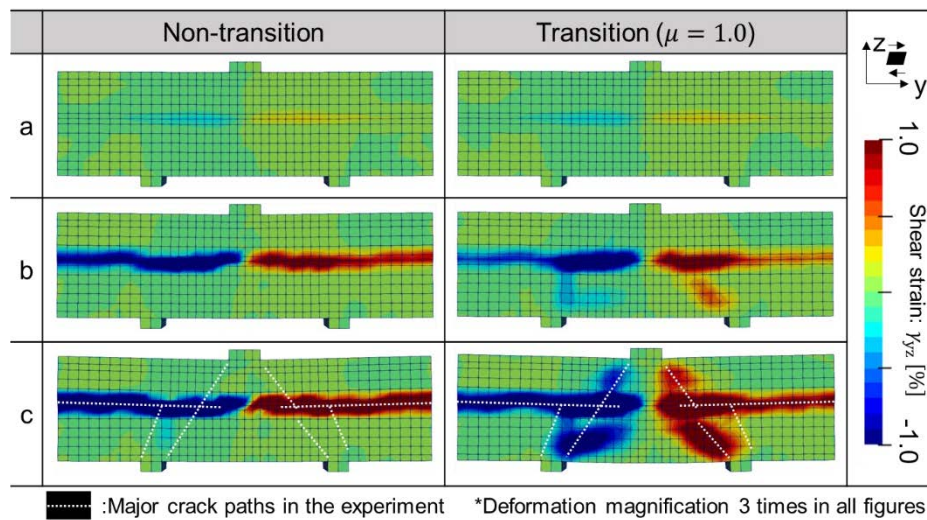


**Fig. 3-11    Shear strain localization of non-transition and transition models for Case FL-2C**

| | Non-transition | Transition ($\mu = 1.0$) |
|---|---|---|
| a | | |
| b | | |
| c | | |

:Major crack paths in the experiment    *Deformation magnification 3 times in all figures
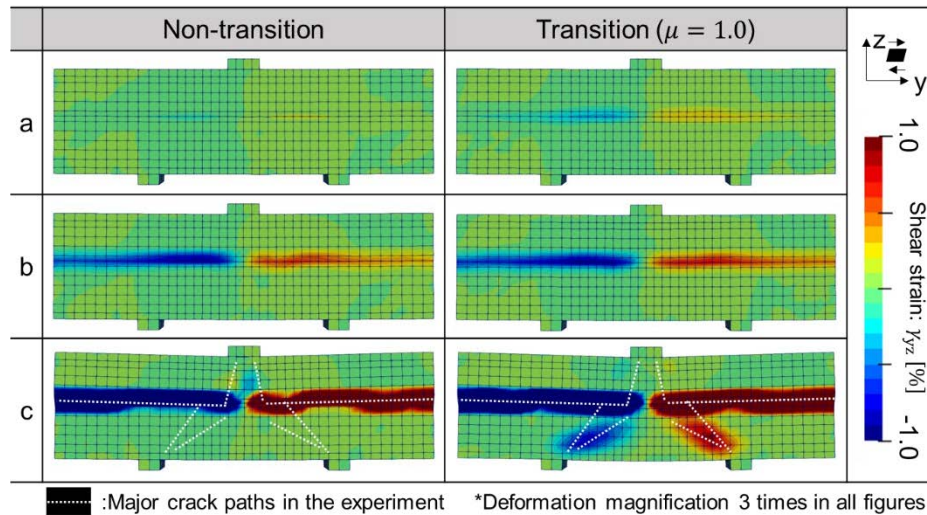
**Fig. 3-12    Shear strain localization of non-transition and transition models for Case FL-2M**

(2)  Analysis of coupled failure of each layer and joint surface (FL-8C-O)

Not only the fracture of each layer but also the failure of joint interface between low-strength concrete and high-strength concrete was appeared, since the joint surface was flatter than that of the other cases in the case of FL-8C-O as shown in Fig. 3-13. The applicability of the proposed model to this complex fracture was investigated in combination with a volumeless interface element that allows slip and opening. The integrated analysis of thermodynamics and mechanics of structural concrete was used same as the other cases. Input value is listed in Table 3-4.



(a)  Joint surface of FL-8C-O    (b)  Joint surface of FL-8C    (c)  Ultimate failure of FL-8C-O
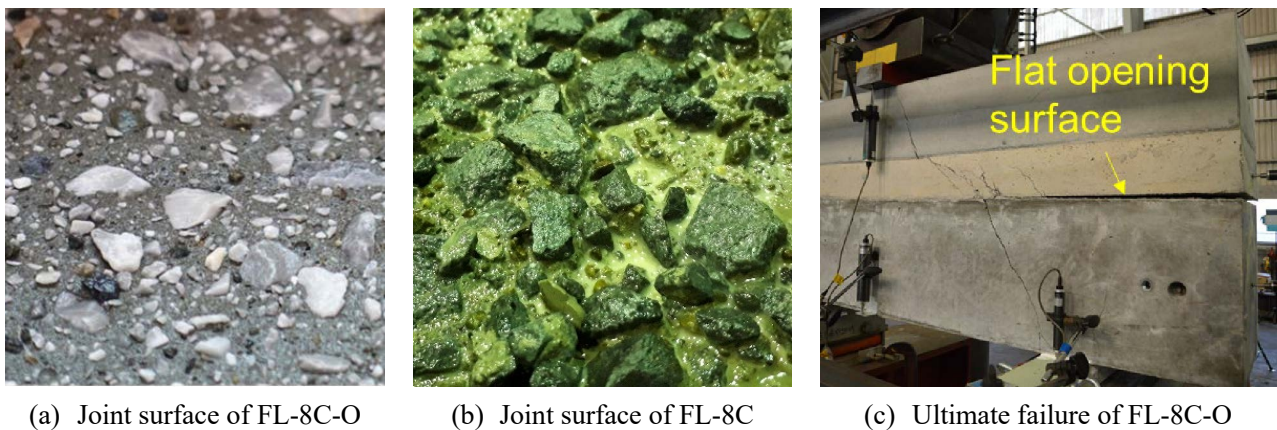
**Fig. 3-13    Joint surface and ultimate failure mode of FL-8C-O**

The different point from the other cases is the presence of joint elements between each layer as shown in Fig. 3-14. The boundary condition of integrated analysis in each analytical step is illustrated in Fig. 3-15. In the first step of creating a bottom layer made of high-strength concrete, only the bottom layer elements are activated, and the other elements are ignored in both thermodynamic and mechanics calculations. The heat and moisture transfer elements with no volume are placed on the joint surface on the bottom layer as well as the other surface so as to be sealed condition. Slips and openings are not mechanically considered here (i.e., assuming a rigid connection). In second step of casting low-strength concrete as intermediate layer, the solid elements in this layer are newly activated. The

45

free transfer condition of moisture and heat are tolerated while maintaining a rigid bond. In the same way, the upper layer is created in next step. Until 28 days had passed since the mold was removed, the sealing condition was set as an environmental condition. After another 20 days at room temperature of 20 degrees and relative humidity of 60 %, the loading step was started.

In the loading steps, the nonlinearity of the joint interface is considered according to the mechanical properties shown in Table 3-5. Elasticity is specified for compression and tension below the tensile strength, and bilinear behavior is specified for shear according to the Mohr-Coulomb friction law (Maekawa et al., 2008). The opening and closure mode can be considered by setting different stiffness for each mode. The shear strength was set according to Eq. (3-2), which represent the ultimate shear strength on the crack surface .

$$m = 3.83 f'^{\frac{1}{3}}_{c} \qquad (3-2)$$

At the lower joint interface (No.1 in Table 3-5), the strength of the weak layer was adopted as the compressive strength in the above equation. Considering the fact no slip or opening occurred at the upper joint interface in the experiment, the strength of normal concrete was adopted to the upper interface elements (No. 2 in Table 3-5). Similarly, the tensile strength was set to the value calculated by the following formula assuming the tensile strength of concrete (Japan Society of Civil Engineers, 2010).
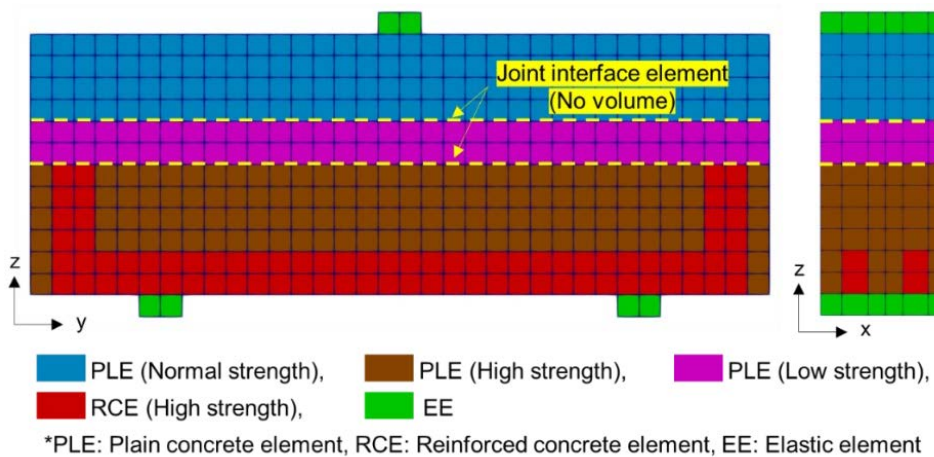
$$f_{t} = 0.23 f'^{\frac{2}{3}}_{c} \qquad (3-3)$$

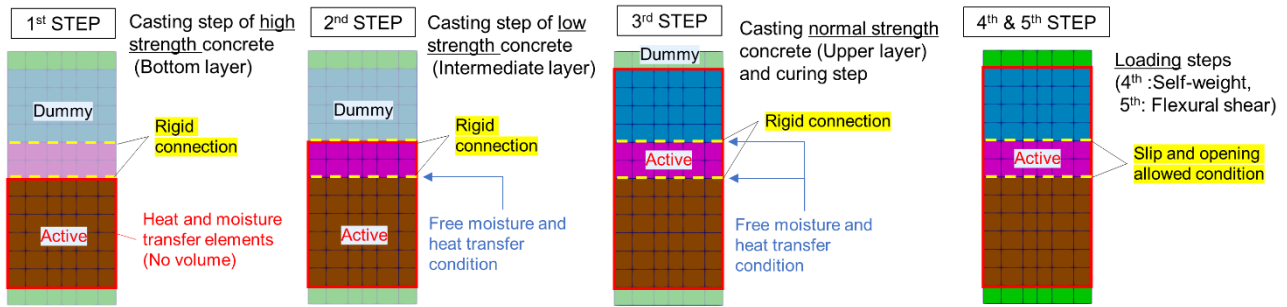**Table 3-5    Input value of each joint interface**

| No.* | $K_s^c$ | $K_n^c$ | $K_s^o$ | $K_n^o$ | $\mu$ | $f_t$ | $\tau_f$ |
|------|---------|---------|---------|---------|-------|-------|----------|
|      | [MPa/m] | [MPa/m] | [MPa/m] | [MPa/m] | [-]   | [MPa] | [MPa]    |
| 1    | 9.81E+3 | 1.96E+4 | 0.0     | 9.81E+1 | 1.0   | 7.62  | 0.91     |
| 2    | 9.81E+3 | 1.96E+4 | 0.0     | 9.81E+1 | 1.0   | 13.7  | 2.96     |

*No.1: Joint interface between **low and high strength** concrete

No.2: Joint interface between **low and normal strength** concrete



Fig. 3-14    Mesh distribution in the case of FL-8C-O

**Fig. 3-15   Boundary condition of integrated analysis in each analytical step**

The experiment and analysis results are compared in Fig. 3-16 and Fig. 3-17. The simulation can reproduce the coupling fracture of joint interface and each layer, and can estimate the ultimate shear capacity within the range of variation for each specimen (Okamura and Higai, 1980; Sigrist et al., 2013). Comparing the results of the proposed transition model and the conventional model ("Non-transition model" in Fig. 3-16), the former has a slightly larger amount of increase in strength in a large strain region. However, as can be seen from the comparison of Fig. 3-17 and Fig. 3-18, there is not much difference in the ultimate failure mode between the two analyses.

The effect of using the proposed model on the analysis accuracy was small compared to other cases where the joint interface fracture did not occur. This is because the non-linearity of the joint interface was dominant. There seems to be room for improvement in the modeling of the joint interface.

In order to clarify the cause of the discrepancy between experiment and analysis, two additional analyses were conducted in different modelling. One is the case where the initial defect is ignored by not considering the thermo-dynamics of concrete, and the other is the case where the stiffness of the sand after the transition is increased. The load-deflection relations of each case are compared in Fig. 3-19. According to the previous experimental research (Nakarai et al., 2016; Sato and Kawakane, 2008), it was confirmed that the initial defects of concrete have a great influence on the initial rigidity of structural concrete. The integrated analysis could capture this tendency and the accuracy of the simulation might be improved if the input and environmental conditions were modified so that the initial damage state was the same as in the experiment.

Moreover, it was implied that the initial set value underestimated the stiffness in large strain region, where the concrete has already transitioned to an assembly of aggregates. In the case of FL-8C with similar weak layer strength, the same tendency was confirmed. In the proposed model, the stiffness after transition is constant regardless of the compressive strength of concrete, and confinement dependency is not considered. However, as the strength of the weak layer increases, the confining pressure when graveling should increase. It is well known that the stiffness of sand largely depends on the confining pressure (Towhata, 2008). Here, priority is given to the simplicity of the model, and the sophistication of the constitutive model after the transition is an issue for future study.
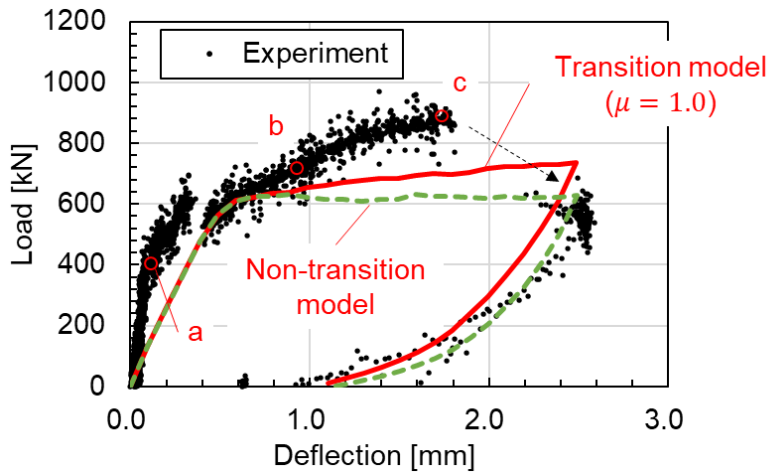
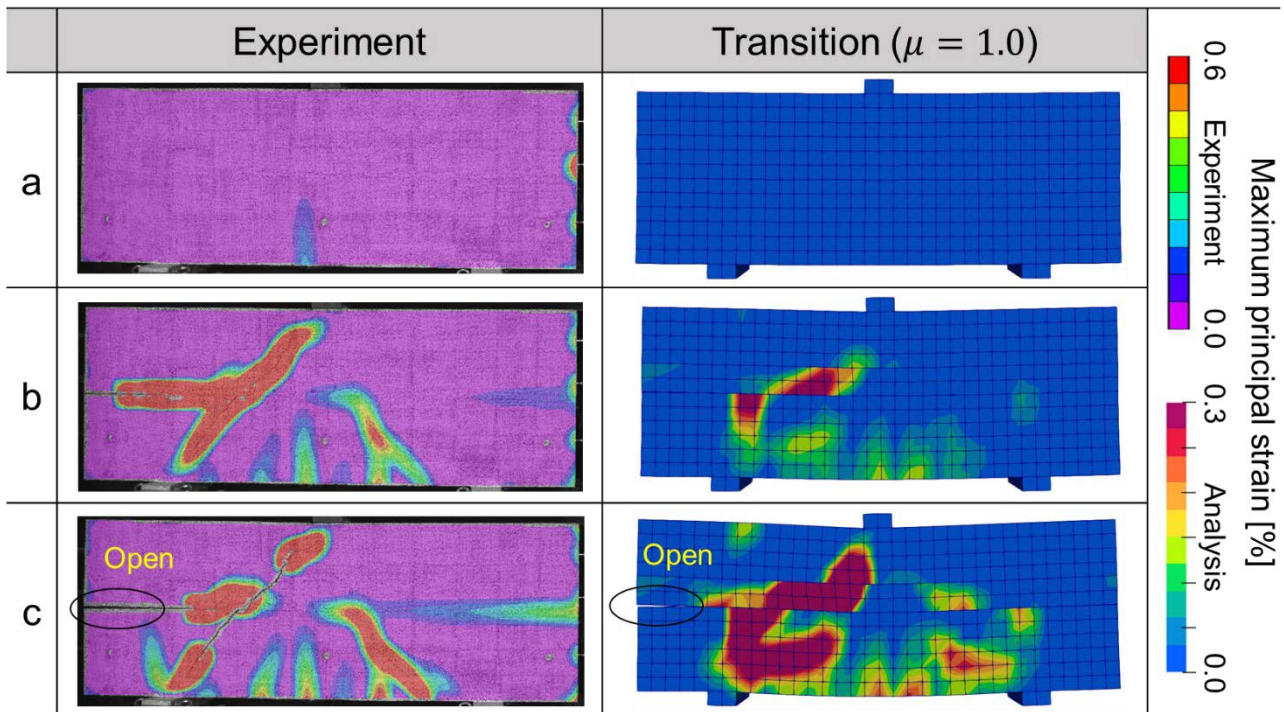**Fig. 3-16    Load-deflection relations of analysis and experiment in the FL-8C-O**



**Fig. 3-17    Comparison of deformation and strain distribution between analysis and experiment in FL-8C-O**

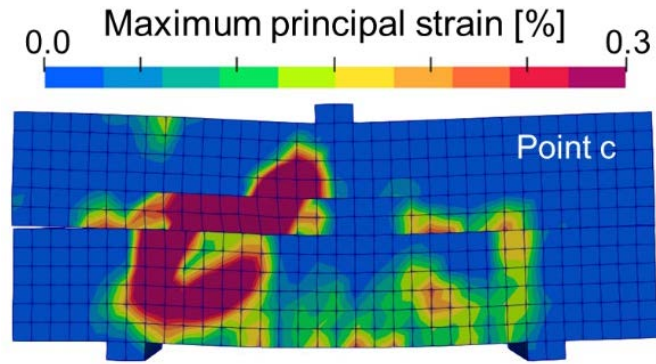**("a-c" corresponds to "a-c" in Fig. 3-16)**

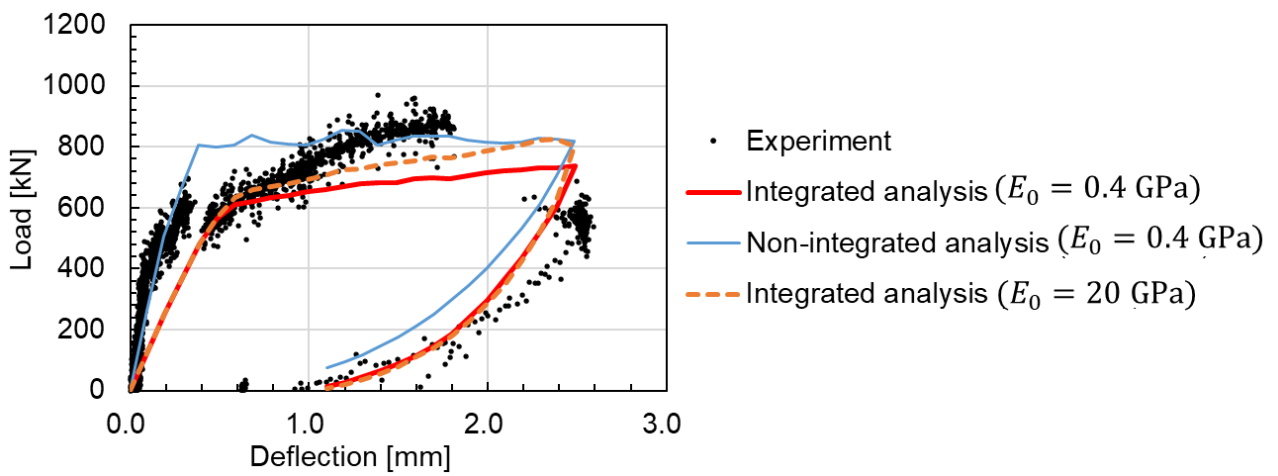**Fig. 3-18   Deformation and strain distribution of the non-transition analysis (point c in Fig. 3-16)**



**Fig. 3-19   Comparison of load-deflection relations between analyzes applied proposed model under different conditions.**

## 3.3    Sensitivity of post-transition physical properties

The validity of the proposed model has been confirmed by the previous section. In this section, the sensitivity of each parameter used in the transition model is checked. The elasto-plastic model of the transition destination requires at least four parameters. Each parameter was varied from the initially set values as shown in Table 3-6. In the series A, the effect of stiffness after transition is investigated using Young's modulus as a parameter while the effect of volume change performance is confirmed by changing the Poisson's ratio in the series B. In Series C, the coefficient of friction and in Series D, the function that expresses the degree of transition is the target of sensitivity analysis.

**Table 3-6    Parametric study case list**

| Case | $E_0$ [GPa] | $\nu$ [-] | $\mu$ [-] | $Z(K)$ [-] | Memo |
|------|-------------|-----------|-----------|------------|------|
| Base | 0.400 | 0.30 | 1.0 | $1-K$ | Input values up to Section 3.2 |
| A-1 | **0.040** | 0.30 | 1.0 | $1-K$ | Lower stiffness |
| A-2 | **4.00** | 0.30 | 1.0 | $1-K$ | Higher stiffness |
| A-3 | **20.0** | 0.30 | 1.0 | $1-K$ | Stiffness equivalent to concrete |
| B-1 | 0.400 | **0.10** | 1.0 | $1-K$ | High volumetric deformability |
| B-2 | 0.400 | **0.49** | 1.0 | $1-K$ | Low volumetric deformability |
| C-1 | 0.400 | 0.30 | **0.1** | $1-K$ | Very small friction |
| C-2 | 0.400 | 0.30 | **0.6** | $1-K$ | Friction equivalent to a friction angle of 30 deg |
| C-3 | 0.400 | 0.30 | **1.5** | $1-K$ | Very large friction |
| D-1 | 0.400 | 0.30 | 1.0 | $\mathbf{1-K^3}$ | Transition starts from a state with little damage |
| D-2 | 0.400 | 0.30 | 1.0 | $\mathbf{(1-K)^3}$ | Transition starts from a state with large damage |
| D-3 | 0.400 | 0.30 | 1.0 | $\mathbf{(1-K)^{10}}$ | Transition starts from a state with extremely large damage |

The results of parametric study are summarized in Fig. 3-20. The load bearing capacity largely depends on the Young's modulus and the coefficient of friction, but the change due to the Poisson's ratio and the transition function is small. The details of the effect of each factor and the validity of the initial settings are described below.

*Young's modulus*

In the basic case, a value similar to that of gravels consolidated under 0.5 kgf/cm$^2$ was tentatively set (Shibuya et al., 1992). However, it is well known that the stiffness of granular materials is greatly affected by various factors such as confining pressure and void ratio and the initial shear stiffness is generally expressed as following equation (Ishihara, 1996; Tatsuoka et al., 1993; Yang and Liu, 2016).

$$G_0 = AF(e)\left(\frac{\sigma'}{p^{\text{ref}}}\right)^{\text{n}} \tag{3-4}$$

where, $\sigma'$ is the mean effective stress (positive in compression); $p^{\text{ref}}$ is a reference stress; $F(e)$ is a function of the void ratio $e$; $A$ and n are arbitrary constants. These constants vary from sand to sand, and Shibuya et al. (1992) proposed an empirical equation for gravels as below.

$$E_{\max} = 1260 \left\{ \frac{(2.97 - e)^2}{1 + e} \right\} \sigma'^{0.509} \qquad (3 - 5)$$

where, $E_{\max}$ is in kgf/cm$^2$. According to the above formula, Young's modulus ranges from 0.075 GPa to 20 GPa when the confinement pressure is 10 kPa or more and 100 MPa or less. The series A covers this range, and especially when the rigidity was smaller than that of the basic case, the effect was large as shown in Fig. 3-20 (a). In reality, the restraining pressure varies greatly depending on the location inside the concrete structure. As mentioned in Section 3.2, the model can be upgraded by considering the confinement pressure dependency of the rigidity after the transition, but the calculation cost will increase, and its validity is difficult to verify. Since the provisional values are generally consistent with the experimental results, a simple model is currently adopted.

*Poisson's ratio*

As the Poisson's ratio increases with a constant Young's modulus, the bulk stiffness increases and the shear stiffness decreases, as expressed by Eq. (3-1), which result in the decrease of the volume change of elements. From the results of Series A and B, it is clarified that shear stiffness is the most influential factor that determines the overall rigidity. This is consistent with the fact that the specimen is dominated by shear failure. Poisson's ratio is about 0.2 for concrete and close to 0.5 for water. In the case of gravel, this value is between the two and changes depending on the degree of compaction, water content, and so on. However, as shown in Fig. 3-20 (b), even when the Poisson's ratio became an extreme value, the effect on the load bearing capacity was small compared to the Young's modulus, and there was no difference in the failure mode.
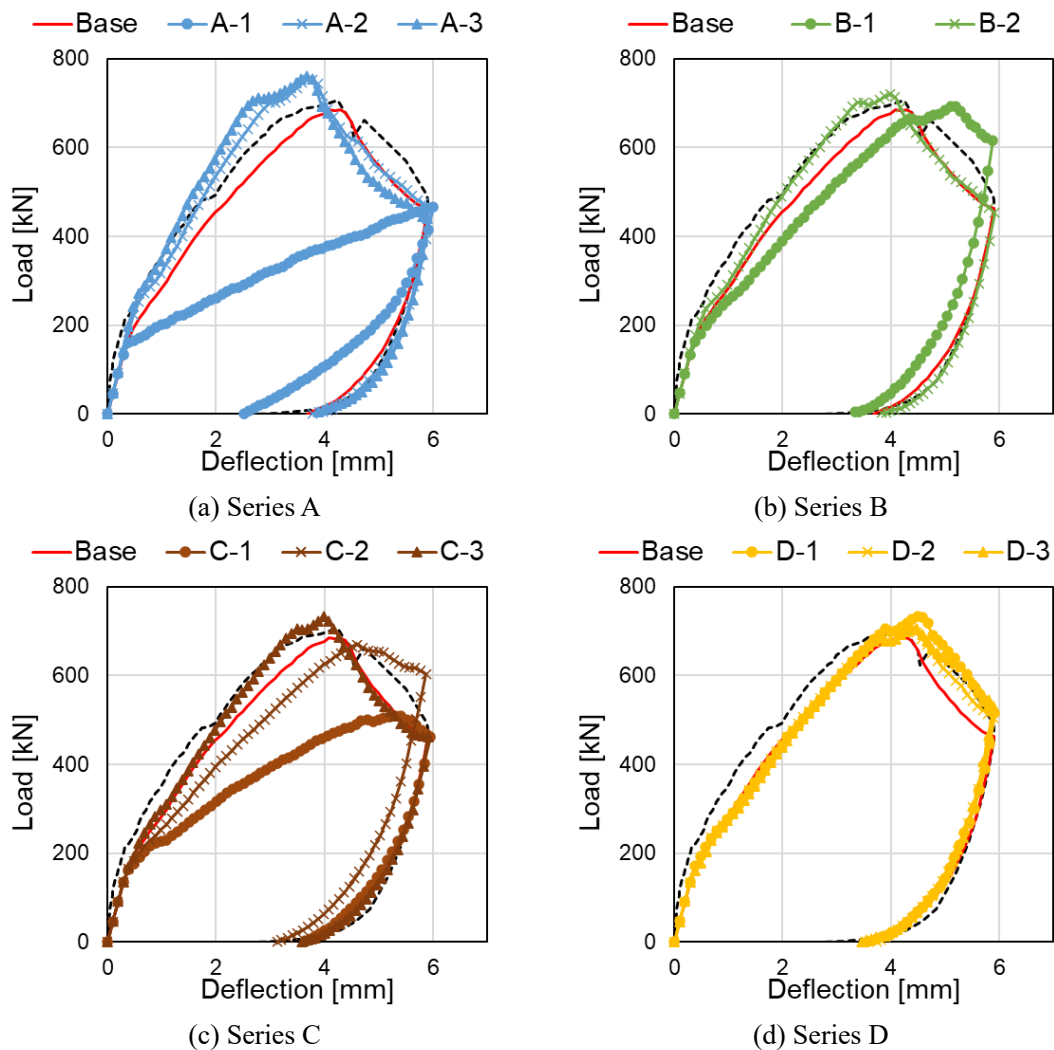
*Friction coefficient*

As shown in Fig. 3-20, rigidity and strength after disintegration is sensitive to changes in the coefficient of friction as similar to Young's modulus. The difference from Young's modulus is that plastic deformation which appears as residual deformation doesn't change even if the friction coefficient become smaller. The shear strain distributions in each case are compared in Fig. 3-21. When the shear transfer force in the weak layer becomes small due to the small friction coefficient, the shear damage in the upper layer becomes small. In this case, as shown in Fig. 3-22, the tensile strain in the span direction of the upper layer is concentrated in the central portion like an unreinforced concrete beam. This implies that the upper and lower beams have independent shear deformations. However, the specimen was finally failure by the diagonal crack penetrating upper and bottom layer, which can be captured by the analysis when friction coefficient is higher than 1.0. Therefore, it can be judged that the value identified in **Chapter 2** was valid.

*Transition function*

In the series C, the results of applying three different transition functions in addition to the basic case are compared as shown in Fig. 3-23. Differences in transition functions had little effect on load bearing capacity or failure mode. This implies that damage to the weak layer progressed rapidly. In the case of unreinforced concrete, the damage is localized, resulting in sharp softening. It may be necessary to set an appropriate transition function when the reinforcing bars are placed and the damage is dispersed, but it was confirmed that a simple linear function is sufficient for the unreinforced ones.

The post-transition physical properties required for the transition model vary depending on the constituent materials and composition of the concrete. Therefore, it is difficult to set a unique value. However, the result of parametric study implies that the coefficient of friction is the most dominant factor, and it is possible to roughly match the actual phenomenon by changing this value. In the future, if improvement of analysis accuracy is required, there is room for improvement in the constraint pressure dependence of rigidity and the transition function.



(a) Series A

(b) Series B

(c) Series C

(d) Series D

**Fig. 3-20 Sensitivity of each parameter to the load-deflection relations (Black dotted lines represent experimental results)**
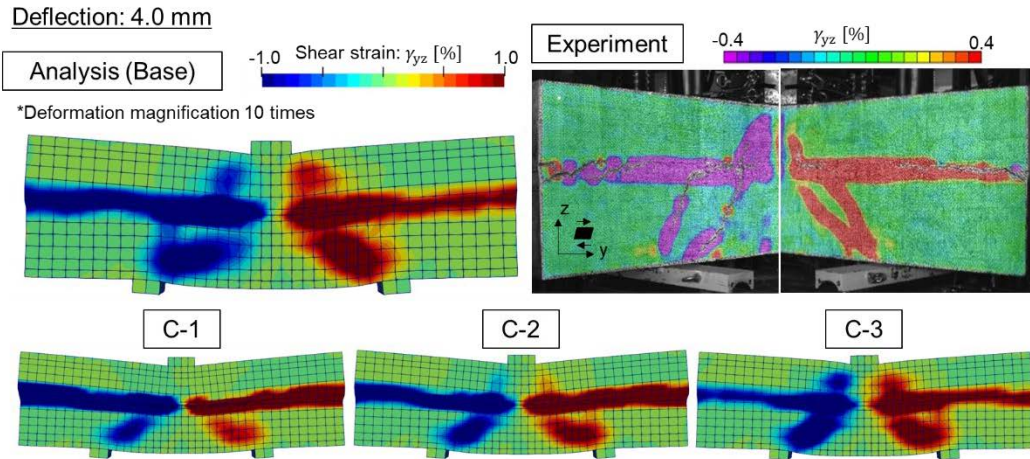
**Fig. 3-21    Changes in strain distribution due to differences in friction coefficient (Series C)**



The white dotted line connects the edges of the top and bottom loading plates.
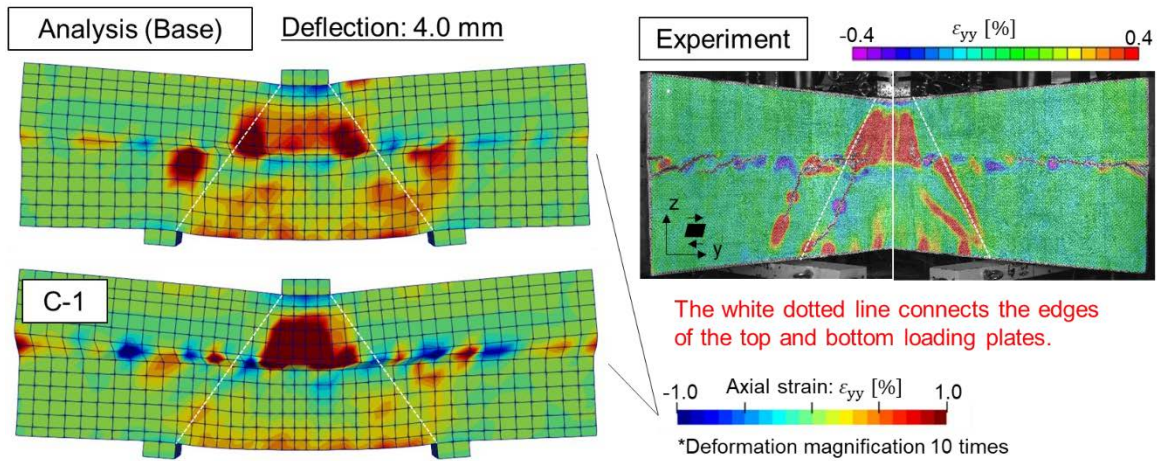
**Fig. 3-22    Changes in axial strain distribution in cases with different failure modes (Series C)**
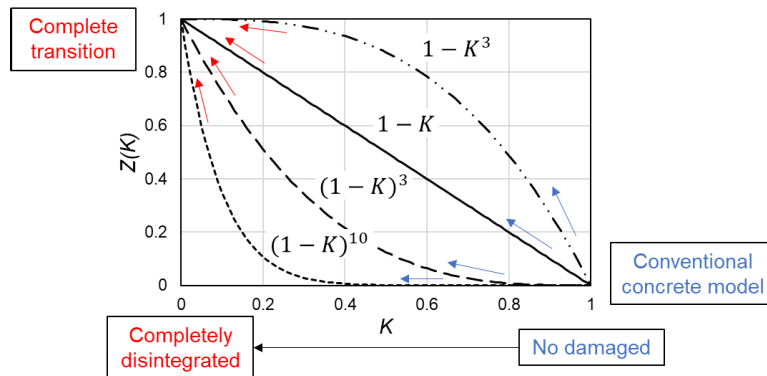


**Fig. 3-23    Relationship between the fracture parameter and transition degree for each transition function in Series D**

## 3.4     Summary of Chapter 3

From the experiment using low-strength concrete, engineering attention was directed at the fact that low-strength concrete transitions to graveling assembly as the cement paste disintegrates in the localized shear bands. The graveling of concrete with compressive strength of about 2 MPa and 8 MPa was observed in the loading test of three-layer beams, and it is clarified that the shear resistance of the low-strength intermediate layer is maintained even after the disintegration proceeds. The applicability of the proposed transition model was confirmed for these low-strength concrete. Furthermore, the applicability of the model to concrete structure subjected to coupling failure with the joint interface was also examined. The main conclusions are summarized below.

i. Even if the compressive strength is about 2 MPa, if the composite matrix has coarse aggregate, a large shear force is transferred under confinement even after great fracture. In the case of mortar, the shear transfer capacity at disintegration becomes much smaller.

ii. The transition model was confirmed to upgrade the post-peak structural analysis of reinforced concrete, especially for structural members that include very small strength layers of concrete.

iii. The frictional coefficient after the transition to graveling in the shear bands was identified as 1.0 regardless of the compressive strength of concrete. This is consistent with the findings of previously reported research on normal strength concrete.

iv. In applying the transition model to mortar, it was necessary to reduce the frictional coefficient compared to the case of concrete, and the value of 0.4 was established as the frictional coefficient mortar.

v. From the result of parametric study, it is clarified the coefficient of friction is the most dominant factor, and it is possible to roughly match the actual phenomenon by changing this value.

## References of Chapter 3

Bujadham, B., Mishima, T., Maekawa, K., 1992. Verification of the universal stress transfer model. *Doboku Gakkai Ronbunshu* 1992. https://doi.org/10.2208/jscej.1992.451_289

Cervenka, V., 2002. Computer simulation of failure of concrete structures for practice, in: *1st Fib Congress*. pp. 289–304.

Ishihara, K., 1996. *Soil Behaviour in Earthquake Geotechnics*. Clarendon Press, Oxford, UK.

Japan Society of Civil Engineers, 2010. *Standard Specifications for Concrete Structures-2007, "Design." Japan Society of Civil Engineers*, Tokyo, Japan.

Lertsrisakulrat, T., Niwa, J., Yanagawa, A., Matsuo, M., 2002. Concepts of localized compressive failure of concrete in RC deep beams. *Doboku Gakkai Ronbunshu 2002*. https://doi.org/10.2208/jscej.2002.697_215

Li, B., Maekawa, K., Okamura, H., 1989. Contact density model for stress transfer across cracks in concrete. *Journal of Faculty of Engineering*, The University of Tokyo 40, 9–52.

Maekawa, K., Fukuura, N., 2013. Nonlinear modeling of 3D structural reinforced concrete and seismic performance assessment, in: *Infrastructure Systems for Nuclear Energy*. John Wiley & Sons, Ltd, Chichester, UK, pp. 153–184. https://doi.org/10.1002/9781118536254.ch11

Maekawa, K., Fukuura, N., Soltani, M., 2008. Path-dependent high cycle fatigue modeling of joint interfaces in structural concrete. *Journal of Advanced Concrete Technology 6*, 227–242. https://doi.org/10.3151/jact.6.227

Maekawa, K., Ishida, T., Kishi, T., 2009. *Multi-Scale Modeling of Structural Concrete*, 1st ed. Taylor & Francis.

Maekawa, K., Pimanmas, A., Okamura, H., 2003. *Nonlinear Mechanics of Reinforced Concrete*. CRC Press Taylor and Francis Group, London.

Nakarai, K., Morito, S., Ehara, M., Matsushita, S., 2016. Shear strength of reinforced concrete beams: concrete volumetric change effects. *Journal of Advanced Concrete Technology 14*, 229–244. https://doi.org/10.3151/jact.14.229

Okamura, H., Higai, T., 1980. Proposed design equation for shear strength of reinforced concrete beams without web reinforcement. *Proceedings of the Japan Society of Civil Engineers 1980*, 131–141. https://doi.org/10.2208/jscej1969.1980.300_131

Sato, R., Kawakane, H., 2008. A new concept for the early age shrinkage effect on diagonal cracking strength of reinforced HSC beams. *Journal of Advanced Concrete Technology 6*, 45–67. https://doi.org/10.3151/jact.6.45

Shibuya, S., Tatsuoka, F., Teachavorasinskun, S., Kong, X.J., Abe, F., Kim, Y.-S., Park, C.-S., 1992. Elastic deformation properties of geomaterials. *Soils and Foundations 32*, 26–46. https://doi.org/10.3208/sandf1972.32.3_26

Sigrist, V., Bentz, E., Ruiz, M.F., Foster, S., Muttoni, A., 2013. Background to the fib Model Code 2010 shear provisions - part I: beams and slabs. *Structural Concrete 14*, 195–203. https://doi.org/10.1002/suco.201200066

Song, H.-W., Shim, S.-H., Byun, K.-J., Maekawa, K., 2002. Failure analysis of reinforced concrete shell structures using layered shell element with pressure node. *Journal of Structural Engineering 128*, 655–664. https://doi.org/10.1061/(ASCE)0733-9445(2002)128:5(655)

Sutton, M.A., Orteu, J.-J., Schreier, H.W., 2009. *Image Correlation for Shape, Motion and Deformation Measurements*. Springer US, Boston, MA. https://doi.org/10.1007/978-0-387-78747-3

Tatsuoka, F., Siddiquee, M.S.A., Park, C.-S., Sakamoto, M., Abe, F., 1993. Modelling stress-strain relations of sand. *Soils and Foundations 33*, 60–81. https://doi.org/10.3208/sandf1972.33.2_60

Towhata, I., 2008. *Geotechnical Earthquake Engineering*. Springer Berlin Heidelberg, Berlin, Heidelberg. https://doi.org/10.1007/978-3-540-35783-4

Vecchio, F.J., Selby, R.G., 1991. Toward compression-field analysis of reinforced concrete solids. *Journal of Structural Engineering 117*, 1740–1758. https://doi.org/10.1061/(ASCE)0733-9445(1991)117:6(1740)

Yamanoi, Y., Maekawa, K., 2020a. Damage assessment of structural concrete with sudden change in rigidity -bifurcation of localized shear-. *Master's Thesis*, Yokohama National University, Japan.

Yamanoi, Y., Maekawa, K., 2020b. Shear bifurcation and graveling of low-strength concrete. *Journal of Advanced Concrete Technology 18*, 767–777. https://doi.org/10.3151/JACT.18.767

Yamanoi, Y., Maekawa, K., 2016. The fracture mode of RC buildings attacked by the fault and the availability of the man-made-rock for damage control. *Graduation Thesis*, Yokohama National University, Japan.

Yang, J., Liu, X., 2016. Shear wave velocity and stiffness of sand: the role of non-plastic fines. *Géotechnique 66*, 500–514. https://doi.org/10.1680/jgeot.15.P.205

Yoneda, T., Ishida, T., Maekawa, K., Gebreyouhannes, E., Mishima, T., 2013. Simulation of early-age cracking due to drying shrinkage based on a multi-scale constitutive Model, in: *Poromechanics V. American Society of Civil Engineers*, Reston, VA. https://doi.org/10.1061/9780784412992.069

Zhang, N., Tan, K.H., 2007. Size effect in RC deep beams: Experimental investigation and STM verification. *Engineering Structures 29*, 3241–3254. https://doi.org/10.1016/j.engstruct.2007.10.005

# 4 Model Verification for Concrete Subjected to Cyclic Load by the Experiment of Double-Beam Coupling Beam (DBCB)

## 4.1 Coupling beam with weak layer in shear

Up to the previous chapter, an engineering attention was directed to the low-strength concrete. This capter tries to validate the model for normal strength concrete as well. There are two types of coupling beams: the conventional type consisting of longitudinal main reinforcement and transverse reinforcement, and the diagonally reinforced coupling beam surrounded by shear reinforcement (Lim et al., 2016; Naish et al., 2013). Choi et al., (2018) proposed the Double-Beam Coupling Beam (DBCB). In DBCB, reinforcement cages are arranged in two stages, and the central part is unreinforced. The unreinforced part may absorb the shear deformation, and the upper and lower parts are bent and damaged like double beams. Despite the relatively simple reinforcement arrangement, greater toughness is exhibited throughout the structure. It is expected that the central unreinforced part will undergo large shear deformation locally, and the damage level will exceed the applicable range of the existing concrete constitutive model. In addition, when the concrete structure is subjected to cyclic deformation, graveling will easily proceed. Thus, the authors conducted the FE-analysis of the cyclic loading experiment of DBCB as shown in Fig. 4-1 by Choi & Chao (2020).



(a) Specimen (R2.4-SC-W)  (b) Loading test setup
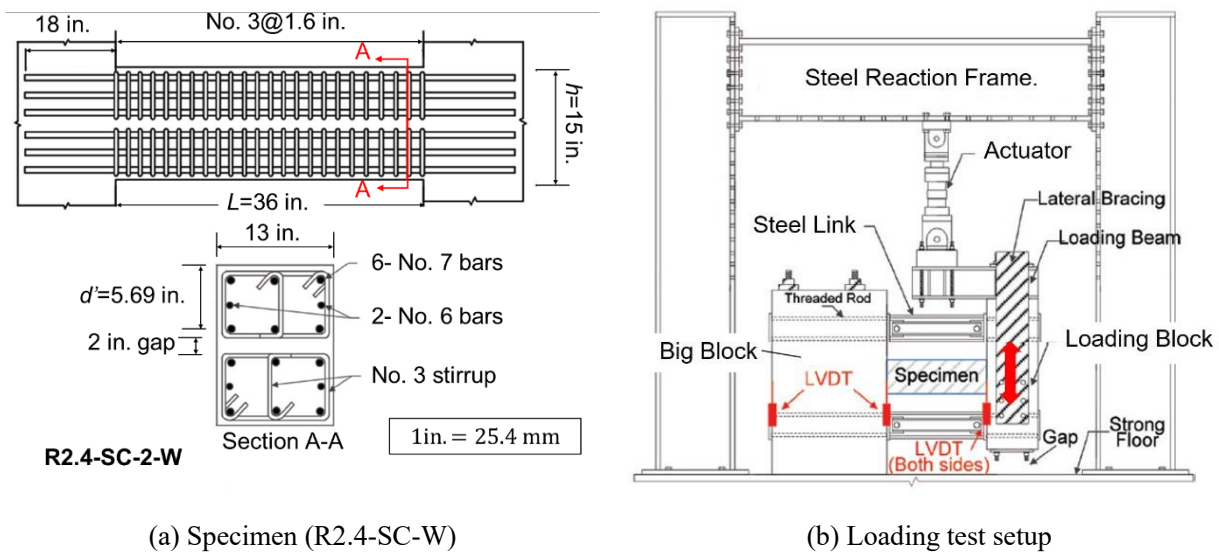
**Fig. 4-1 Experimental setup (Partially added to Choi et al. (2018); Choi & Chao (2020))**

## 4.2    Applicability of the proposed model

The analysis model is shown in Fig. 4-2 and the physical characteristics are shown in Table 4-1. As in the previous chapter, a multi-directional smeared crack model was applied to concrete. The compressive strength was computationally set to the measured value at the test, and Young's modulus and tensile strength were set based on the JSCE code specification (Japan Society of Civil Engineers, 2010) from the compressive strength of concrete. In the previous chapter, as the different types of concrete were mixed, the different drying shrinkage may cause self-equilibrated stresses. This effect of differential shrinkage was considered by using the integrated analysis of the coupled thermo-dynamic-mechanistic analysis. As the shrinkage characteristics are uniform in this experiment, the stand-alone structural analysis was conducted (Maekawa et al., 2003). The beam is idealized to be monolithically connected to the side end blocks by sharing the nodes at the plane of interface. The side end blocks were idealized with the perfect elastic elements. It means mechanically that main reinforcement is perfectly anchored inside the side blocks and that the pullout of main reinforcement from the blocks is not considered in the numerical analysis. In general, when the axial tension-flexure actions are dominant with large bar diameter of reinforcing bars used, pullout of main reinforcement is to be considered in some cases (Ishibashi et al., 2000). In this study, the authors neglected the bar pullout since the major action is in shear and the distance between end blocks were experimentally confined.

As shown in Fig. 4-2, the displacement of the lower and side surfaces of the fixed block was confined, and the upper and lower surfaces of the loading block were forcibly displaced. The loading block is always displaced while maintaining parallelism with the fixed block. In the experiment, since the loading block is connected to the fixed block by a steel link, strictly speaking, horizontal displacement occurs in the direction in which the specimen is shortened as the vertical displacement increases. However, the maximum deformation angle loaded in this experiment was about 6 degrees, which is equivalent to 10% of the beam chord rotation. As the displacement error due to the elastic deformation of the steel link and the engagement of the jig is also occurable, it was judged that the horizontal displacement can be ignored. The transition model described in **Chapter 2** was applied to the reinforced and unreinforced concrete parts, and the average friction coefficient of graveling specified in the same chapter was set ($\mu = 1.0$).
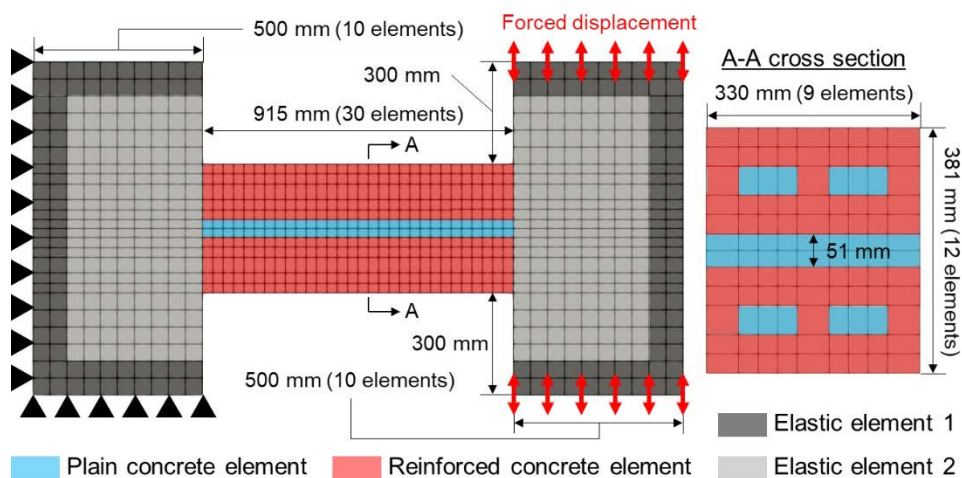


**Fig. 4-2    Mesh discretization of DBCB**

**Table 4-1  Input values for DBCB analysis**

| Element* | Property |
|---|---|
| PLE, RLE | $f'_c$ = 30.3 MPa, $E_c$ = 28.0 GPa, $f_t$ (tensile strength) = 1.34 MPa |
| RLE | $f_y$ (yield strength of rebar) = 414 MPa, |
| EE1 | Elasticity = 206 GPa |
| EE2 | Elasticity = 28.0 GPa |

*PLE: Plain concrete element, RLE: Reinforced concrete, element, EE1, 2: Elastic element 1, 2

Fig. 4-3 shows a comparison of the shear force-beam chord rotation relation of experiments and analysis and Fig. 4-4 shows a comparison of damage modes. In the experiment, the unreinforced section in the middle was proactively damaged, and in the ultimate state, it became so disintegrated that the concrete cover was peeled off. On the other hand, a large residual strength was maintained even in this state. Both figures indicate the results of the transition analysis from concrete to disintegrated graveling and the conventional one not to consider it. The DBCB reaches its maximum strength when cracks occur in the unreinforced section. As the deformation angle increases, the damage to the unreinforced part increases, but the ductility is large, and it has a residual strength of 60 % or more even after peak loading. These behaviors of the experiment can be reproduced with transition of shear localized bands accurately. When the non-transition model was used, the damage at the joint between the beam and the loading block became dominant, resulting in unrealistically small strength and ductility.

Focusing on the damage when the deformation angle is 3 %, shear cracks occur on the diagonal line of the beam in the experiment. This means that the damaged unreinforced part maintains shear transfer. In the non-transition analysis, the damage is concentrated in the unreinforced part and the joint between the beam and the loading block, and it behaves like in a non-synthetic beam. This means that the shear transfer of the unreinforced part during large shear deformation can be evaluated to be small. When the transition model is applied, there is a tendency to overestimate the energy absorption capacity during cyclic loading. Similar trends are seen when damage to the beam-loading block joint is dominant (Choi et al., 2018; Lim et al., 2016; Naish et al., 2013). The model of fully disintegrated concrete in Eq. (2-1) is described simply by the elasto-perfect plasticity model whose yield strength has confinement dependency. In this case, the shear stress-slip strain relation gets point symmetry without so called Bauschinger effect. This simplicity may bring about less pinched force-displacement relation under smaller restoring forces. The enhancement of the hysteretic model of disintegrated concrete composite is required in future progress.

The authors integrated the existing concrete model with a soil foundation modelling by means of the most simple and clear way. Although there is room for further improvement in the modeling, the structural analysis of the post-peak was greatly improved with this simple modification. Even when normal-strength concrete is used, if the concrete continues to undergo large shear deformation beyond the maximum capacity, it is necessary to consider the behavior of transition from concrete to disintegrated graveling.

(a) Conventional concrete model                    (b) Proposed transition model
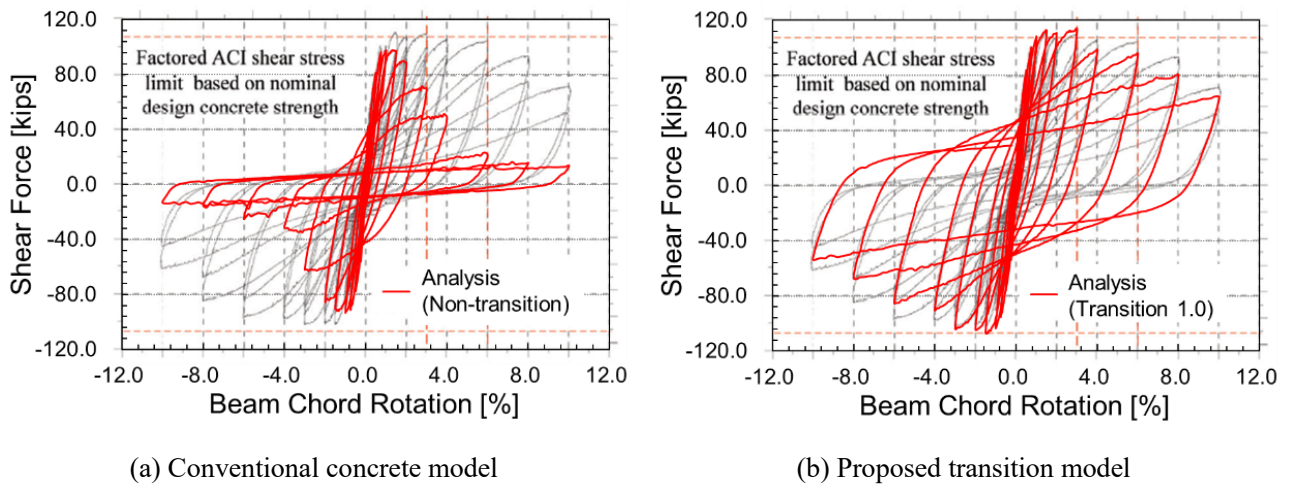
**Fig. 4-3    Comparison of hysteresis responses between analysis and experiment (Analysis results are added to experimental data of Choi & Chao (2020))**
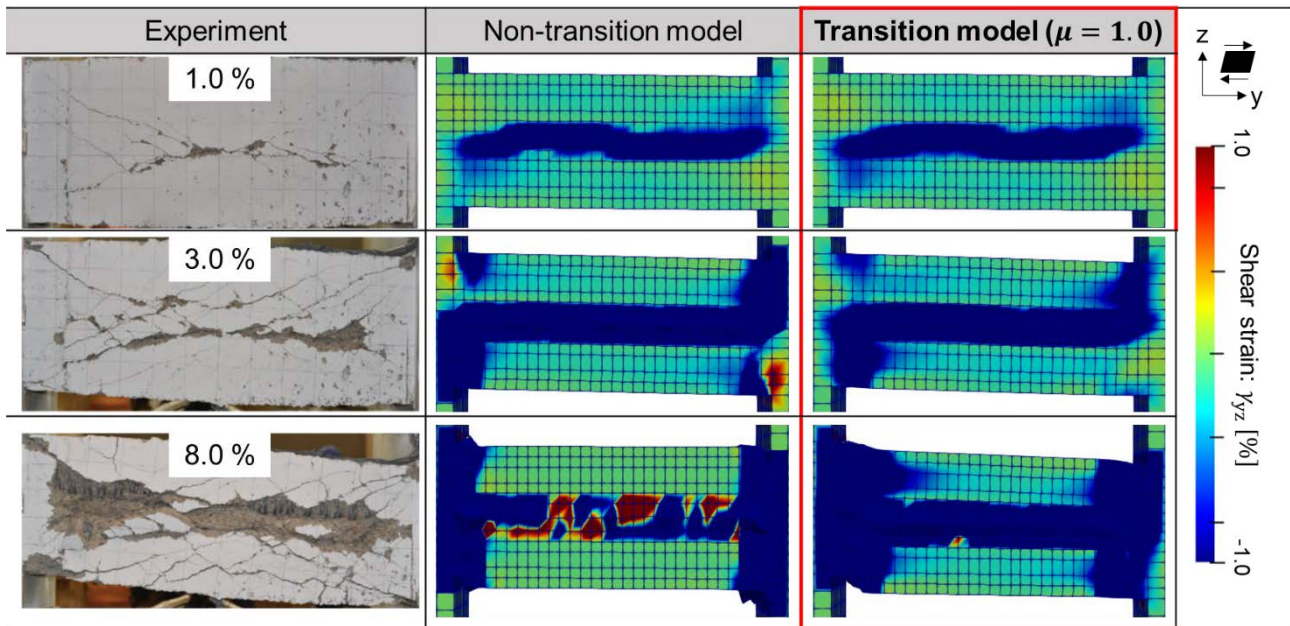


**Fig. 4-4    Comparison of analysis results using the proposed transition model and conventional concrete model (photo taken by Choi & Chao (2020))**

Next, the sensitivity of the coefficient of friction in the ultimate state was checked as shown in Fig. 4-5. The maximum shear force does not change significantly even if the coefficient of friction changes from 1.0 to 0.6. On the other hand, the residual strength is greatly affected by the friction angle, and 45 degrees (equivalent to the coefficient of friction of 1.0) appears highly consistent with the experimental result. It was confirmed that the transition model can be applied not only to low-strength concrete but also normal-strength concrete when the disintegration of the composition becomes significant.
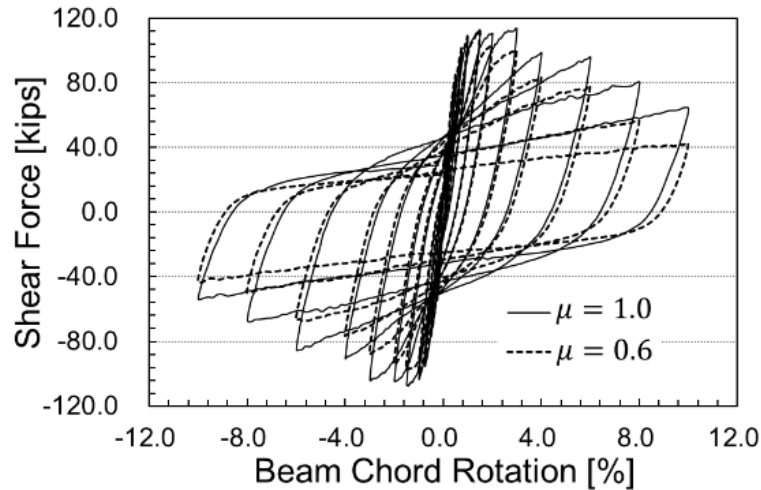
**Fig. 4-5  Sensitivity of the ultimate friction in the transition model (DBCB).**

4.3        Multi-layer composite with high-strength concrete

As mentioned in the previous section, it is necessary to consider the transition of shear transfer characteristics in the localized shear bands even for ordinary strength concrete. The transition model was applied only to the weak layer in **Chapter 3** for verification and validation. In this section, the model will be also examined by focusing on the normal and high-strength concrete of the multi-layer composite.

  Fig. 4-6 shows a comparison between the analysis of applying the transition model only to the weak layers as shown in **Chapter 3** and the analysis of applying the transition model to all layers including the normal and high-strength concrete. In the two cases, except for the weak layer of mortar, consideration of the transition of shear transfer characteristics of the normal strength layer ($f'_c \approx 45$ MPa) and the high strength layer ($f'_c > 100$ MPa) leads to a structural capacity increase of about 10%. It is considered that the little gain in capacity can be attributed to the restraint dependence of shear by the bending compression.

  Since the strength of the hardened cement paste exceeds that of aggregate for high strength concrete, coarse aggregate particles are split into two pieces at crack planes. As a result, the aggregate interlock mechanism is almost lost. Because of no contact forces to already split aggregates, further graveling hardly proceeds unlike the case of low-strength concrete. Thus, it is estimated that the greater strength concrete may also have less graveling as disintegration unless subjected to the high-cycle fatigue load. In this case, as mentioned in **Chapter 1**, there has already been the numerical model for the graveling concrete subjected to the high-cycle fatigue load under the wet condition. The applicability of the transition model was verified for concrete with a compressive strength of about 30 MPa in the section 4.2. Then, the authors propose Eq. (4-1) for normal and high-strength concrete. Combining this model with the existing one can provide a numerical model that integrates low-cycle graveling of the low-strength materials and high-cycle graveling of all strength concrete, as shown in Fig. 4-7.

  The validity of setting 30 MPa as the threshold value and the relationship between the cyclic number and the progress of graveling would be investigated in the future.

$$\sigma_{ij} = \sigma_{rcij}(K) + \alpha(1 - K) \cdot \sigma_{sij} \qquad (4-1)$$

$$\alpha = \begin{cases} 0.0 & (f'_c \geq 30.0) \\ 1.0 - \dfrac{f'_c - 10.0}{20.0} & (10.0 \leq f'_c < 30.0) \ [MPa] \\ 1.0 & (f'_c < 10.0) \end{cases}$$
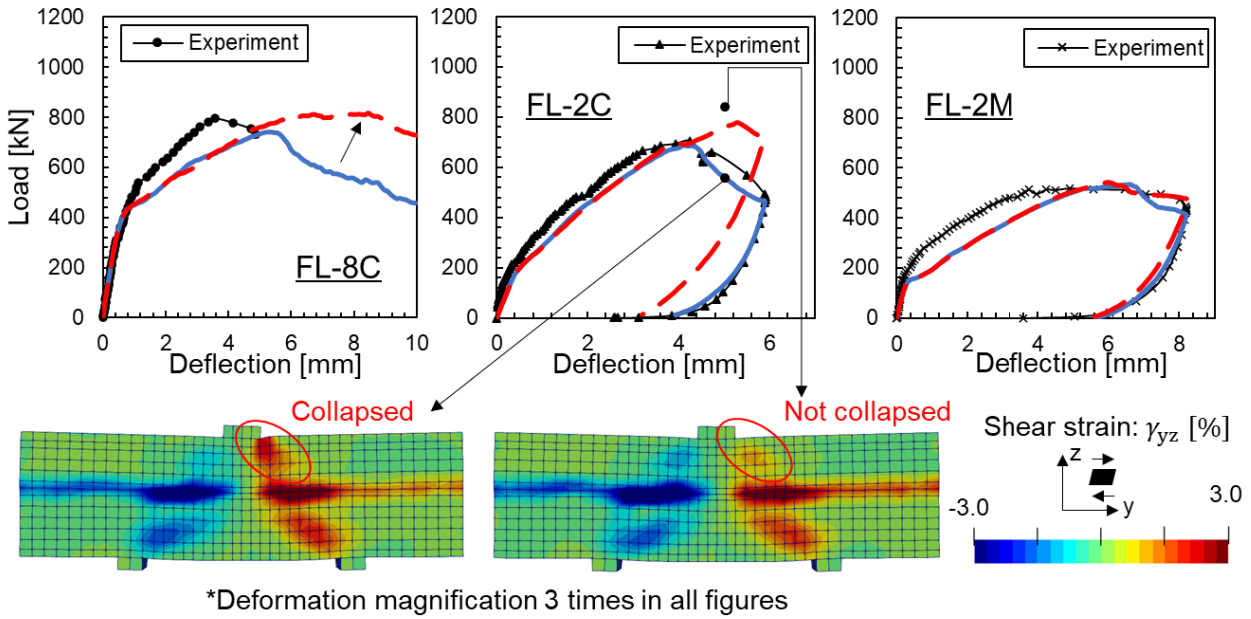


**Fig. 4-6　Effect of transitional shear transfer characteristics of concrete other than weak layers**
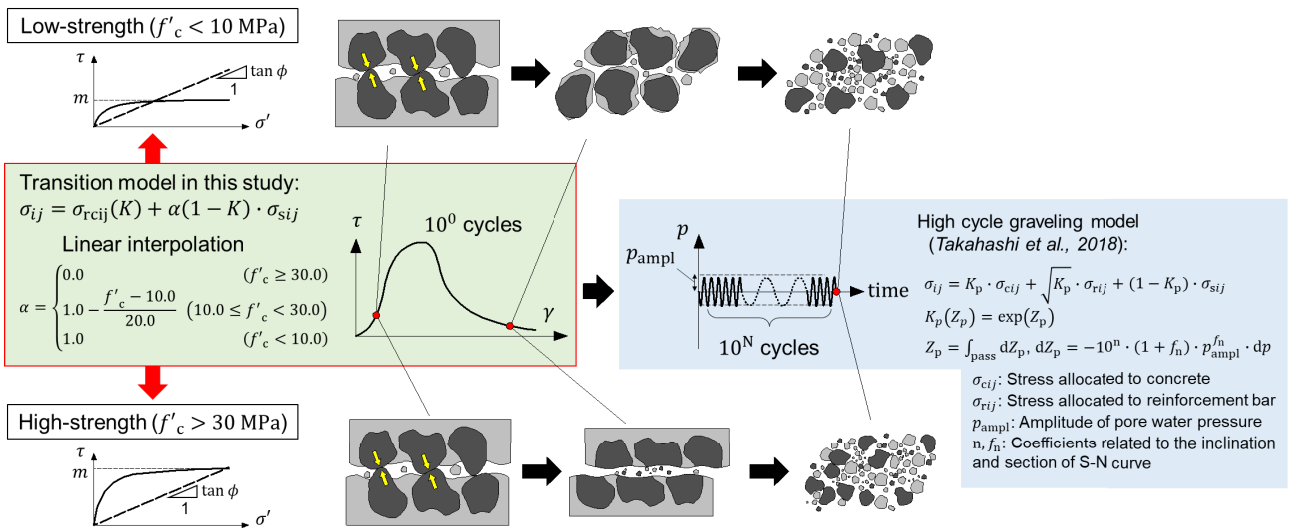


**Fig. 4-7　Integral scheme of low cycle graveling for the low-strength materials and high cycle graveling of the high strength concrete**

## 4.4    Summary of Chapter 4

The previous reported cyclic shear loading test of Double-Beam Coupling Beam (DBCB) was chosen as a verification target because its unreinforced concrete as an intentional weakness of will undergo large shear deformation locally, and the damage level will exceed the applicable range of the existing concrete constitutive model. In the experiment, the unreinforced section in the middle was proactively damaged, and in the ultimate state, it became so disintegrated that the concrete cover was peeled off. On the other hand, a large residual strength was maintained even in this state. It was confirmed that proposed transition model originally developed for low-strength concrete can be applied to DBCB made of normal-strength concrete. The main conclusions are given below.

i. The proposed model can accurately evaluate the capacity and ductility of DBCB.

ii. There was room for improvement of the model regarding cyclic behavior.

iii. It was also revealed that the load bearing capacity may be overestimated in the case of the higher strength-concrete subjected to the monotonic loading.

iv. Since the applicability of the transition model was verified for concrete with a compressive strength of about 30 MPa by this experiment of DBCB, an upper limit of 30 MPa was set on the strength of concrete to which the transition model is applied.

References of Chapter 4

Choi, Y., Chao, S.H., 2020. Analysis and design of double-beam coupling beams. *ACI Structural Journal 117*, 79–95. https://doi.org/10.14359/51725985

Choi, Y., Hajyalikhani, P., Chao, S.H., 2018. Seismic performance of innovative reinforced concrete coupling beam-double-beam coupling beam. *ACI Structural Journal 115*, 113–125. https://doi.org/10.14359/51700951

Ishibashi, T., Kobayashi, K., Umihara, T., 2000. Study on quantity evaluation of pull out of longitudinal bar from footing of RC. *Doboku Gakkai Ronbunshu 2000*, 43–54. https://doi.org/10.2208/jscej.2000.648_43

Japan Society of Civil Engineers, 2010. *Standard Specifications for Concrete Structures-2007, "Design." Japan Society of Civil Engineers*, Tokyo, Japan.

Lim, E., Hwang, S.J., Cheng, C.H., Lin, P.Y., 2016. Cyclic tests of reinforced concrete coupling beam with intermediate span-depth ratio. *ACI Structural Journal 113*, 515–524. https://doi.org/10.14359/51688473

Maekawa, K., Pimanmas, A., Okamura, H., 2003. *Nonlinear Mechanics of Reinforced Concrete*. CRC Press Taylor and Francis Group, London.

Naish, D., Fry, A., Klemencic, R., Wallace, J., 2013. Reinforced Concrete Coupling Beams-Part I: Testing. *ACI Structural Journal 110*, 1057–1066.

# 5　Application of the Transition Model to Masonry Structures

## 5.1　Multi-Directional Fixed Crack Model Extended to Masonry Structures

### 5.1.1　Review of the analytical model of masonry structures

Masonry structures have a long history and are still effectively used today, but numerous instances of earthquake damage to such structures have been reported (Bruneau, 1995; Coburn and Spence, 2002; Hisada et al., 2004; Javed et al., 2006; Mukai et al., 2016). Aiming for more sophisticated seismic capacity evaluation, methods for evaluating the seismic performance of existing masonry structures have been developed. One such method is to represent the mortar joint and the masonry block by separate structural elements, each of which is given a constitutive model (Hashimoto et al., 2017, 2014; Lourenço and Rots, 1997; Pandey and Meguro, 2004). In addition, a method to obtain the response of a masonry structure has been proposed by describing the space-averaged behaviors of masonry components including the mortar joint in a constitutive model (Fig. 5-1). The former can analyze the structural response and the behavior of the constituent materials in detail. The latter can analyze large-scale and complexly shaped masonry structures rationally and with a small number of degrees of freedom by dividing them into a small number of finite elements.
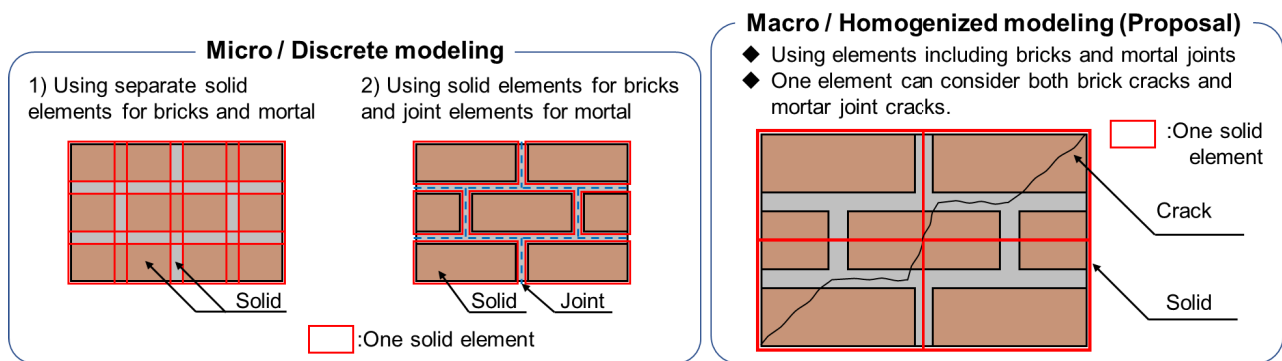


**Fig. 5-1　Behavioral Modeling of Masonry Structures in terms of Referential Volume**

Lourenço et al. (2007) have proposed a non-linear model of masonry structures in which mortar joint deformation is prominent. Maier et al. (1991) have proposed an isotropic damage model for each of the blocks and mortar joints that make up the masonry structure. Facconi et al. (2014) have formulated the local stress-strain relationship of mortar joint and designed a constitutive model considering anisotropy.

These models focus on the nonlinearity of mortar joint. The constituent blocks are represented by elastic bodies or nonlinear materials that allow for cracking in one direction. To the best of the authors' knowledge, there are no analysis models that can handle the state where cracks intersect in multiple directions within masonry blocks in having interaction with multi-directional masonry joints. When the strength of the mortar joint exceeds that of the masonry block, or in a masonry structure where the periphery is reinforced with RC columns, fracture damage to masonry blocks is often inevitable. In view of the above, the objective of this chapter is to present a structural model that may take into account both the complex fracture of the structural blocks and the local deformation of joints.

For the behavioral analysis of RC structures under reversed cyclic loading, a constitutive model to consider non-orthogonal cracking in up to 6-directions has been developed (Maekawa and Fukuura, 2013). Then, the authors

propose a method in which the possible crack axis is fixed in the direction of the joint planes to represent the response of the joints (3-directions), and a multi-directional crack model (another 3-directions) is further provided for the evaluation of damage that develops in the masonry blocks, as in the conventional model. The accuracy and applicability of the multi-directional crack model extended to masonry structures is validated experimentally.

### 5.1.2    Proposed model for masonry structures

#### (1) Allocation of crack coordinates to masonry joints

An RC in-plane constitutive model to deal with interacting two-way cracking has been formulated based on the active crack method (Okamura and Maekawa, 1991). Later, it was extended to three-dimensional stress fields (Fukuura and Maekawa, 1998; Hauke and Maekawa, 1999). Currently, a constitutive model that can consider non-orthogonal cracking in 6 directions is used (Maekawa and Fukuura, 2013). An outline is shown in Fig. 5-2. For 3-directional quasi-orthogonal crack planes, a non-orthogonal coordinate system is applied. Further, a 3D space averaged constitutive law for a total of six directions of crack groups has been formulated by adding a new crack coordinate system.

The authors opted to allocate one of the above two quasi-orthogonal crack coordinate systems to mortar joint planes orthogonal to each other. The remaining quasi-orthogonal coordinate system was allocated to the behavioral analysis of the constituent blocks (Fig. 5-2). The opening of the joint was defined if the stress normal to the mortar joint plane exceeds the tensile strength of the joint ($\beta f_\mathrm{t}$ in Fig. 5-2). A tensile strain softening model is applied to subsequent deformations ($\sigma'_1$ in Fig. 5-2). It goes without saying that this crack coordinate system is spatially fixed parallel to the joints.

When the maximum principal stress in the masonry block exceeds the tensile strength, a second crack coordinate system is mobilized. This makes it possible to handle kinetics in which multiple cracks occur not only in mortar joint but also in masonry blocks under complex load histories. The crack criterion and the shear transfer characteristics of cracks can be set separately for the mortar joint and block.

The slip and the opening modes are considered for space-averaging in which a set of block joints within a finite element forms a continuous plane. On the other hand, in the space-averaging process where masonry joints may intersect discontinuously, the bricks or blocks interlock. In this case, only cracks in the opening mode are considered. This makes it possible to handle various ways such as British and Flemish bond brick works.

#### (2) Disintegrated cementitious composites on masonry joints

For a finite region with multi-directional intersecting cracks, the active crack plane that dominates the nonlinearity is selected (Maekawa et al., 2003). The material constitutive model of compression, tension, and shear is applied to this plane as expressed in **Chapter 2**. The stresses carried by cracked concrete can be obtained as a result.

For the shear stress-shear strain relationship along the crack plane, a shear transfer model based on the contact density function was applied (Li et al., 1989). This model represents the aggregate interlock resulting from the restricted rotation of cemented aggregates. The shape of the crack plane is determined by the contact density function with respect to the contact angle. In other words, the differences in crack plane's shape and shear transfer characteristics between concrete and mortar can be reflected in the analysis. This was also applied to the mechanics of masonry blocks. The concrete-to-sand transition model (Yamanoi and Maekawa, 2020), which represents the transient shear

mechanics from cementitious materials to a sand particle assembly with shear slip, was used as the shear transfer model on the crack surface in the mortar joint direction. In the transition model originally formulated in a three-dimensional stress field, the vertical displacement of the joint is negligibly small compared to the shear slip displacement and it was assumed that the entire element would undergo graveling. Therefore, the existing concrete-to-sand transition model was degenerated to a two-dimensional joint plane here.

$$\tau_{cr} = (1 - \alpha)\tau_c + \alpha\tau_s \qquad (5-1)$$

where, $\tau_{cr}$ is the total shear transfer stress on the crack surface, $\tau_c$ is the shear transfer stress calculated based on the contact density model (Li et al., 1989), $\tau_s$ is shear transfer stress based on the friction law and $\alpha$ is mixture ratio of concrete particle assembly. Shear stress component $\tau_s$ of the sand particle assembly is represented by the elaso-perfect plastic model subject to the Coulomb friction law based on the cohesive strength: $c$, which is set equal to the tensile strength of concrete, and the friction coefficient: $\mu$ as,

$$d\tau_s = G_m d\gamma_{cr} \quad ...f < 0 \qquad (5-2)$$

$$d\tau_s = 0 \qquad ...f = 0$$

$$f = \tau_s - c + \mu\sigma_n, \qquad (5-3)$$

where, $d\gamma_{cr}$ is the incremental of the crack shear strain; $G_m$ is the shear stiffness of the mortar joint; and $\sigma_n$ is the normal stress perpendicular to the cracked surface. The authors decided to use the state function denoted by "$\alpha$" in Eq. (5-1) and Eq. (5-4) to represent the process by which the consolidation of mortar joint by cement disintegrates as shear slip progresses and transitions to a sand particles aggregation model.

$$\alpha = 1.0 - \exp(-A(\gamma - B)) \qquad (5-4)$$

where, $A$ and $B$ are constants. The coefficient $B$ representing the start point of the transition, is set to $1.0 \times 10^{-4}$ so that no transition occurs in the elastic region. The coefficient $A$, which governs the slope of the $\gamma$-$\alpha$ relation, was inversely estimated from the experimental results.

The above equation is a one-dimensional constitutive equation, but the slip on the cracked surface in the three-dimensional space is represented by the independent two-way slip. The shear stress and strain When determining the elasto-plastic state and the degree of transition, the equivalent shear stress and strain expressed by the following equations were used. In addition, the transition is considered only for the shear transfer characteristics, and the opening / closure (dilatancy) of the cracked surface follows the existing crack model.

$$\tau_s = \tau_{eq} = \sqrt{\tau_{xy}^2 + \tau_{xz}^2}, \qquad \gamma = \gamma_{eq} = \sqrt{\gamma_{xy}^2 + \gamma_{xz}^2} \qquad (5-5)$$

where, $\tau_{eq}$ and $\gamma$ are equivalent shear stress and strain on the crack surface; ($\gamma_{xy}$, $\gamma_{xz}$) and ($\tau_{xy}$, $\tau_{xz}$) are the strain and stress components on the crack surface (x-direction coincides with the one normal to the joint plane). When calculating the stress in the concrete crack model, the shear strain of the crack coordinate system is decomposed into the slip strain on the two quasi-orthogonal crack planes according to each loading condition as shown in Fig. 5-3. On the other hand, in the model after graveling, shear strain in the cracked coordinate system is regarded as the slip strain in the active cracked surface.

## Space-averaged constitutive model of concrete with multi-directional cracks

**No crack**

$\sigma_1$

**1st crack coordinate system (x1, y1)**

$\sigma_1 \geq f_t$

*x1 coincides with the maximum principal stress direction.*

$22.5° < \theta < 67.5°$

$\theta > 67.5°$

**2nd crack coordinate system (x2, y2)**

*In 2D, cracks in up to 4 directions can be considered. ⇒6 directions in 3D.*

## Proposal masonry model

**No crack**

$\sigma_x \geq \beta f_t$ or $\sigma_y \geq \beta f_t$

$\sigma_1$

**1st crack coordinate system (x1, y1)**

Joint cracks

$\sigma'_1$

$\beta$: Ratio of tensile strength of joint mortar to tensile strength of brick

*x1 coincides with any of the axes of the global coordinate system (=mortal joint directions).*

$\sigma'_1 \geq f_t$ and $22.5° < \theta < 67.5°$

$\sigma_x \geq \beta f_t$ or $\sigma_y \geq \beta f_t$

**2nd crack coordinate system (x2, y2)** Brick cracks

Joint cracks

*In 2D, two-way cracks at joints and two-way cracks at bricks can be considered. ⇒Three-way and three-way cracks in 3D.*

**Fig. 5-2    Extension of Non-Orthogonal Multi-Directional Crack Modeling**

## Shear $\tau_{xy}, \tau_{yz}, \tau_{zx}$

$\boldsymbol{\tau = G * \gamma = \tau_{cr1} = \tau_{cr2}}$

$G = 1/(1/G_c + 1/G_{cr1} + 1/G_{cr2})$

$\boldsymbol{\gamma = \gamma_c + \gamma_{cr1} + \gamma_{cr2}}$

$\cong \boldsymbol{\gamma_{cr1} + \gamma_{cr2}}$

$G_c$: Shear stiffness of uncracked concrete       Crack plane 1, 2

$G_{cri} = \dfrac{\tau_{cri}(\varphi_i)}{\gamma_{cri}}$

$\tau_{cr} = \dfrac{\varphi^2}{1 + \varphi^2} m$

$\tau_{cr} = m(\gamma_u/\gamma_{cr})^{c_s}$

$\varphi = \gamma_{cr}/\varepsilon_t$

$0.85\varphi_{max}$     $\varphi_u = \gamma_u/\varepsilon_t$

**Separation of shear strain**

**Both cracks subjected to loading**

$\tau_{cri} = f_{st} \dfrac{\varphi_i^2}{1 + \varphi_i^2}$

$\therefore \dfrac{\gamma_{cr1}}{\varepsilon_{t2}} = \dfrac{\gamma_{cr2}}{\varepsilon_{t1}}$

**One crack subjected to loading, other subjected to unloading**

$\tau_{cr1} = f_{st} \dfrac{\varphi_1^2}{1 + \varphi_1^2}$

$\tau_{cr2} = \dfrac{\tau_{max2}}{0.15\beta_{max2}}(\varphi_{max2} - \varphi_2)$

**Both cracks subjected to unloading**

$\tau_{cri} = \dfrac{\tau_{maxi}}{0.15\beta_{maxi}}(\varphi_{maxi} - \varphi_i)$

**Fig. 5-3    Calculation of shear strain on the quasi-orthogonal crack surface**

## 5.2 Validation of the proposed model by the previous tests of various shear walls

### 5.2.1 Validation case A: Coupling of joints and blocks damage

Ganz and Thurlimann (1984) reported a loading experiment on masonry shear walls. In the W1 specimen as shown in Fig. 5-4 (a), there are openings and slips in the joints. Furthermore, cracks were introduced in the masonry blocks. As two types of nonlinearities are provided, this experiment was considered appropriate for the verification of the extended multi-directional crack model proposed in this chapter. The bricks are arranged in a staggered pattern and this stacking pattern does not provide effective interlock between masonry blocks against horizontal displacement of joints. On the other hand, interlock between blocks that works against the displacement of joints in the vertical direction is exhibited. The method of entering interlocks between blocks into the calculation can also be confirmed by this verification.

The specimen consists of hollow clay bricks stacked in 10 layers. The bricks are bonded to each other with 10 mm of mortar. Each brick measures 300 mm x 190 mm x 150 mm. The finite elements placed in the wall were 300 mm x 200 mm x 150 mm, almost the same dimensions as the brick blocks. Thus, one element may contain at most one joint. As shown in Fig. 5-4 (b), the in-plane structural system was discretized with 3D enhanced strain elements which may describe the induced out-of-plane deformation and the continuous in-plane crack propagation across the element boundaries made by 8 nodes (Simo et al., 1993). An RC constitutive model was applied to the loading beams and specimens (Maekawa et al., 2003). Horizontal displacement was applied to the top plate under a vertical load of 415 kN. The material properties used in the analysis are listed in Table 5-1.

Experimental values were used for the strength of the masonry bricks (Ganz and Thurlimann, 1982). It is known that the strength of the mortar joint in a structure generally differs from the strength of the standardized specimen due to water absorption into the bricks during curing, early age drying, and the quality of construction. In the analysis, sensitivity analysis was performed by setting the tested strength to multiple levels while referring to the specimen strength by the standard testing procedure. Here, the aforementioned concrete-to-sand transition model was applied to the shear transfer characteristics of the cracks in the mortar joint. From sensitivity analysis and in reference to the commonly known internal friction angle of sands, the assumed friction coefficient was set to 0.4 for the case when the solidification caused by cement paste disappears.

**Table 5-1   Material properties for analysis of Ganz wall**

| Material property value | unit | RC element (brick) | RC element (RC beam) |
|---|---|---|---|
| Young's modulus | MPa | 5460 | 22800 |
| Compressive strength | MPa | 7.61 | 29.0 |
| Tensile strength of concrete | MPa | 0.67 | 2.30 |
| Tensile strength of mortar | MPa | 0.01 | - |
| Frictional coefficient | - | 0.40 | - |

(a) Test specimens (W1)    (b) FEM mesh
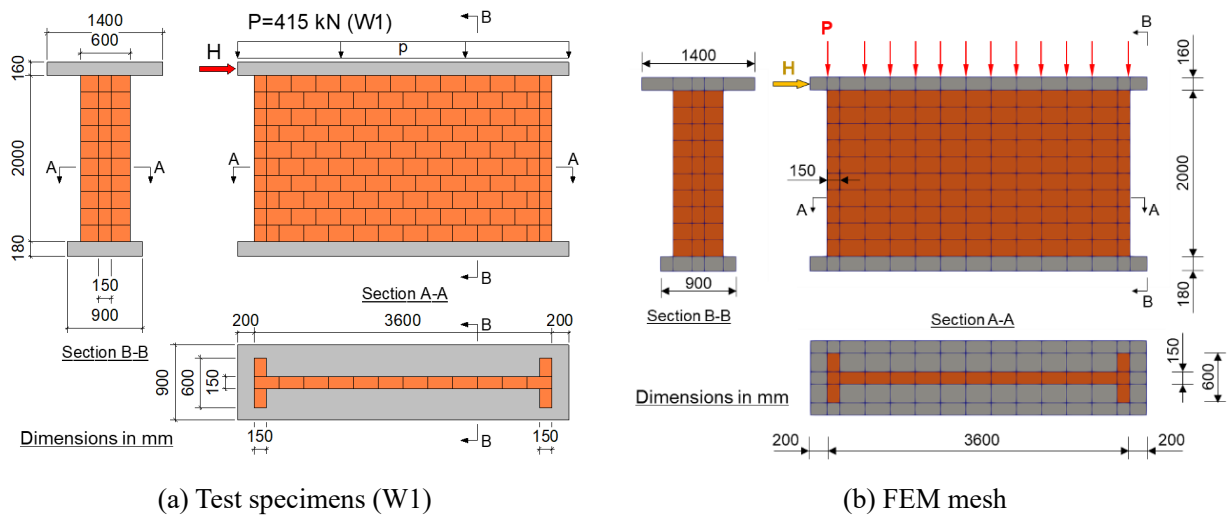
**Fig. 5-4    Experimental setup and finite element discretization of Ganz's wall (Ganz and Thurlimann 1984)**

Fig. 5-5 shows a comparison of the experimental and the analysis results obtained by applying the proposed model. In this analysis, the exact position of the joint is not specified within the finite element, but space averaged continuous strain distribution within the element is addressed. The shear failure path and the load-displacement relations were reasonably well reproduced by the analysis. Both joint openings/slips and damage to the brick were observed in the experiment. It was confirmed that this shear wall experiment is an appropriate target for validating the capabilities of this analysis that can consider both mortar joint and brick cracks.

Furthermore, the author carried out validation through sensitivity analyses by comparing the results when the shear transfer characteristics of the mortar joint would not change ($\alpha = 0.0$) and an extreme case of the mortar joint being disintegrated from the beginning ($\alpha = 1.0$). Fig. 5-6 shows the respective deformation diagrams when each of the models is applied. In the former case, bending damage is predominant in the analysis. This differs from the experimental results in which the shear damage mode is predominant. According to the blue line in Fig. 5-7, the analysis gives a larger load capacity than the experiment. On the other hand, in the latter case, the strain distribution is consistent with the experimental results as shown in Fig. 5-6 (b). However, the load bearing capacity is lower than the experimental value (orange line in Fig. 5-7). In both of these extreme cases, it is difficult to explain the overall structural response. This transition model that combines both characteristics is judged to be effective as a shear transfer model for mortar joint.

Moreover, the sensitivity of the friction angle was investigated. The analysis results when the friction coefficient of the transition model is changed from 0.2 to 0.6 are compared in Fig. 5-8. The higher the coefficient of friction, the higher the shear capacity and stiffness of the wall. When the frictional resistance of the mortar joint is small ($\mu = 0.2$), calculated shear strain distributes horizontally, which indicates that the slip along the horizontal mortar joint is dominant. On the other hand, assuming a higher coefficient of friction ($\mu = 0.6$), the diagonal cracks in the brick appear to be dominant, and the failure mode is determined to be shear compression failure. This is similar to the results of the analysis where shear transfer model on the crack surface of concrete is applied to the mortar joint. This sensitivity analysis shows that the initially assumed coefficient of friction ($\mu = 0.4$) is appropriate.
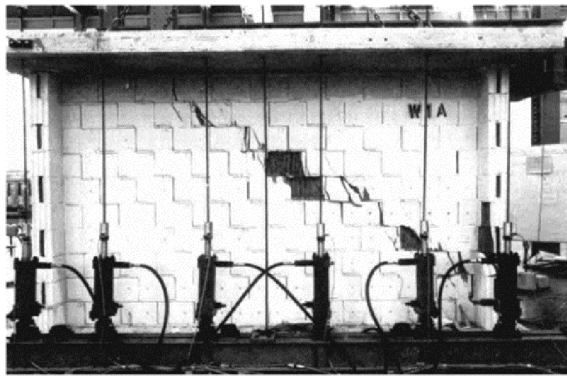
(a) Experimental response at failure



Deformation magnification: 10 times
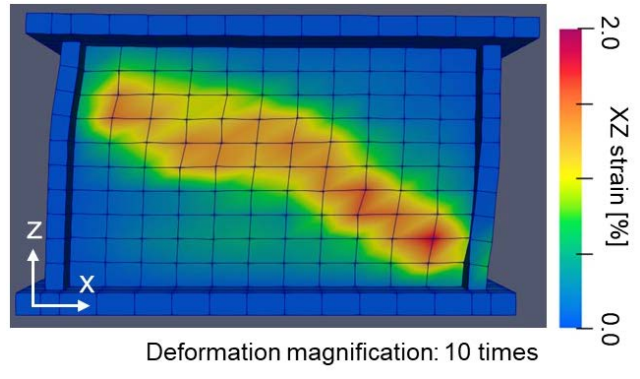
(b) Shear strain distribution of analysis
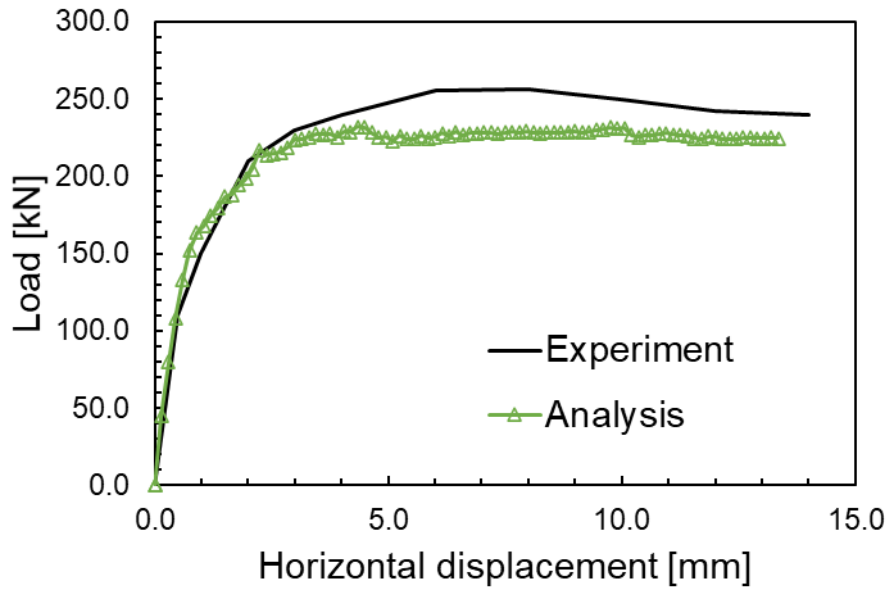


(c) Load-displacement relations

**Fig. 5-5   Behavioral Simulation of masonry wall for experimental validation (Ganz and Thurlimann 1984)**
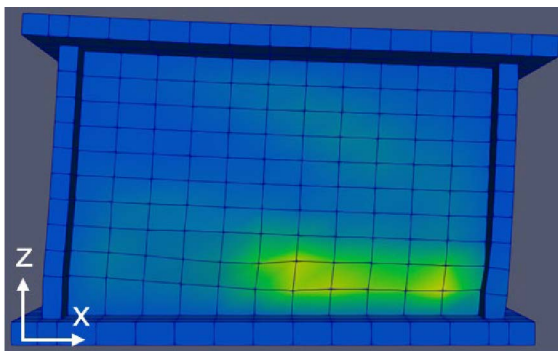


(a) Concrete model
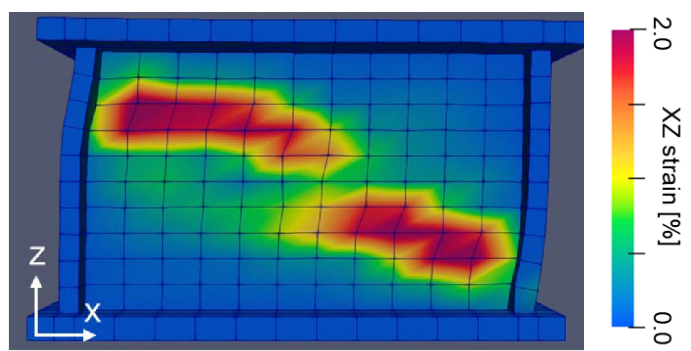


(b) Sand model

**Fig. 5-6   Shear strain distribution and deformational modes in accordance with the mechanism of masonry joints (Deformation magnification of all figures: 10 times)**
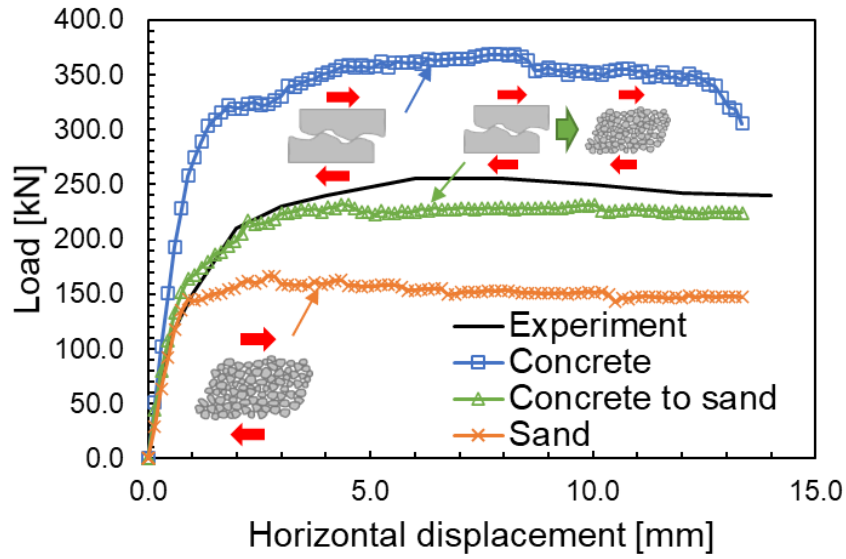
**Fig. 5-7 Comparison of load-displacement relations in view of the kinetics of joints**



(a) Load-displacement relations

(b) Shear strain distribution of analysis ($\mu = 0.2$)

(c) Shear strain distribution of analysis ($\mu = 0.4$)

(d) Shear strain distribution of analysis ($\mu = 0.6$)
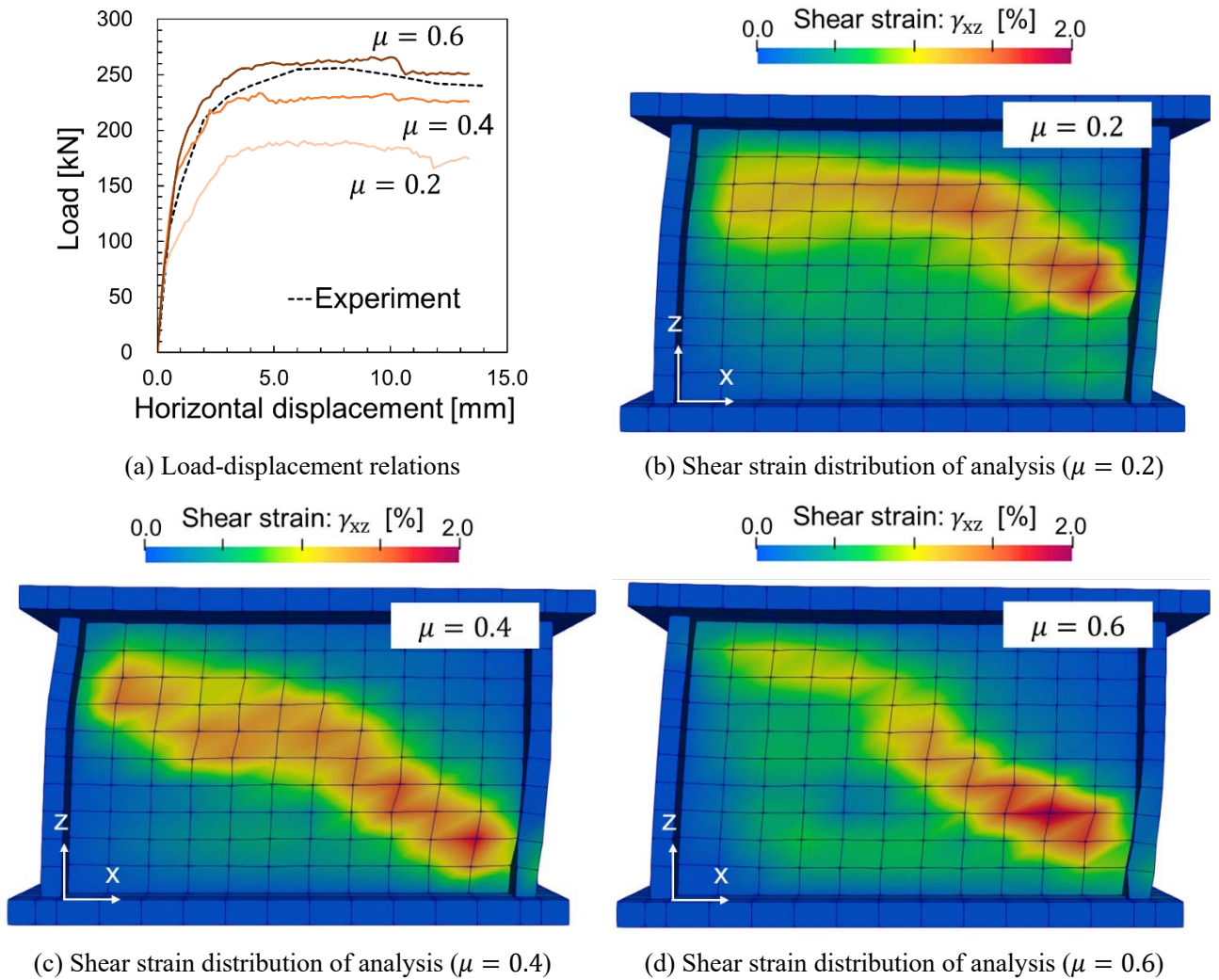
**Fig. 5-8 Sensitivity of the ultimate friction angle in the transition model (Masonry wall).**

70

### 5.2.2 Validation case B: Brick block damage dominates

Bourzam et al. (2008) subjected a brick wall surrounded by RC columns and beams to cyclic loading. Assuming an ordinary window pier, the aspect ratio ($h/l$ in Fig. 5-9 (a)) of the specimen is set to 1.5. The nominal dimensions of the bricks that make up the specimen are 210 x 100 x 60 mm. The bricks are bonded to each other with 10 mm of mortar. The compressive strength of the brick is 30 MPa, whereas the strength of the mortar joint is 27 MPa. Since the strength of the bricks and the mortar joint are nearly the same, there is almost no opening of the joints and the cracks present a failure mode that penetrates the masonry blocks.

The specimens were subjected to cyclic horizontal loading with average vertical stress of 0.4 MPa, assuming a load acting on the first floor of a four-story building. The levelness of the top loading beam is maintained by the loading frame installed on the side of the specimen (Fig. 5-9). The upper and lower loading slabs were sufficiently reinforced and no damage was observed throughout the loading test. The analysis was carried out on the assumption that the loading slabs are elastic bodies.

In the validation of modeling, the measured material properties were set (Table 5-2). However, as mentioned previously, the tensile strength of mortar joint is known to be much lower than its material strength obtained by the standard testing procedure. Then, the strength value obtained from the empirical equation of Nakahama et al. (2009) was used in the analysis.

Fig. 5-10 shows the comparison of the load-displacement relations of experiment and analysis. In the experiment, at the load of about 70 kN in a positive side, the stiffness is greatly reduced. Then, when the horizontal displacement reaches about 2.5 mm, the load comes up to the maximum followed by gradual softening. At the point of maximum horizontal displacement, the specimen retains the strength about half of its capacity. Looking at the hysteresis characteristics, the unloading path is origin-directed up to the maximum load. After the maximum load was reached, the residual displacement was accumulated, and the maximum residual displacement at load removal was about 4 mm. Comparing the loading histories of the negative and positive sides, the load bearing capacity and residual strength of the negative side are a little larger, while its residual displacement is smaller.

The initial stiffness and residual strength can be reproduced by the analysis. On the other hand, the maximum strength was underestimated, and residual displacement was evaluated on the higher side. Adjusting the strength and coefficient of friction of the mortar joint may improve these discrepancies. In the analysis, the difference between the positive and negative loading histories is small. The transition model applied to the mortar joint is an elasto-perfect plastic model, and the Bauschinger effect is not considered. It was confirmed that there is room for improvement in historical characteristics. In Fig. 5-11, the ultimate state of the specimen is compared with the analysis value of the corresponding shear strain distribution. In Fig. 5-10, red circle indicates the point where the deformation is captured. The diagonal cracks in the center of the specimen and the dominant damage at the base are well reproduced.

Owing to the relative strength of the mortar joint, many cracks were observed to penetrate the bricks in the experiment. The proposed model is capable of evaluating the load bearing capacity on the safe side, and the damage mode is confirmed correctly.

**Table 5-2    Material properties for CaseB**

| Material property value | unit | RC element (brick) | RC element (RC pillar) | Elastic element |
|---|---|---|---|---|
| Young's modulus | MPa | 8240 | 18300 | 210000 |
| Compressive strength | MPa | 30.0 | 20.0 | - |
| Tensile strength of concrete | MPa | 2.20 | 1.70 | - |
| Tensile strength of mortar | MPa | 0.27 | - | - |
| Frictional coefficient | - | 0.50 | - | - |
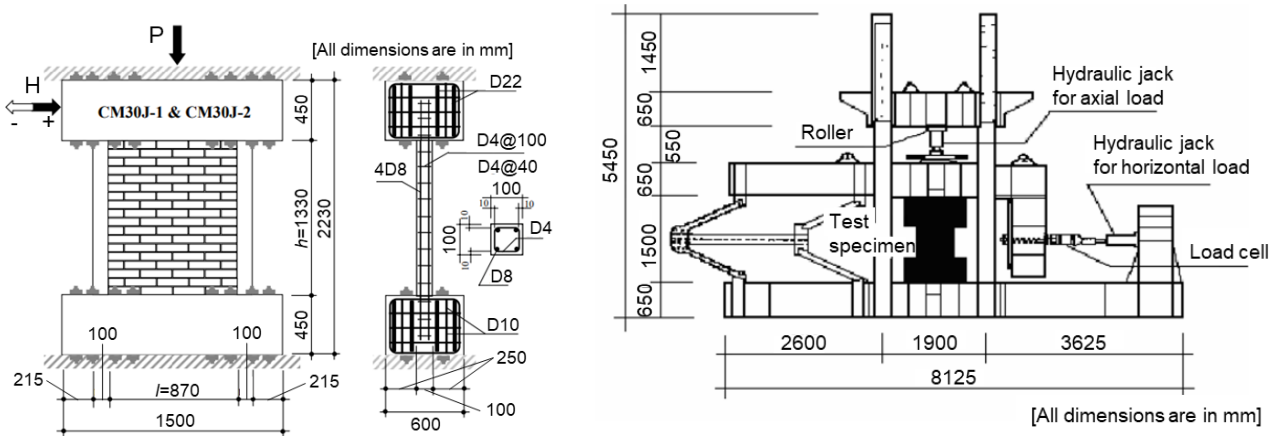


(a-1) Test specimens                    (a-2) Loading system
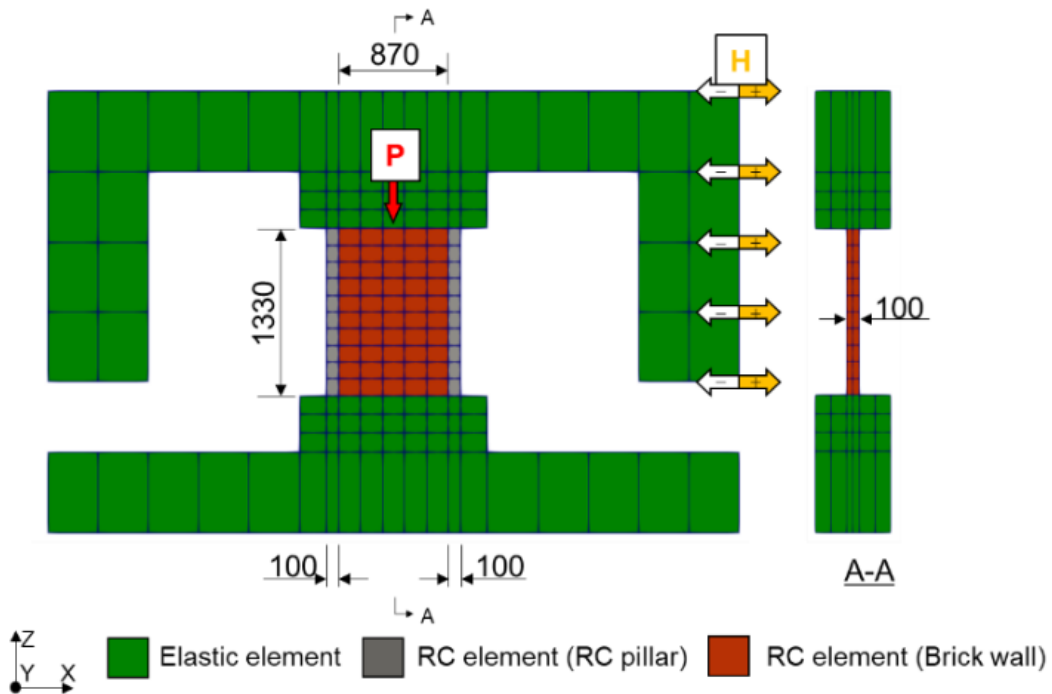


(b) FEM mesh

**Fig. 5-9    Case B (Strong mortar joint): Experimental setup and FE mesh discretization (Bourzam *et al*. 2008)**

72
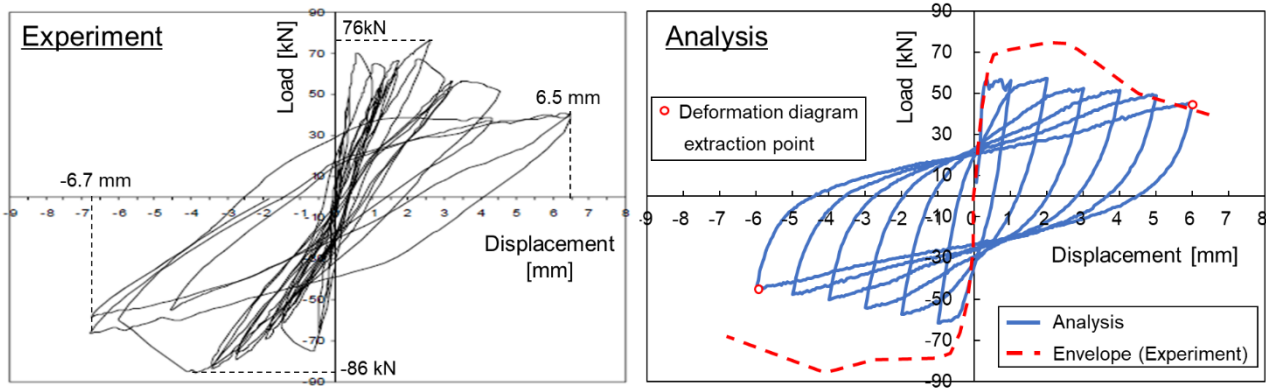
**Fig. 5-10   Case B (Strong mortar joint): Computed load-displacement relations (Bourzam *et al*. 2008)**
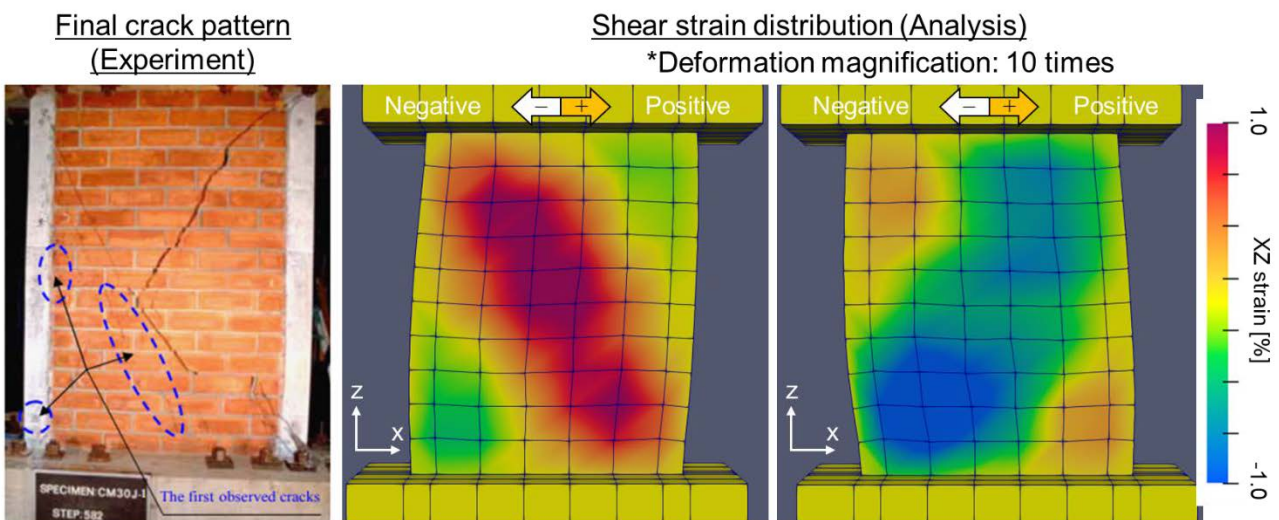


**Fig. 5-11   Case B (Strong mortar joint): Failure mode and shear strain distribution (Bourzam *et al*. 2008)**

### 5.2.3   Validation case C: Mortar joint damage dominates

In masonry structures constructed in the early 20th century, the strength of the mortar joint was considerably lower than that of the brick. The experiments of Abrams and Shah (1992) were selected for validation as satisfying this condition. As shown in Fig. 5-12 (a), the specimens were nearly unrestrained brick walls. Three types of specimens with different aspect ratios were prepared (W1, W2 and W3). The nominal dimensions of the bricks used were 198 x 89 x 56 mm and the mortar joints were 9.5 mm thick. Table 5-3 lists the physical property input in the analysis. The strength of the bricks in the experiment was 24.0 MPa, and the compressive strength of the mortar was 6.3 MPa. The friction coefficient of mortar joint is reported to be 0.50. The tensile strength of the mortar joint in the structure was set to 1/100 of the standard specimen strength.

A constant vertical load was applied to each specimen by applying the tension force of the PC steel bar to the top loading beam, and horizontal displacement was applied to the center of the top beam as shown in Fig. 5-12 (b).

Fig. 5-13 and Fig. 5-14 show comparisons between the experiment and the analysis. Due to the low strength of the mortar joint, the diagonal cracks propagated along the joints while avoiding the masonry blocks. In the analysis too, the diagonal cracks did not propagate linearly, and the main strain was distributed stepwise along the joints. Diagonal

cracks were found in experiments on W1 and W2 with a large aspect ratio (Fig. 5-14), but in W3 with a small aspect ratio, cracks were concentrated along the joints at the base.

Although the load bearing capacity and residual strength were a little smaller than the experimental fact, the cyclic hysteresis indicated by the S-shaped load displacement diagram is reproduced. This nonlinear but quasi-elastic mode of displacement attributes to the kinetics of rigid body rotation of the entire masonry wall.

Table 5-3   Material properties for Case C

| Material property value | unit | RC element (brick) | Elastic element |
|---|---|---|---|
| Young's modulus | MPa | 4710 | 210000 |
| Compressive strength | MPa | 24.0 | - |
| Tensile strength of concrete | MPa | 1.91 | - |
| Tensile strength of mortar | MPa | 0.06 | - |
| Frictional coefficient | - | 0.50 | - |
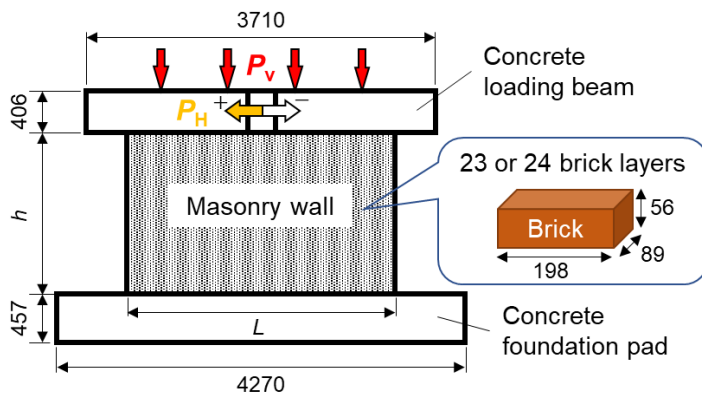


Scale of each specimen

| Specimen | $L$ [mm] | $h$ [mm] | $L/h$ | $P_v^{*1}$ [MPa] |
|---|---|---|---|---|
| W1 | 3658 | 1626 | 2.25 | 0.52 |
| W2 | 2743 | 1626 | 1.67 | 0.34 |
| W3 | 1829 | 1626 | 1.12 | 0.34 |

*1: Vertical stress

(a) Test specimens (Dimensions in mm)



(b) FEM mesh (Dimensions in mm)

**Fig. 5-12   Case C (Weak mortar joint): Experimental setup and FE mesh discretization (Abrams and Shah 1992)**

(a) W1



(b) W2



(c) W3

**Fig. 5-13    Case C (Weak mortar joint): Computed load-displacement relations (Abrams and Shah 1992)**

(a) W1                    (b) W2                    (c) W3

**Fig. 5-14　Case C (Weak mortar joint): Failure mode and shear strain distribution (Abrams and Shah 1992)**

## 5.3　Summary of Chapter 5

Table 5-4 gives a summary of the recorded experimental and analytical load bearing capacity values. In each case, the proposed model estimates the load bearing capacity on the safe side. Focusing on the historical characteristics, the energy absorption capacity in the analysis is also calculated somewhat on the small side. Therefore, from the viewpoint of practical design, the analysis for both monotonic and cyclic loading gives a conservative evaluation.

The constitutive law based on the existing non-orthogonal multi-directional crack model can take into account the nonlinearity presented by a group of cracks intersecting in up to six directions in a finite region. In this chapter, a nonlinear response analysis is presented in which a fixed crack plane with three directions is placed in the nonlinear response of joints of a masonry structure, and the remaining three directions are assigned to represent the damage to unreinforced masonry blocks. Furthermore, a transition model that takes into account the degradation of mortar solids due to shear deformation was applied to a low-strength mortar joint. Three cases were selected to validate the analysis model: a masonry wall structure with cracks in both the joints and the blocks, a structure where the cracks exclusively penetrate the blocks, and a structure where the crack damage is concentrated in the joints. The findings of this study are summarized as below.

i. The proposed model is capable of reproducing the damage mode of a masonry structure subjected to shear and evaluating the load bearing capacity conservatively.

ii. Structural analysis also confirmed that the shear transfer characteristics of low-strength mortar joint combine the shear transfer characteristics of concrete and those of sand.

iii. To improve the accuracy of the analysis, it is necessary to take into account the characteristic of loss of consolidation of sand particles in mortar joint due to shear slip.

**Table 5-4  Summary of experimental validation results of capacity**

| \Case | Case A (Ganz) | Case B (Strong mortar joints) | | Case C (Weak mortar joints) | | | | | |
|---|---|---|---|---|---|---|---|---|---|
| | | | | W1 | | W2 | | W3 | |
| | | P | N | P | N | P | N | P | N |
| $P_E$ | 256 | 76 | -86 | 409 | -436 | 191 | -200 | 89 | -89 |
| $P_A$ | 232 | 57 | -62 | 348 | -355 | 143 | -150 | 64 | -64 |
| $P_A/P_E$ | 0.9 | 0.8 | 0.7 | 0.9 | 0.8 | 0.7 | 0.7 | 0.7 | 0.7 |
| $G_E$ | - | 476 | | 5,930 | | 2,790 | | 1.085 | |
| $G_A$ | - | 459 | | 4,400 | | 1,790 | | 599 | |
| $G_A/G_E$ | - | 1.0 | | 0.7 | | 0.6 | | 0.6 | |

$P_E$, $P_A$: Maximum load in experiment and analysis [kN]

$G_E$, $G_A$: Energy absorbed in the final loop in experiment and analysis [J]

P, N: "Positive" and "Negative"

References of Chapter 5

Abrams, D.P., Shah, N., 1992. Cyclic load testing of unreinforced masonry walls. University of Illinois, at Urbana-Champaign, Newmark Civil Engineering Laboratory, Advanced Construction Technology Center.

Bourzam, A., Goto, T., Miyajima, M., 2008. Shear capacity prediction of confined masonry walls subjected to cyclic lateral loading. *Doboku Gakkai Ronbunshuu A 64*, 692–704. https://doi.org/10.2208/jsceja.64.692

Bruneau, M., 1995. Damage to masonry buildings from the 1995 Hanshin-Awaji (Kobe, Japan) earthquake -Preliminary report-, in: *Seventh Canadian Masonry Symposium*. Canada Masonry Design Centre, Ontario, pp. 84–98.

Coburn, A., Spence, R., 2002. *Earthquake Protection*, 2nd ed. John Wiley & Sons, West Sussex, England.

Facconi, L., Plizzari, G., Vecchio, F.J., 2014. Disturbed stress field model for unreinforced masonry. *Journal of Structural Engineering 140*, 04013085. https://doi.org/10.1061/(ASCE)ST.1943-541X.0000906

Fukuura, N., Maekawa, K., 1998. Multi-directional crack model for in-plane reinforced concrete under reversed cyclic actions-4 way fixed crack formulation and verification. *Computational modelling of concrete structures*, 143–152.

Ganz, H.R., Thurlimann, B., 1984. Versuche an mauerwerksscheiben unter normalkraft und querkraft. Zurich, Switzerland. https://doi.org/https://doi.org/10.3929/ethz-a-000328538

Ganz, H.R., Thurlimann, B., 1982. Tests on the biaxial strength of masonry. Zurich, Switzerland. https://doi.org/https://doi.org/10.3929/ethz-a-000248407

Hashimoto, R., Kikumoto, M., Koyama, T., Mimrua, M., 2017. Method of deformation analysis for composite structures of soils and masonry stones. *Computers and Geotechnics 82*, 67–84. https://doi.org/10.1016/j.compgeo.2016.09.011

Hashimoto, R., Koyama, T., Kikumoto, M., Saito, T., Mimura, M., 2014. Stability analysis of masonry structure in Angkor Ruin considering the construction quality of the foundation. *Journal of Civil Engineering Research 2014* 4, 78–82.

Hauke, B., Maekawa, K., 1999. Three-dimensional modelling of reinforced concrete with multi-directional cracking. *Doboku Gakkai Ronbunshu 1999*, 349–368. https://doi.org/10.2208/jscej.1999.634_349

Hisada, Y., Shibaya, A., Ghayamghamian, M.R., 2004. Building damage and seismic intensity in Bam city from the 2003 Iran. *Bulletin of the Earthquake Research Institute*, University of Tokyo 79, 81–93.

Javed, M., Khan, A.P., Magenes, G., 2006. Behaviour of masonry structures during the Kashmir 2005 earthquake, in: *First European Conference on Earthquake Engineering and Seismology*. Geneva, Switzerland, pp. 1–10.

Li, B., Maekawa, K., Okamura, H., 1989. Contact density model for stress transfer across cracks in concrete. *Journal of Faculty of Engineering*, The University of Tokyo 40, 9–52.

Lourenço, P.B., Milani, G., Tralli, A., Zucchini, A., 2007. Analysis of masonry structures: review of and recent trends in homogenization techniques. *Canadian Journal of Civil Engineering 34*, 1443–1457. https://doi.org/10.1139/L07-097

Lourenço, P.B., Rots, J.G., 1997. Multisurface interface model for analysis of masonry structures. *Journal of Engineering Mechanics 123*, 660–668. https://doi.org/10.1061/(ASCE)0733-9399(1997)123:7(660)

Maekawa, K., Fukuura, N., 2013. Nonlinear modeling of 3D structural reinforced concrete and seismic performance assessment, in: *Infrastructure Systems for Nuclear Energy*. John Wiley & Sons, Ltd, Chichester, UK, pp. 153–184. https://doi.org/10.1002/9781118536254.ch11

Maekawa, K., Pimanmas, A., Okamura, H., 2003. *Nonlinear Mechanics of Reinforced Concrete*. CRC Press Taylor and Francis Group, London.

Maier, G., Papa, E., Nappi, A., 1991. On damage and failure of brick masonry, in: *Proceedings of the Experimental and Numerical Methods in Earthquake Engineering*. Kluwer Academic Publishers, Netherlands, pp. 223–245.

Mukai, Y., Yamamoto, N., Masui, M., Miyauchi, A., 2016. Field survey for the damage distribution of traditional masonry buildings in Bhaktapur caused by the 2015 Gorkha earthquake in Nepal. Hyogo, Japan.

Nakahama, T., Hatanaka, S., Mishima, N., 2009. Experimental study on shearing test method and constitutive law of brick joint. *Journal of Structural and Construction Engineering* (Transactions of AIJ) 74, 1225–1232. https://doi.org/10.3130/aijs.74.1225

Okamura, H., Maekawa, K., 1991. *Nonlinear Analysis and Constitutive Models of Reinforced Concrete*. Gihodo-Shuppan Co, Japan.

Pandey, B.H., Meguro, K., 2004. Simulation of brick masonry wall behavior under in-plane lateral loading using applied element method, in: *13th World Conference on Earthquake Engineering*. Vancouver, B.C., Canada.

Simo, J.C., Armero, F., Taylor, R.L., 1993. Improved versions of assumed enhanced strain tri-linear elements for 3-D finite deformation problems. *Computer Methods in Applied Mechanics and Engineering 110*, 359–386. https://doi.org/10.1016/0045-7825(93)90215-J

Yamanoi, Y., Maekawa, K., 2020. Shear bifurcation and graveling of low-strength concrete. *Journal of Advanced Concrete Technology 18*, 767–777. https://doi.org/10.3151/JACT.18.767

# 6 Application to Damage Evaluation of Underground RC Structures Using a Full-Scale Model

## 6.1 Proposal of fault displacement countermeasures using artificial soft rock

*Damage caused by the fault displacement*

It is well known that underground structures have a superior seismic resistance to the one of ground structures because the response of the ground is dominant. On the other hand, damage to underground structures has also been reported during major earthquakes. Recently, Tsinidis et al., (2020) and Wang et al., (2021) have compiled a wide range of past damage cases, experiments, and analysis cases for tunnels. Damage to underground structures is roughly divided into damage caused by vibration and damage caused by permanent displacement of the ground. The fault displacement targeted in this study corresponds to the latter, which has the characteristic that the frequency of occurrence is low, but the damage is enormous.

Damage caused by fault displacement has been reported in various civil engineering structures such as dams (Nakamura, 1990; Ohmachi, 2000), bridges(Kawashima, 2002; Pamuk et al., 2005) and sewers (Hatakeyama et al., 2020). Damages of tunnels around the world have been summarized by Sabagh & Ghalandarzadeh, (2020). In particular, the three earthquakes that occurred in 1999-the Kocaeli earthquake, the Duzce earthquake in Turkey and the Chi-Chi earthquake in Taiwan caused enormous damage to structure due to fault displacement (Anastasopoulos and Gazetas, 2007; Kontogianni and Stiros, 2003; Wang et al., 2001). These experiences had led to increase studies on fault displacement. In recent years, fault displacement damage to structures has also been reported in the 2004 Mid Niigata Chuetsu Earthquake (Konagai et al., 2005) and the 2008 Wenchuan Earthquake (Lin et al., 2009).

*Current status of fault displacement measures*

The basic measure against fault displacement is to "avoid sites where active faults exist" regardless of the structure. Shiozaki et al., (2018) summarized how the response policies of active faults and fault displacements are stipulated in the guidelines or standards for civil engineering structures in Japan. According to them, in linear structures such as railways, sewers, and oil pipelines, it may be unavoidable to intersect with faults, so the specific countermeasure policies are shown in the standards. On the other hand, in dams and nuclear facilities, strict measures have been taken so that structures cannot be installed on faults where displacement may occur even by 1 mm.

However, it is difficult to judge what is regarded as an active fault even if it is simply said to "avoid active faults". As evidence, the criteria for accreditation of "active faults to be considered in seismic design", which are subject to examination at nuclear power plants, have been changed twice from 1978 to 2013 (Shiozaki et al., 2018). In addition, the reverse fault, which is predominantly seen in the subduction zone as in Japan, has a complicated spatial structure, and it is difficult to evaluate the detailed position and activity. Therefore, it is important to ensure the safety of the structure when the fault is displaced, not just whether the fault is active. From this viewpoint, a number of research committees have been set up, centered on electric power-related company and academia, and studies have been carried out (Japan Nuclear Safety Institute, 2013; Narabayashi and Kamiya, 2017; The Nuclear Civil Engineering Committee of the JSCE, 2015).

In April 2019, the IAEA upgraded the verification of fault displacement from "Guide" to "Requirement" (International Atomic Energy Agency, 2019). Probabilistic risk assessment (PRA) is attracting attention as an effective means for fault displacement, which is an unexpected event (Narabayashi and Kamiya, 2017). Although many studies have

been made on fault displacement hazard evaluation (Petersen et al., 2011; Takao et al., 2018; Youngs et al., 2003), studies on structural fragility evaluation for fault displacement have been limited (for example, (Haraguchi et al., 2020; Zheng et al., 2021)). On the other hand, the application of the deterministic performance assessment method used in the evaluation of seismic resistance has also been studied, and a systematized one based on the results of experiments and analyzes has been proposed (Itoh et al., 2020).

*Fault displacement countermeasures using weak layers*

At the Kashiwazaki-Kariwa nuclear power plant, artificial bedrock (roughly 5 MPa of compressive strength) with rigidity and strength designed to be less than that of the concrete foundation was used as a soil improvement additive (Kurihara et al., 1994). When fault displacement reaches the power plant, the artificial soft rock is expected to undergo shear failure before the foundation, thereby mitigating damage to the nuclear power facilities as shown in Fig. 3-1. The same concept was the basis for constructing a soil bentonite wall, which has been confirmed in both experiments and analysis to have the effect of limiting damage (Fadaee et al., 2013). In the purpose of confirming the bifurcation and dispersion of the shear band by the weak layer, the model experiment was conducted in **Chapter 3**. In this chapter, the effect of man-made rock (MMR) on reducing damage to underground structures is verified using a full-scale model. Here, the transition model which was validated for low-strength cementitious materials is used for the MMR.

6.2     Validation of the constitutive model for the ground with shear band

(1)  Constitutive model for geomaterials

    For geomaterials, an elasto-plastic constitutive law based on the multi-yield surface plastic theory has been proposed (Gutierrez et al., 1993; Towhata, 2008; Towhata and Ishihara, 1985). Soltani & Maekawa, (2015) incorporated this model into the mean stress-mean strain relationship for application to coupled analysis with concrete. In the multi-yield surface plasticity theory, geomaterials are regarded as a set of springs with sliders, as shown in Fig. 6-1. The spring represents elasticity of the ground, and the slider represents plasticity. By setting different rigidity and strength for each spring, the material non-linearity can be expressed. Specifically, some reference points are extracted for the shear stress-strain relationship of a certain ground. By defining the average stiffness and yield strength between each reference point as in Eq. (6-1) and (6-2), higher-order nonlinearity can be decomposed into any number of elasto-perfect plasticity. For each spring component, the deviatoric stress are calculated based on the flow rule, consistency condition, and Drucker-Prager yield surface. By summation of the stresses of all shear springs, the deviatoric component of the ground element is calculated as Eq. (6-3). On the other hand, the volumetric component is represented by one spring considering elasto-plasticity (Eq. (6-4)). The volumetric plasticity is divided into two parts, dilatancy provoked by shear ($\varepsilon_\mathrm{v}$) and consolidation evolved by the changes of effective stress ($\varepsilon_\mathrm{p}$). Finally, the total stress tensor of the element is calculated by the combination of the deviatoric and volumetric component (Eq. (6-5)).

$$\begin{cases} G_0^\mathrm{m} = D^\mathrm{m} - D^{\mathrm{m}+1}, & \mathrm{m} = 1 \sim \mathrm{n} - 1 \\ \quad G_0^\mathrm{n} = D^\mathrm{m}, & \mathrm{m} = \mathrm{n} \end{cases} \qquad (6-1)$$

$$\begin{cases} F^\mathrm{m} = G_0^m \gamma_m, & m = 1 \sim \mathrm{n} - 1 \\ \quad F^\mathrm{n} = \infty, & \mathrm{m} = \mathrm{n} \end{cases} \qquad (6-2)$$

$$s_{ij} = \sum_{m=1}^{n} s_{ij}^m\left(\varepsilon_{kl}, \varepsilon_{pkl}^m, G_0^m, F^m\right) \tag{6-3}$$

$$p = 3K_v\left(\varepsilon_m - \varepsilon_v - \varepsilon_p\right) \tag{6-4}$$

$$\sigma_{ij} = s_{ij} + p\delta_{ij} \tag{6-5}$$

where, $\varepsilon_m$ is the mean strain and equal to $\varepsilon_{ii}/3$; $\delta_{ij}$ is the Kronecker's delta; $K_v$ is the volumetric stiffness and expressed by the following equation considering the confinement dependency with the confinement index $\chi$.

$$K_v = K_0\chi^{0.5}, \qquad K_0 = \frac{2(1+v)}{3(1-2v)}G_0, \qquad \chi = \frac{A + BI_1}{S_u(p_0)} \tag{6-6}$$

In the original model, the dilatancy denoted by $\varepsilon_v$ is divided into two components as shown in Eq. (6-7). One is the unrecoverable negative dilatancy denoted by $\varepsilon_{vc}$ and the other is recoverable positive dilatancy denoted by $\varepsilon_{vd}$. Each component is expressed by the following empirical formula.

$$\varepsilon_v = \varepsilon_{vc} + \varepsilon_{vd} \tag{6-7}$$

$$\varepsilon_{vc} = \varepsilon_{v,lim}\left\{1 - \exp\left[-3\left(J_{2ps} + J_{2p,ini}\right)\right]\right\} - \varepsilon_{vc,ini} \tag{6-8}$$

$$J_{2ps} = \int dJ_{2ps}, \qquad dJ_{2ps} \equiv \frac{1}{2}\beta\frac{s_{kl}}{J_2} \cdot d\varepsilon_{kl}, \qquad \beta = \sqrt{\frac{J_2}{|p|}}, \qquad J_2 = \sqrt{\frac{1}{2}s_{ij}s_{ij}}$$

$$\varepsilon_{vd} = \eta\left[J_{2s} - \frac{1 - \exp(-aJ_{2s})}{a}\right], \qquad \eta = \frac{1}{2}\left(\frac{\varepsilon_{vc} + \varepsilon_{v,ini}}{\varepsilon_{v,lim}}\right), \qquad J_{2s} = \sqrt{\frac{1}{2}e_{ij}e_{ij}} \tag{6-9}$$

where $s_{ij}$ and $e_{ij}$ are the deviatoric tensor of stress and strain; suffix "ini" means the initial state of sandy foundation which is specified by defining the initial relative density; $\varepsilon_{v,lim}$ is the intrinsic volumetric consolidating strain; $a$ is the material constant.

When fault displacement acts, loose soil will undergo gradual deformation due to negative dilatancy. On the other hand, localized shear bands will be formed in dense soil. It is well known that the path of the shear band due to fault displacement depends on the dilation angle of the soil (Cole and Lade, 1984). In the dense case, the shear strain-volumetric strain relationship is highly dependent on the ratio of shear band width to mesh size. Anastasopoulos et al., (2007) have defined four phases for response of sand subject to direct shear, quasi-elastic behavior, plastic behavior, softening behavior and residual behavior, and proposed the elasto-plastic constitutive model with isotropic softening by considering mobilized friction angle and mobilized dilation angle according to the phase. After formation of shear band, it is assumed that all plastic shear deformation takes place within the shear band. They considered the mesh size dependency in this phase by associating the strain of the element with the one in the shear band when setting the plastic shear strain at which softening has been completed. Following this idea, the original dilatancy model is modified as shown in Fig. 6-2 and Eq. (6-10).

$$\begin{cases} \varepsilon_{vd} = \varepsilon_{vdp}(J_{2s}) & \cdots J_{2s} \leq J_{2sp} \\ \varepsilon_{vd} = \varepsilon_{vdp}(J_{2sp}) + \varepsilon_{vdf}(J_{2s}) & \cdots J_{2s} > J_{2sp} \end{cases} \tag{6-10}$$

The volumetric plastic strain $\varepsilon_{vd}$ derived from positive dilatancy is divided into two parts, before and after the shear band begins to form. The boundary is identified by the second invariant of the total deviatoric strain at the peak

denoted by $J_{2sp}$. In the former, the dilation strain denoted by $\varepsilon_{vdp}$ represents a uniform volumetric deformation of the entire reference volume and is indicated in Eq. (6-9). In the latter, $\varepsilon_{vdp}$ represents the volumetric deformation of the shear band where no deformation of the soil outside the shear band is assumed.

the continuum deformation has reached a plateau and the empirical formula expressed by Eq. (6-11) is newly applied to the original model.

$$\varepsilon_{vdf} = \varepsilon_{vdf,lim}\left[1 - \left(1 - \frac{J_{2s} - J_{2sp}}{J_{2sf} - J_{2sp}}\right)^2\right], \qquad 0 \le \varepsilon_{vdf} \le \varepsilon_{vdf,lim} \qquad (6-11)$$

$$\varepsilon_{vdf,lim} = \left[\varepsilon_{vdf,lim}^{ref} - \varepsilon_{vdp}(J_{2sp})\right]\cdot\lambda > 0, \qquad \lambda = \frac{L_{sb}}{L_e}$$

$$J_{2sf} = J_{2sp} + (J_{2sf}^{ref} - J_{2sp}^{ref})\cdot\lambda$$

where, $\varepsilon_{vdf,lim}$ is the maximum dilation strain in the shear band; $J_{2sf}$ is the second invariant of the total deviatoric strain where the dilatancy becomes steady; $L_{sb}$ and $L_e$ are the width of the shear band and the reference length of the element. The superscript of "ref" means the value in the relation of the reference shear stress-shear strain. The mesh dependency is considered in two factors, only after the peak. One is the maximum dilation strain, and the other is the shear strain up to steady state. For the same test piece, these parameters must have the unique value in the displacement field so the ratio of the shear band width to the reference length of the element is multiplied. The larger the element to the shear band, the smaller the amount of dilation strain and the larger the dilation angle.
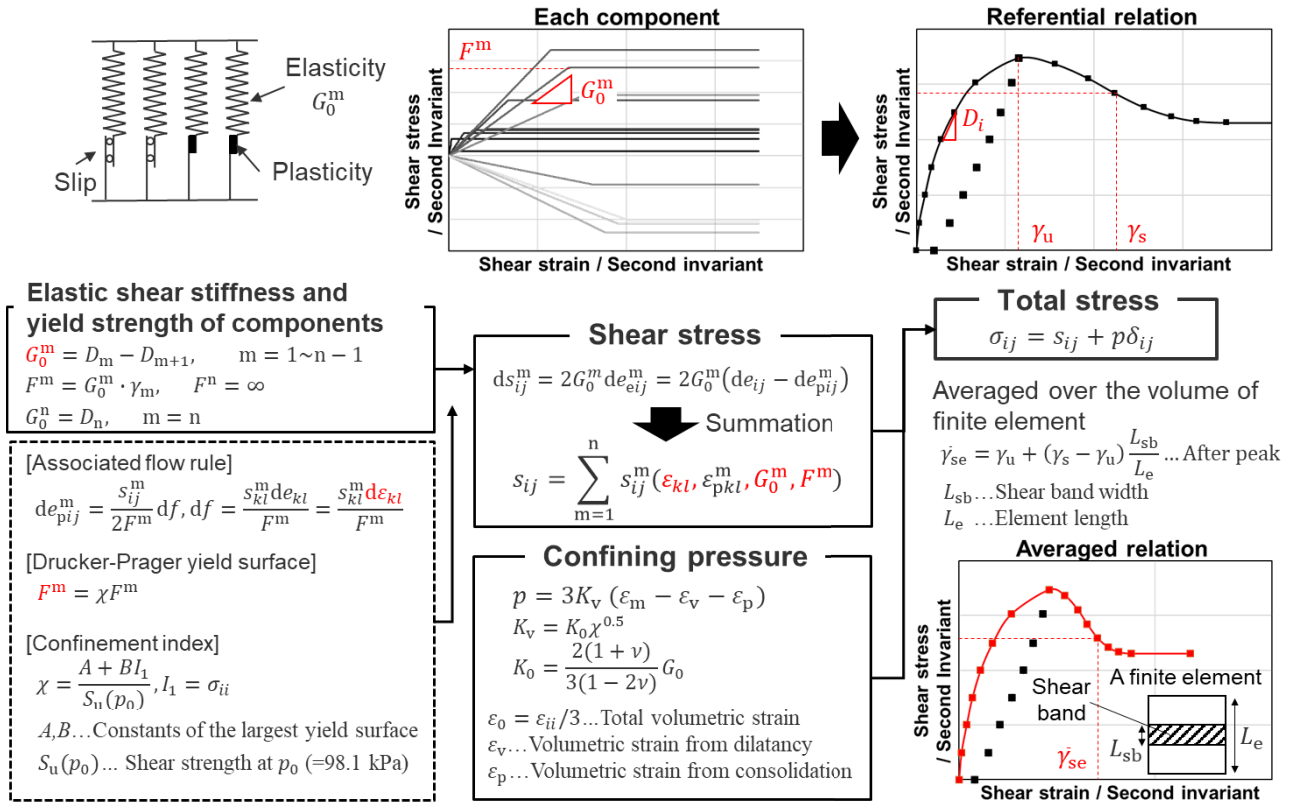


**Fig. 6-1   Constitutive model based on the multi-yield surface plasticity**
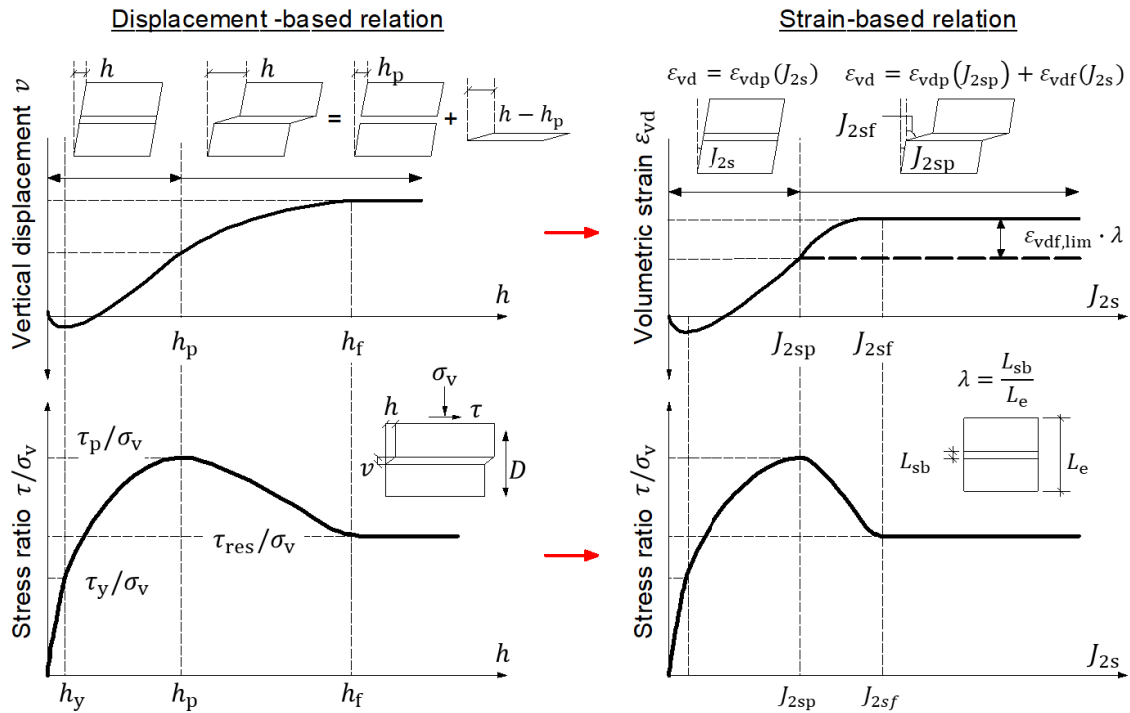
**Fig. 6-2    Concept of modified dilatancy model**

As presented in Fig. 6-3, the validation of the proposed model is checked by the direct shear test of Toyoura sand (Shibuya et al., 1992).    The test sand had a median diameter of 0.16 mm and was compacted under dry conditions to a relative density of 89 %. From the result of the parameter adjustment, the material constants $a$ was set to 75. The reference shear stress-strain relationship and dilatancy parameters ($\varepsilon_{vdf,\lim}^{ref}$, $J_{2sf}^{ref}$ and $J_{2sp}^{ref}$) were set to the values obtained in the experiment. The shear band width ($L_{sb}$) was set to 2.6 mm based on the experimental fact that it is 10-15 times mean particle diameter (Alshibli and Sture, 1999; Soltani and Maekawa, 2015).

The result of the analysis using one hexahedron element with 8 nodes successfully reproduces the experimental result as shown in Fig. 6-4 (a). Using the original model without modifying the dilatancy model causes the dilation strain to increase to infinity as the shear strain increases, resulting in an overestimation of the volumetric strain (Fig. 6-4 (b)).



(a)   Direct shear test equipment                                        (b)   One element model
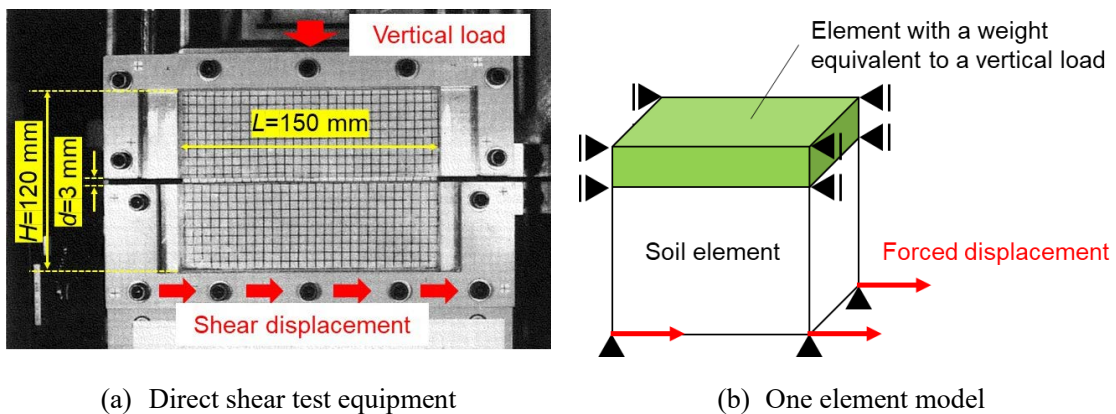
**Fig. 6-3    Overview of the experiment and simulation to identify dilatancy properties** (Shibuya et al., 1992).

83

(a) Modified dilatancy model       (b) Original model
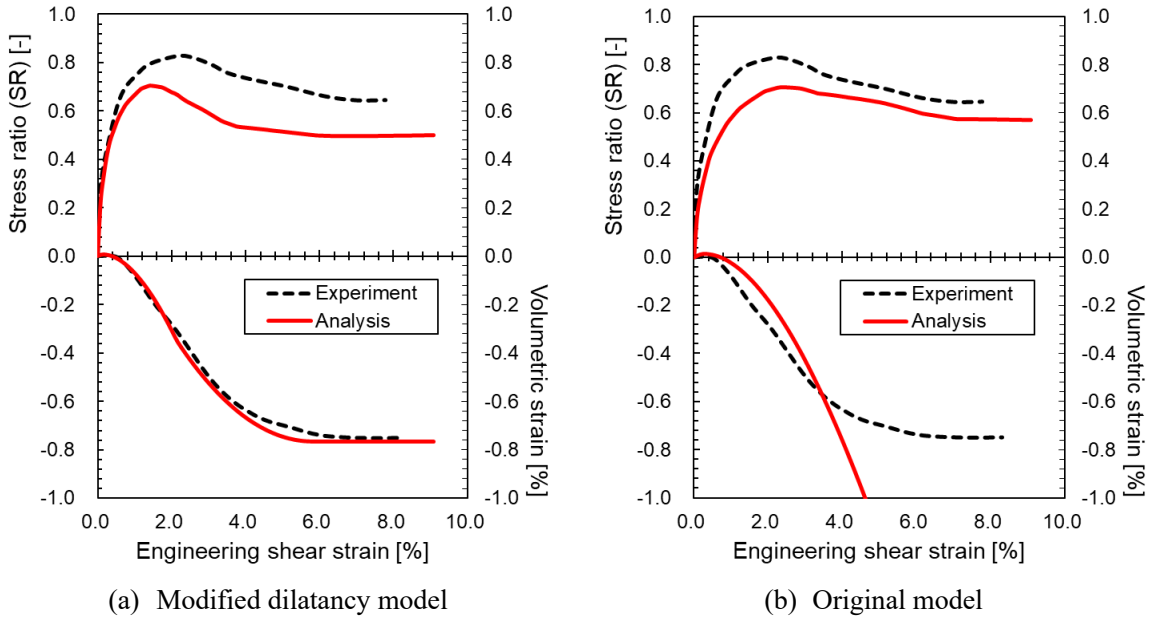
**Fig. 6-4　Adjustment result with experimental value by Shibuya et al. (1992)**

(2) Comparison with the centrifuge model test

Higuchi et al., (2017). conducted a centrifugal model experiment in which a reverse fault displacement with an inclination of 30 degrees is applied to a box culvert buried in sand under a gravitational field of 50 G. In order to confirm the validity of the soil constitutive model, an experimental case with only sand was selected as a comparison target. As presented in Fig. 6-5, the test specimen including the steel frame was modeled by 8-node hexahedron elements, and the interface between both was modeled by the joint interface elements. The above-mentioned constitutive model was applied to the sand layer, while elastic model was applied to the steel frame. The input physical properties of sand were set as shown in Table 6-1 based on the results of the triaxial compression test. The total stress model proposed by Ohsaki, (1980) was adopted to determine the reference shear stress-strain relationship, and the initial shear modulus according to the porosity was determined by the following equation proposed by Tatsuoka et al. (1993).

$$G_0 = 90 \frac{(2.17 - e)^2}{1 + e} \sigma'^{0.4}_3 \qquad (6 - 12)$$

where, $G_0$ is the initial shear modulus; $e$ is the void ratio; $\sigma'_3$ is the minor principal stress and the value when $\sigma'_3$ was equal to 0.1 MPa was used as the reference value. The No. 7 silica sand was used in the experiment. The dilatancy parameters were determined so that the results of simulation using the one second-order element fit the triaxial compression test results as shown in Fig. 6-6. The proposed model can accurately reproduce the volumetric strain. The inconsistency in shear load capacity is due to fracture criteria. In this model, the Drucker-Prager yield criterion was adopted and the yield surface on the deviatoric plane is a circle with an area approximately equal to that of the Mohr-Coulomb hexagon. It is well known that the yield surface of granular materials is greatly affected by the intermediate principal stress, but this is not taken into consideration in this model. Since the yield surface become close to the Mohr-Coulomb hexagon under the in-plane strain condition (B=0.2~0.5), the load bearing capacity is underestimated in the triaxial compression state (B=0) as shown in Fig. 6-7. Since the centrifugal model experiment is analyzed under the plane strain condition, the difference in strength is considered to be small.

The interface between sand and steel frame was set to a large compressive rigidity so as not to overlap, not to resist tension, and to have a lower coefficient of friction than sand as shown in Table 6-2. The simulated fault plane did not have a special angle, and a slit with no width (the coordinates of the two nodes sandwiching the slit match) was provided at the position where the fault displacement acts on the bottom of the sand layer. Due to this idealization, the movable floor moves while overlapping with the fixed floor at the slit part as the fault displacement increases.

Fig. 6-8 shows the changes in the ground surface shape up to a displacement of 50 mm on the movable floor and the deformations when the displacement is 50 mm. Both results obtained by experiments and analysis are compared. Before the formation of a clear shear band (less than 10 mm) in the analysis, the surface shape of the experiment can be accurately reproduced. On the other hand, when the local deformation in the shear band was predominant, there was a discrepancy in the ground surface shape in the experiment and analysis. Comparing the results when the displacement is 50 mm, the ground surface is deformed gently in the experiment, while the analysis shows local swelling at a point about 800 mm away from the fixed wall. This discrepancy is thought to occur because this constitutive model represents the mechanical properties of macroscopic sand aggregates, and the ground behavior near the ground surface where the confinement is almost zero is out of the applicable range. The reproducibility of the ground surface shape will be improved by using a modeling method that represents the behavior of microscopic sand particles. It was confirmed that the path of the shear band was almost the same between the experiment and the analysis.

The results of two simulations with different mesh size are compared in Fig. 6-9. In spite of the twice as difference of the element dimensions, the path of the shear band and the ground surface shape are almost the same. It was confirmed that the proposed modified dilatancy model worked well. Although there is much room for improvement, it was verified that the current model can reproduce the rough path of the shear band and can consider the element size dependence.

### Table 6-1 Input value for the centrifuge model test

| $G_0^{ref}$ [MPa] | $S_u^{ref}$ [MPa] | $\gamma_{peak}^{ref}$ [%] | $\rho_d$ [ton/m$^3$] | $D_r$ [%] | $c$ [MPa] | $\phi$ [deg] | $\phi_{res}$ [deg] | $L_{sb}$ [mm] | $\nu$ [-] |
|---|---|---|---|---|---|---|---|---|---|
| 42.9 | 0.233 | 4.0 | 1.53 | 90.0 | 0.0 | 44.4 | 37.4 | 3.0 | 0.30 |

$G_0^{ref}$, $S_u^{ref}$, $\gamma_{peak}^{ref}$: Reference skeleton curve initial shear modulus, shear strength and corresponding shear strain

$\rho_d$: Dry density, $D_r$: Relative Density, $c$: Cohesion, $\phi$: Friction angle, $\phi_{res}$: Friction angle at residual strength

### Table 6-2 Input value for joint interface elements of centrifuge model test

| Interface | Closure mode | | Opening mode | | Strength characteristics | | |
|---|---|---|---|---|---|---|---|
| | $K_s^c$ [MPa/m] | $K_n^c$ [MPa/m] | $K_s^o$ [MPa/m] | $K_n^o$ [MPa/m] | $\mu$ [-] | $f_t$ [MPa] | $\tau_f$ [MPa] |
| Sand-steel frame | 9.8E+3 | 2.0E+6 | 0.0 | 0.0 | 0.3 | 0.0 | 0.0 |

*$K_s^c$, $K_s^o$ : Shear stiffness, $K_n^c$, $K_n^o$ : Normal stiffness

(The subscripts c and o mean closure and opening, respectively.)

*$\mu$: Friction coefficient, $f_t$: Tensile strength, $\tau_f$: Shear strength
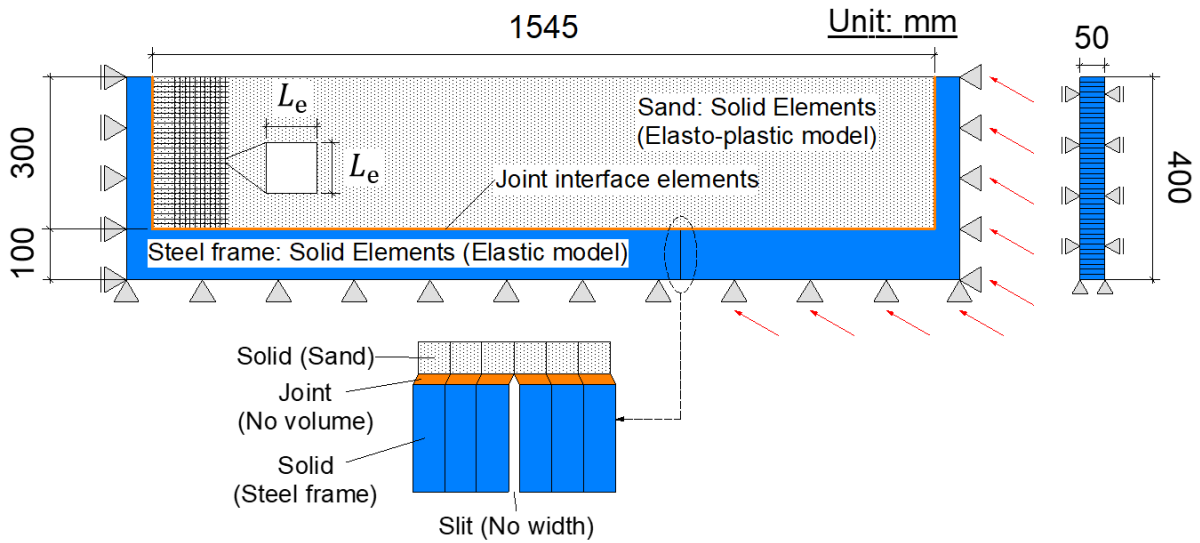
**Fig. 6-5  Analytical model of the centrifuge model test**



(a) Deviator stress

(b) Volumetric strain
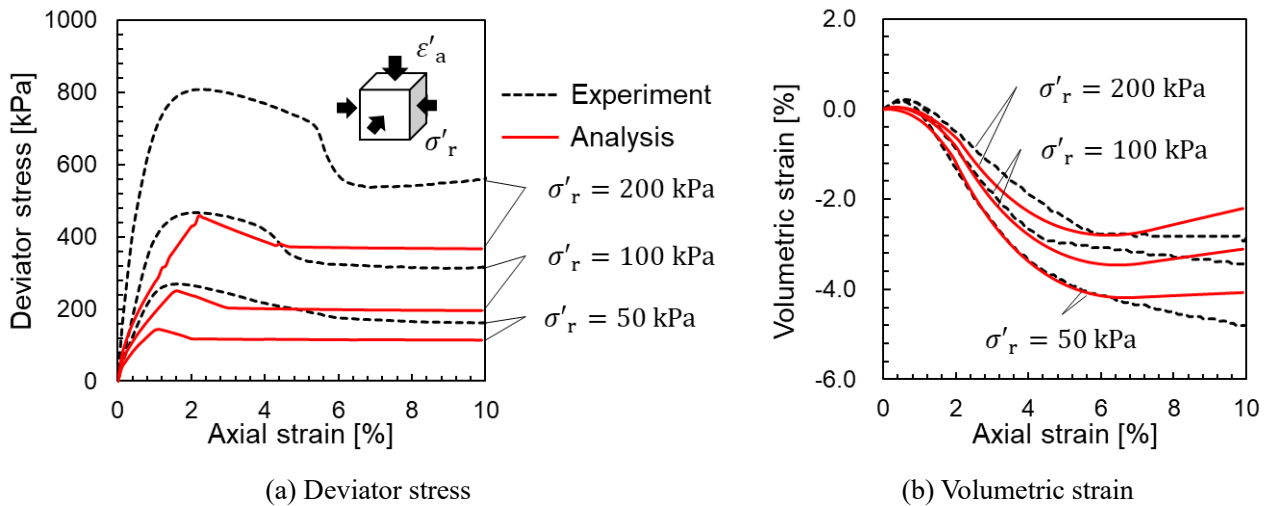
**Fig. 6-6  Parameter adjustment to match triaxial compression test results**



$$B = \frac{\sigma'_2 - \sigma'_3}{\sigma'_1 - \sigma'_3}$$

$$\sigma'_1 > \sigma'_2 > \sigma'_3$$
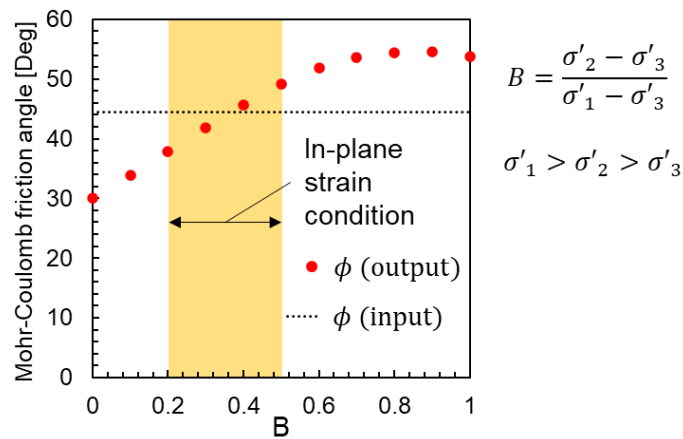
**Fig. 6-7  Friction angle according to the stress condition**
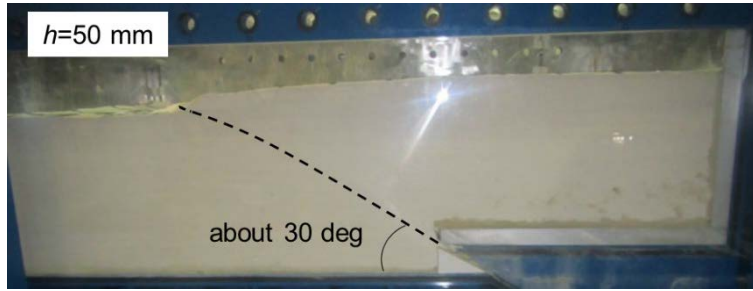
(a) Experimental result (Higuchi et al., 2017)
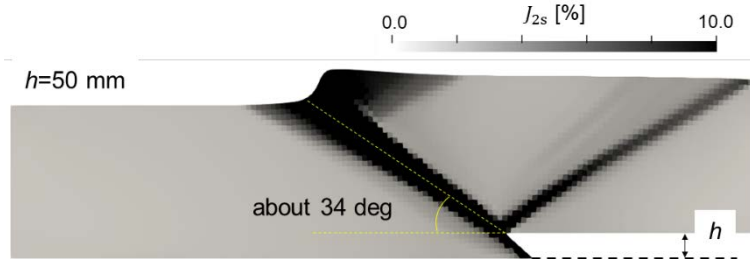


(b) Ultimate deformation obtained by the simulation (*Le*=10mm)
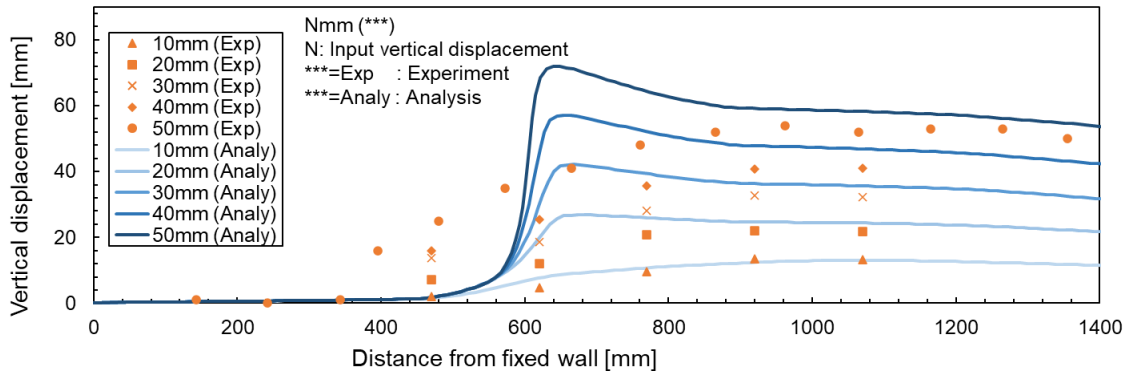


(c) Comparison of the shape of the ground surface between experiment and analysis

**Fig. 6-8  Comparison of the soil deformation between simulation and model test**
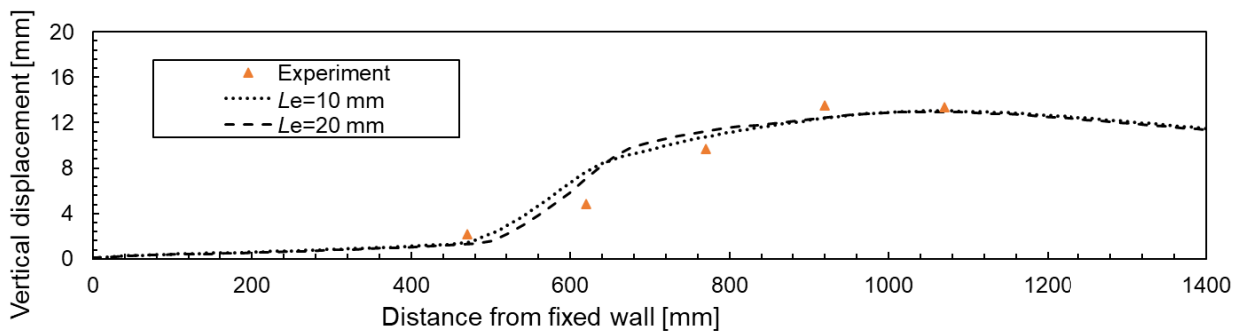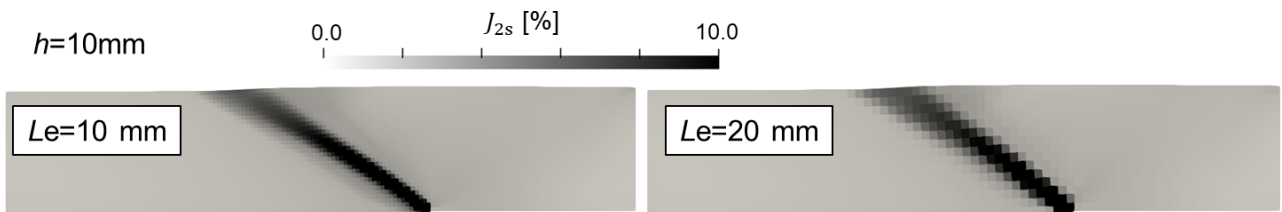


**Fig. 6-9  Mesh size dependency**

## 6.3 Evaluation of damage mitigation method for underground structures by MMR

### 6.3.1 Analytical model

An full-scale model in which a reverse fault acts on an underground RC duct directly supported by the bedrock was created as shown in Fig. 6-10. The slope of the fault is 45 degrees, and an ideal situation is assumed in which the axis of the duct and the fault line are parallel. The width of the fracture zone is 500 mm. The 8-nodes hexahedral elements were used for the RC duct, bedrock and backfilled soil. The targeted RC duct has a dimension of 4.5 m in height and width. The topsoil was 15 m high, and the bedrock from the bottom of the duct to 5 m was modeled. The bedrock and ground were modeled up to a length of 100 m from the fault line, which satisfies the recommendation of Bray, (1990). A region with a depth of 200 mm was extracted and forced displacement corresponding to dip-slip of fault was given to the bedrock under plane strain condition. The case where the fault line extends to just below the RC duct and the case where the MMR layer with a height of 4 m is placed between them were compared.

The input values for each material are summarized in Table 6-3 and 6-4. The RC model representing the average stress-strain relationship of finite elements comprising multi-directional smeared cracks and dispersed reinforcement was used for the RC duct. Main reinforcement and stirrup are placed at a ratio of 0.64% and 0.66% to the member cross section of the duct. The width of the member was divided into three meshes, and the reinforcement was considered only in the surface elements. The constitutive model mentioned in previous section was applied to the surrounding soil. The skeleton curve and dilatancy parameters of Toyoura sand was adopted as input (Fig. 6-4). The bedrock is assumed to be hard rock with an S wave speed equivalent to 700 m/sec. As a difficult situation for the RC duct, it was modeled as an elastic body. As shown in Fig. 6-10 (b) and Table 6-5, joint interface elements that can reproduce peeling and slipping were placed at the boundaries between different materials.

The proposed transition model was applied to the fault fracture zone and MMR. In general, the former is modeled by the joint interface element to deal with the localized large deformation. By setting a low friction in the proposed model, the joint element can be replaced with the solid element. The coefficient of friction after the transition was set to 0.1 as a condition to almost ignore the shear resistance of the crush zone. The concrete properties of the MMR were determined with reference to the measured values of the one used at the Kashiwazaki-Kariwa nuclear power plant (91 days strength), and the coefficient of friction after the transition was set to 1.0, which was identified in **Chapter 3**.

#### Table 6-3  Input value for concrete elements

|  | $f'_c$ [MPa] | $E_0$ [GPa] | $f_t$ [MPa] | $\nu$ [-] | $\rho$ [ton/m$^3$] |
|---|---|---|---|---|---|
| Duct | 24.0 | 25.0 | 1.91 | 0.17 | 2.45 |
| Fault fracture zone* | 1.00 | 1.96 | 0.10 | 0.20 | 2.50 |
| MMR* | 3.60 | 6.08 | 0.67 | 0.20 | 1.75 |

*Transition model is applied

**Table 6-4  Input value for soil elements**

| $\rho_d$ [ton/m³] | $D_r$ [%] | $c$ [MPa] | $\phi$ [deg] | $\phi_{res}$ [deg] | $L_{sb}$ [mm] | $\nu$ [-] |
|---|---|---|---|---|---|---|
| 1.80 | 89.2 | 0.0 | 42.0 | 32.0 | 50.0 | 0.30 |

**Table 6-5  Input value for joint interface elements**

| No. | Closure mode | | Opening mode | | Strength characteristics | | |
|---|---|---|---|---|---|---|---|
| | $K_s^c$ [MPa/m] | $K_n^c$ [MPa/m] | $K_s^o$ [MPa/m] | $K_n^o$ [MPa/m] | $\mu$ [-] | $f_t$ [MPa] | $\tau_f$ [MPa] |
| 1 | 9.8E+3 | 2.0E+6 | 0.0 | 0.0 | 0.0 | 0.0 | 0.0 |
| 2 | 9.8E+3 | 2.0E+6 | 0.0 | 0.0 | 0.3 | 0.0 | 0.0 |
| 3 | 9.8E+3 | 2.0E+6 | 0.0 | 0.0 | 1.5 | 0.5 | 3.4 |
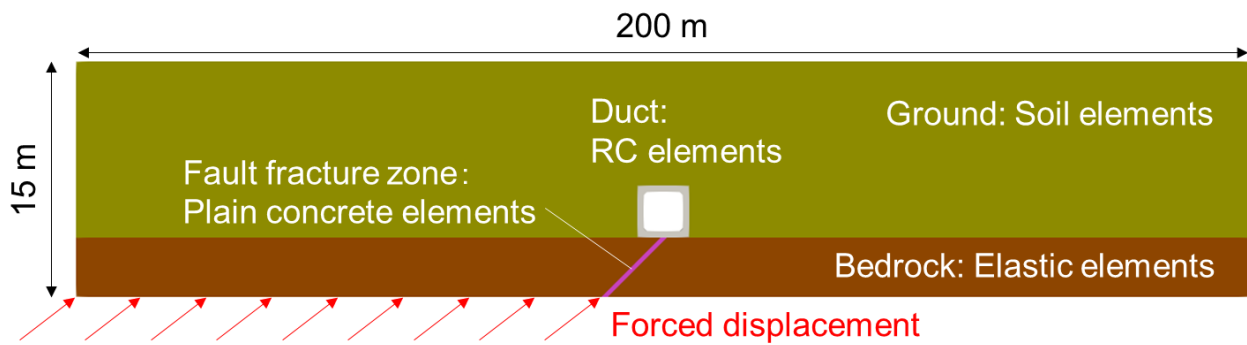


(a) Overview
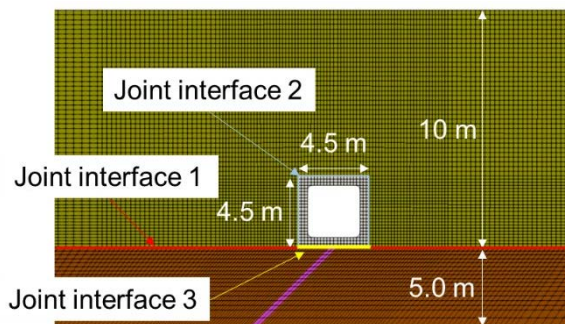


(b) Mesh discretization (without MMR)
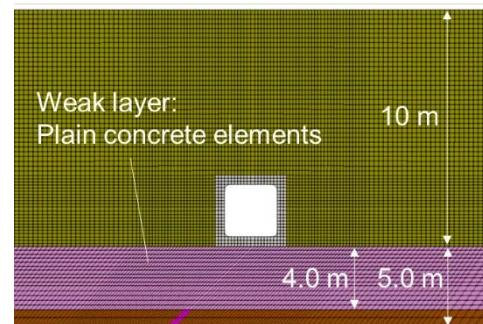
(c) Mesh discretization (with MMR)

**Fig. 6-10  Full-scale model of the underground RC duct**

### 6.3.2 Damage evaluation of the RC duct

Fig. 6-11 shows the failure modes with and without MMR at a vertical displacement of 500 mm at the bottom of the bedrock. In both cases, by applying the proposed model, the local deformation of the fracture zone was reproduced as intended. The RC duct is subjected to bending fracture due to the action of fault displacement and earth pressure. As a result of the interaction between the RC duct and surrounding soil, the shear band in the soil forms from the edge of the duct. These trends are consistent with the result of the centrifuge model test of the box culvert (Higuchi et al., 2017). If MMR is present under the RC duct, the shear band progresses avoiding the duct and the duct deformation is less than in the case without MMR.

In order to evaluate the mitigating effect quantitatively, the tensile strain at the corner and deformation angle against the fault displacement in each case were compared as shown in Fig. 6-12. Here, the former represents the local bending fracture while the latter represents the global one. Both parameters indicate that MMR has alleviated RC duct damage. In all cases, the tensile strain exceeded the yield strain of the reinforcement at an early stage, but with MMR, the increase is more gradual, and the final strain is 40% less than without MMR. Regarding the deformation angle, it has been reported from the results of experiments and analysis that the lower limit of the deformation angle at the time of bending compression fracture is about 1.0 % (Miyagawa et al., 2000). When the limit deformation angle is set to 1.0 %, it is judged that the presence of MMR can more than double the limit fault displacement at the ultimate state of the RC duct.

Next, the case study was conducted to investigate the effect of the arrangement of MMR. As shown in Fig. 6-13, two model was prepared. One is a case where the height of MMR is 2.5 m (Fig. 6-13 (a)), and the other is a case where the length is 15 m (Fig. 6-13 (b)). Other analytical conditions, including the material property of MMR, is not changed. The analysis results of both cases are compared in Fig. 6-14 and 6-15. When the height of the weak layer was low, the branched shear band could not avoid the duct, and the damage mitigation effect was not seen. The deformation angle is rather larger than the case without MMR. This is thought to be due to the change in the shear path, which moved the point of action of the fault closer to the corner, resulting in an increase in the bending span of the bottom slab of the duct. On the other hand, given sufficient height, the length of MMR did not significantly affect the mitigation effects. Under the conditions set in this analysis, the shorter the MMR length, the greater the mitigation effect. In the shorter case ($H$=2.5m in Fig. 6-15), it was confirmed that the duct can tolerate displacements up to 500 mm with MMR. From past field surveys, the displacement of the secondary fault is considered to be up to 500 mm. It was indicated that it would be possible to design the underground structure so that it could withstand the expected fault displacement by devising the arrangement and physical properties of MMR.

The friction coefficient of MMR was set to 1.0 with reference to the experimental results of concrete with the uniaxial compressive strength of 2.0 ~ 8.0 MPa. However, the coefficient of friction after the transition changes depending on the material, and in **Chapter 3**, it is identified as 0.4 in the case of mortar. Therefore, the sensitivity of the mitigation effect to friction was investigated by using the model with MMR height of 2.5 m. As a result of setting the coefficient of friction to 0.3, the shear band diverged neatly into two, avoiding the duct as shown in Fig. 6-16. Focusing on the deformation angle (Fig. 6-17), it can be seen that the damage mitigation effect could be improved by assuming lower the coefficient of friction. It was implied that materials with a small residual friction coefficient, such as mortar, are suitable as seismic isolation materials.
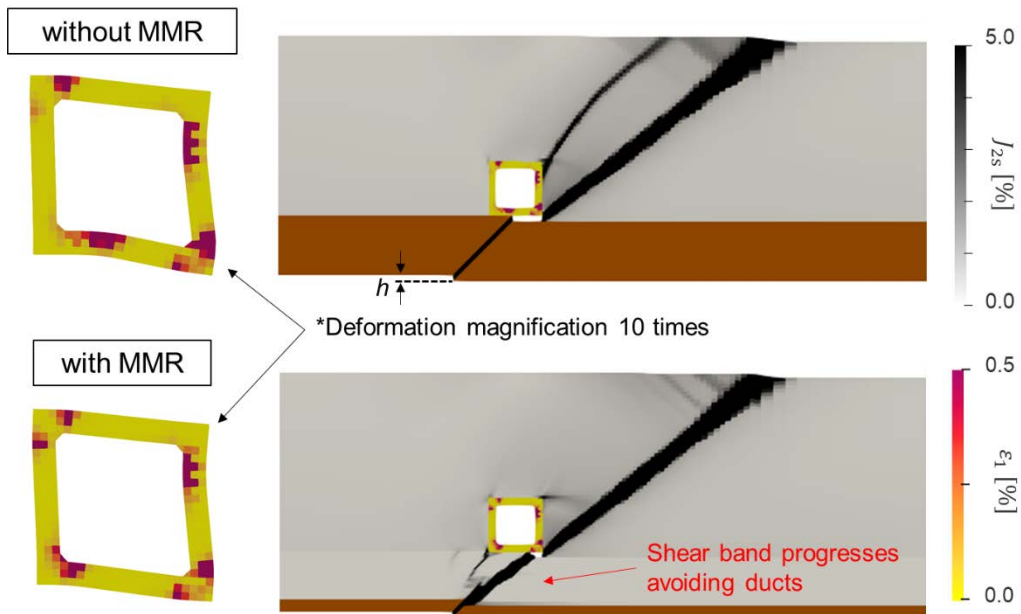
**Fig. 6-11    Comparison of failure modes with and without MMR (*h*=500mm)**
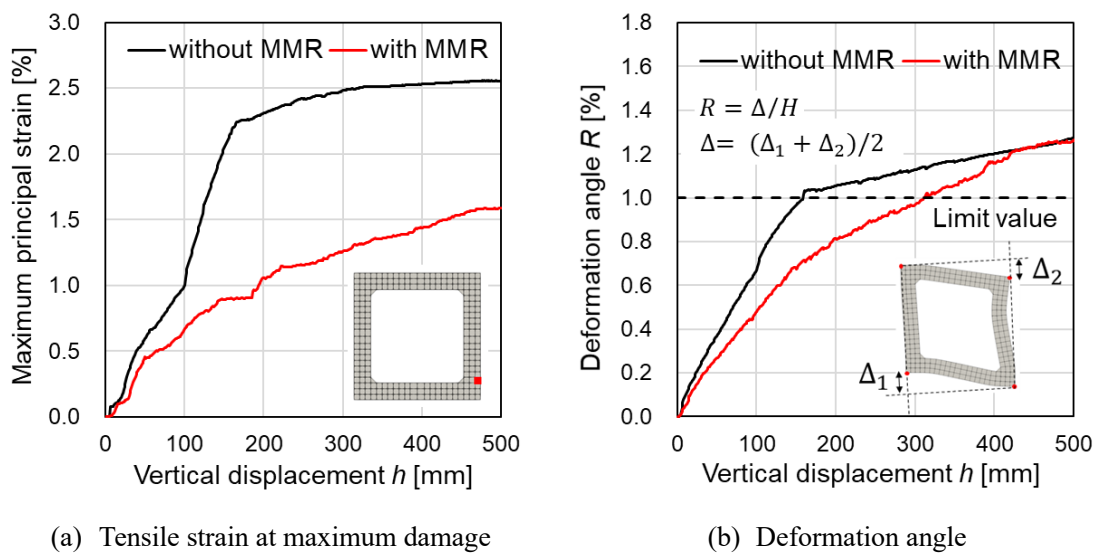


(a)  Tensile strain at maximum damage

(b)  Deformation angle

**Fig. 6-12    Comparison of damages of the RC duct with and without MMR**
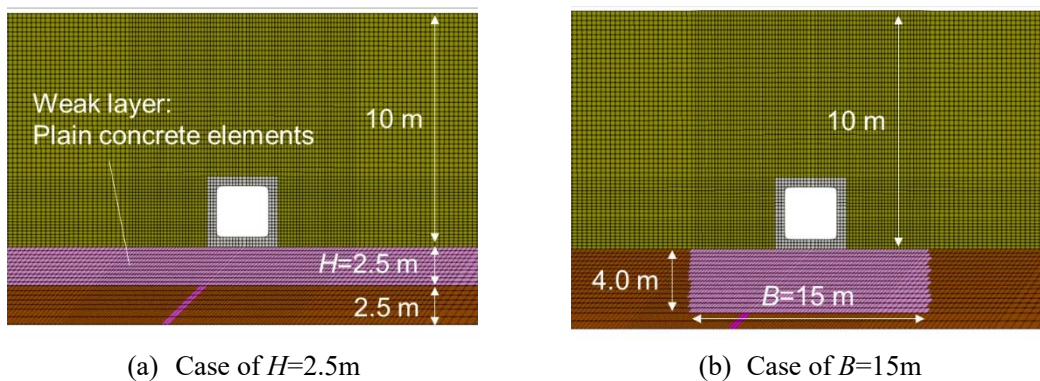


(a)  Case of *H*=2.5m

(b)  Case of *B*=15m

**Fig. 6-13    Model for case study**

91

with MMR (*H*=2.5m)

Branch fault hits
the duct directly

*Deformation magnification 10 times

with MMR (*B*=15m)

Similar result to assuming
a semi-infinite width
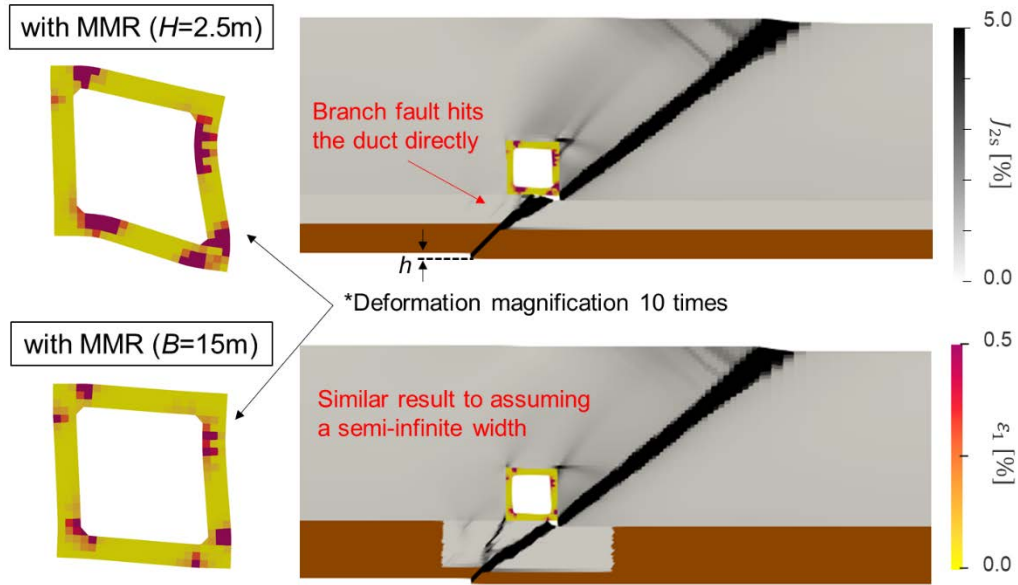
**Fig. 6-14   Comparison of failure modes in each case (*h*=500mm)**



$$R = \Delta/H$$
$$\Delta = (\Delta_1 + \Delta_2)/2$$
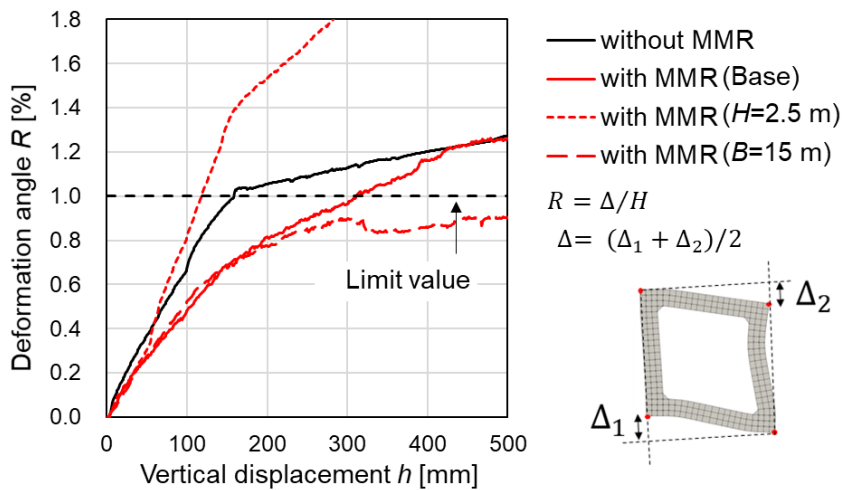
**Fig. 6-15   Comparison of deformation angle of the duct in each case**



with MMR ($\mu = 0.3$)

$\varepsilon_1$ [%]

$J_{2s}$ [%]

*Deformation
magnification 10 times

Shear band progresses
around the structure
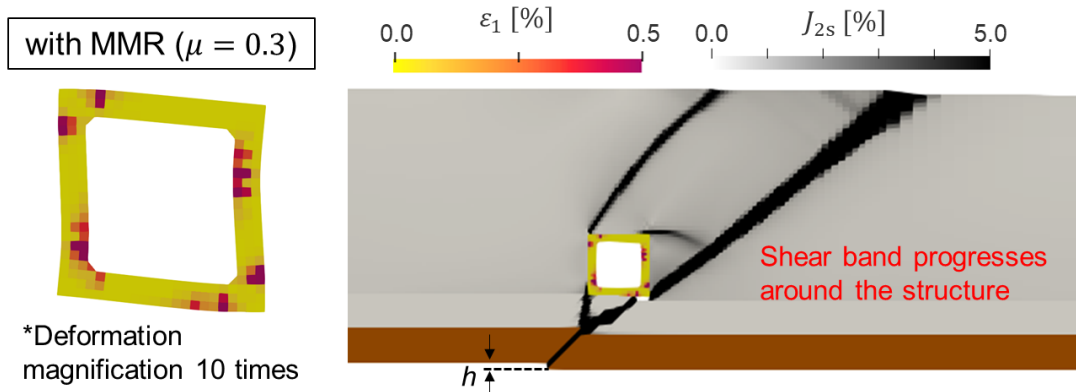
**Fig. 6-16   Changes in failure mode for different coefficients of friction (*h*=500mm)**

92
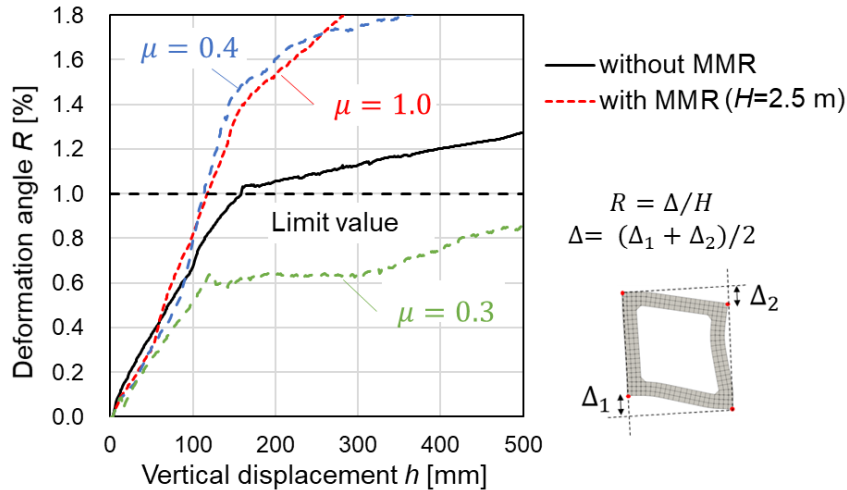
**Fig. 6-17  Comparison of deformation angles of the duct for different coefficients of friction**

Then, it will be qualitatively evaluated whether the MMR at the Kashiwazaki-Kariwa nuclear power plant can relieve the damage to the reactor building. The measured uniaxial compressive strength of MMR was between 4.5 MPa and 6.5 MPa 3000 days after casting, which is slightly larger than the setting value in Table 6-3. In the experiment shown in **Chapter 3**, even if the strength of the weak layer was different between 8 MPa and 2 MPa, there was no big difference in the load bearing capacity, so this difference in strength is considered to be not so significant. On the other hand, the width of reactor building is more than ten times that of the above RC duct. It is predicted that the required depth of MMR to make the shear band bypass the structure increase when the width of structure increases. Assuming the linear relationship, more than 40 m depth of MMR would be required for the reactor building. This is an unrealistically large value compared to the actual depth (about 5 m to 20 m). However, the friction coefficient can be regard to less than 0.4 since coarse aggregates were not included in the MMR used in the Kashiwazaki-Kariwa nuclear power plant. Considering that the bending resistance due to the wall is large, the damage mitigation effect may be exhibited even in a relatively shallow MMR layer depending on the friction coefficient and the position of intersection with the fault line. The author plans to evaluate it by simulation in the future.

6.4    Summary of Chapter 6

The focus was on artificial soft rocks called Man-Made-Rock (MMR) as a material to mitigate damage to underground structures due to fault displacement. A transition model whose validity was verified by model experiments in **Chapter 3** was applied to MMR and the fault fracture zone which subject to localized large deformation. After confirming the applicability of the soil model to the ground including shear band, the damage assessment of the underground RC duct subjected to the fault displacement was conducted by using full-scale model. The conclusions are summarized as below.

i. By proposing a dilatancy model of sand that takes mesh size dependency into consideration, it was confirmed that the behavior of the sand layer subject to fault displacement in the centrifuge model test can be roughly reproduced.

ii. Using proposed model makes it possible to replace the joint interface element with the solid element and to improve the reliability of the evaluation of the mitigation effect by MMR.

iii. MMR underlying the RC duct can mitigate the duct damage by changing the path of the shear band.

iv. The mitigation effect depends on the arrangement and friction angle of MMR. The higher the MMR area, or the lower the friction, the greater the damage reduction effect can be expected.

References of Chapter 6

Alshibli, K.A., Sture, S., 1999. Sand shear band thickness measurements by digital imaging techniques. *Journal of Computing in Civil Engineering 13*, 103–109. https://doi.org/10.1061/(ASCE)0887-3801(1999)13:2(103)

Anastasopoulos, I., Gazetas, G., 2007. Foundation–structure systems over a rupturing normal fault: Part I. Observations after the Kocaeli 1999 earthquake. *Bulletin of Earthquake Engineering 5*, 253–275. https://doi.org/10.1007/s10518-007-9029-2

Anastasopoulos, I., Gazetas, G., Bransby, M.F., Davies, M.C.R., EI Nahas, A., 2007. Fault rupture propagation through sand: Finite-element analysis and validation through centrifuge experiments. *Journal of Geotechnical and Geoenvironmental Engineering 133*, 943–958. https://doi.org/10.1061/(ASCE)1090-0241(2007)133:8(943)

Bray, J.D., 1990. The effects of tectonic movements on stresses and deformations in earth embankments. University of California, Berkeley.

Cole, D.A., Lade, P. V., 1984. Influence zones in alluvium over dip-slip faults. *Journal of Geotechnical Engineering 110*, 599‐615. https://doi.org/10.1061/(ASCE)0733-9410(1984)110:5(599)

Fadaee, M., Anastasopoulos, I., Gazetas, G., Jafari, M.K., Kamalian, M., 2013. Soil bentonite wall protects foundation from thrust faulting: analyses and experiment. *Earthquake Engineering and Engineering Vibration 12*, 473–486. https://doi.org/10.1007/s11803-013-0187-8

Gutierrez, M., Ishihara, K., Towhata, I., 1993. Model for the deformation of sand during rotation of principal stress directions. *Soils and Foundations 33*, 105–117. https://doi.org/10.3208/sandf1972.33.3_105

Haraguchi, R., Tanaka, F., Ebisawa, K., Sakai, T., Tsutsumi, H., Yuyama, A., Sato, K., Mihara, Y., Nikaido, Y., Yoshida, S., 2020. Development of fault displacement PRA methodology and its application to a hypothetical NPP. *Nuclear Engineering and Design 361*, 110433. https://doi.org/10.1016/j.nucengdes.2019.110433

Hatakeyama, D., Shoji, G., Nagata, S., Yoshimi, M., 2020. Seismic damage mechanism of sewer buried pipes by surface ruptures in the 2016 Kumamoto earthquake. *Journal of Japan Society of Civil Engineers, Ser. A1 (Structural Engineering & Earthquake Engineering (SE/EE)) 76*, I_441-I_453. https://doi.org/10.2208/jscejseee.76.4_I_441

Higuchi, S., Kato, I., Sato, S., Itoh, G., Sato, Y., 2017. Experimental and numerical study on the characteristics of earth pressure acting on the box-shape underground structure subjected the strike slip fault displacement. *Journal of Japan Society of Civil Engineers, Ser. A1 (Structural Engineering & Earthquake Engineering (SE/EE)) 73*, I_19-I_31. https://doi.org/10.2208/jscejseee.73.I_19

International Atomic Energy Agency, 2019. *Site Evaluation for Nuclear Installations: Specific Safety Requirements.*

Itoh, G., Yamaguchi, K., Hida, Y., Nagai, H., Tsutsumiuchi, T., Yonezawa, K., 2020. Damage evaluation by nonlinear 3D analysis on RC underground structure subjected to fault displacement. *Journal of Japan Society of Civil Engineers, Ser. A1 (Structural Engineering & Earthquake Engineering (SE/EE)) 76*, 180–196. https:

//doi.org/10.2208/jscejseee.76.1_180

Japan Nuclear Safety Institute, 2013. *Assessment Methods for Nuclear Power Plant Against Fault Displacement.* JANSI-FDE-01 rev.1.

Kawashima, K., 2002. Faulting and fault-induced damages and disasters: Damage of bridges resulting from fault rupture in the 1999 Kocaeli and Duzce, Turkey earthquakes and the 1999 Chi-chi, Taiwan earthequake. *Structural Engineering / Earthquake Engineering 19*, 179S-197S. https://doi.org/10.2208/jsceseee.19.179s

Konagai, K., Johansson, J., Zafeirakos, A., Numada, M., Sadr, A.A., 2005. Damage to tunnels in the October 23, 2004 Chuetsu earthquake. *JSCE Journal of Earthquake Engineering 28*, 75. https://doi.org/10.11532/proee2005a.28.75

Kontogianni, V.A., Stiros, S.C., 2003. Earthquakes and seismic faulting: effects on tunnels. *Turkish Journal of Earth Sciences 12*, 153–156.

Kurihara, H., Kikuchi, K., Fukazawa, E., 1994. Experimental study on durability of artificial soft rock. *Doboku Gakkai Ronbunshu 1994*, 85–94. https://doi.org/10.2208/jscej.1994.486_85

Lin, A., Ren, Z., Jia, D., Wu, X., 2009. Co-seismic thrusting rupture and slip distribution produced by the 2008 Mw 7.9 Wenchuan earthquake, China. *Tectonophysics 471*, 203–215. https://doi.org/10.1016/j.tecto.2009.02.014

Miyagawa, Y., Matsumoto, T., Kanatsu, T., 2000. An evaluation method of deformation capacity of RC box culvert. *Report of Central Research Institute of Electric Power Industry U00015*.

Nakamura, Y., 1990. Possible fault displacements in dam foundations. Part 1. Examples of faulting near dams. *Journal of the Japan Society of Engineering Geology 31*, 207–215. https://doi.org/10.5110/jjseg.31.207

Narabayashi, T., Kamiya, M., 2017. Risk evaluation method for faults displacement by engineering approach. *The Proceedings of the National Symposium on Power and Energy Systems 2017.22*, A123. https://doi.org/10.1299/jsmepes.2017.22.A123

Ohmachi, T., 2000. On damage to dams in Taiwan due to the 1999 Chi-chi earthquake. *Journal of Japan Society of Dam Engineers 10*, 138–150. https://doi.org/10.11315/jsde1991.10.138

Ohsaki, Y., 1980. Some notes on Masing's Law and nonlinear response of soil deposits. *Journal of the Faculty of Engineering*, the University of Tokyo (B) XXXV.

Pamuk, A., Kalkan, E., Ling, H.I., 2005. Structural and geotechnical impacts of surface rupture on highway structures during recent earthquakes in Turkey. *Soil Dynamics and Earthquake Engineering 25*, 581–589. https://doi.org/10.1016/j.soildyn.2004.11.011

Petersen, M.D., Dawson, T.E., Chen, R., Cao, T., Wills, C.J., Schwartz, D.P., Frankel, A.D., 2011. Fault displacement hazard for strike-slip faults. *Bulletin of the Seismological Society of America 101*, 805–825. https://doi.org/10.1785/0120100035

Sabagh, M., Ghalandarzadeh, A., 2020. Numerical modelings of continuous shallow tunnels subject to reverse faulting and its verification through a centrifuge. *Computers and Geotechnics 128*, 103813. https://doi.org/10.1016/j.compgeo.2020.103813

Shibuya, S., Tatsuoka, F., Teachavorasinskun, S., Kong, X.J., Abe, F., Kim, Y.-S., Park, C.-S., 1992. Elastic deformation properties of geomaterials. *Soils and Foundations 32*, 26–46. https://doi.org/10.3208/sandf1972.32.3

_26

Shiozaki, I., Matsuura, K., Hiramatsu, S., 2018. Active fault measures described in guidelines and standards. *Journal of the Japan Society of Engineering Geology 59*, 94–100. https://doi.org/10.5110/jjseg.59.94

Soltani, M., Maekawa, K., 2015. Numerical simulation of progressive shear localization and scale effect in cohesionless soil media. *International Journal of Non-Linear Mechanics 69*, 1–13. https://doi.org/10.1016/j.ijnonlinmec.2014.10.014

Takao, M., Annaka, T., Kurita, T., 2018. Establishment of evaluation formulae for probabilistic fault displacement hazard analysis (PFDHA) in Japan. *International Atomic Energy Agency (IAEA).*

The Nuclear Civil Engineering Committee of the JSCE, 2015. *Research Report of the Subcommittee on Fault Displacement Evaluation.*

Towhata, I., 2008. *Geotechnical Earthquake Engineering*. Springer Berlin Heidelberg, Berlin, Heidelberg. https://doi.org/10.1007/978-3-540-35783-4

Towhata, I., Ishihara, K., 1985. Undrained strength of sand undergoing cyclic rotation of principal stress axes. *Soils and Foundations 25*, 135–147. https://doi.org/10.3208/sandf1972.25.2_135

Tsinidis, G., de Silva, F., Anastasopoulos, I., Bilotta, E., Bobet, A., Hashash, Y.M.A., He, C., Kampas, G., Knappett, J., Madabhushi, G., Nikitas, N., Pitilakis, K., Silvestri, F., Viggiani, G., Fuentes, R., 2020. Seismic behaviour of tunnels: From experiments to analysis. *Tunnelling and Underground Space Technology 99*, 103334. https://doi.org/10.1016/j.tust.2020.103334

Wang, T.-T., Kwok, O.-L.A., Jeng, F.-S., 2021. Seismic response of tunnels revealed in two decades following the 1999 Chi-Chi earthquake (Mw 7.6) in Taiwan: A review. *Engineering Geology 287*, 106090. https://doi.org/10.1016/j.enggeo.2021.106090

Wang, W.L., Wang, T.T., Su, J.J., Lin, C.H., Seng, C.R., Huang, T.H., 2001. Assessment of damage in mountain tunnels due to the Taiwan Chi-Chi Earthquake. *Tunnelling and Underground Space Technology 16*, 133–150. https://doi.org/10.1016/S0886-7798(01)00047-5

Youngs, R.R., Arabasz, W.J., Anderson, R.E., Ramelli, A.R., Ake, J.P., Slemmons, D.B., McCalpin, J.P., Doser, D.I., Fridrich, C.J., Swan, F.H., Rogers, A.M., Yount, J.C., Anderson, L.W., Smith, K.D., Bruhn, R.L., Knuepfer, P.L.K., Smith, R.B., dePolo, C.M., O'Leary, D.W., Coppersmith, K.J., Pezzopane, S.K., Schwartz, D.P., Whitney, J.W., Olig, S.S., Toro, G.R., 2003. A Methodology for probabilistic fault displacement hazard analysis (PFDHA). *Earthquake Spectra 19*, 191–219. https://doi.org/10.1193/1.1542891

Zheng, Q., Liu, X., Zhang, H., Gu, X., Fang, M., Wang, L., Adeeb, S., 2021. Reliability evaluation method for pipes buried in fault areas based on the probabilistic fault displacement hazard analysis. *Journal of Natural Gas Science and Engineering 85*, 103698. https://doi.org/10.1016/j.jngse.2020.103698

# 7    Conclusion and Future Task

## 7.1    Conclusion

In order to improve the model accuracy for concrete structures in the ultimate state until concrete breaks down to gravel, a simple constitutive model that represents the transition of physical properties from concrete to granular material was proposed. In **Chapter 3**, graveling of low-strength concrete with a compressive strength of 2 to 8 MPa was observed in experiments and confirmed that its structural response could be reproduced by using the proposed model. In **Chapter 4**, it was clarified that graveling occurs even if the strength is not low when subjected to cyclic loading, and the validity of the proposed model for ordinary-strength concrete was verified by the shear failure experiment of DBCB. In **Chapter 5 and 6**, the scope of application of proposed model was extended to the two cases, masonry structures and the fault rupture problem. The main conclusions of this study are summarized below.

i. The validity of the model was verified by comparison with the past push-off test results, and the residual friction coefficient of concrete was identified as 1.0 for normal-strength concrete.

ii. Even if the compressive strength is about 2 MPa, if the composite matrix has coarse aggregate, a large shear force is transferred under confinement even after great fracture. In the case of mortar, the shear transfer capacity at disintegration becomes much smaller.

iii. The transition model was confirmed to upgrade the post-peak structural analysis of reinforced concrete, especially for structural members that include very small strength layers of concrete or is locally subjected to cyclic loading.

iv. The frictional coefficient after the transition to graveling in the shear bands was identified as 1.0 regardless of the compressive strength of concrete and the loading condition but it depends on the existence of the coarse aggregate.

v. From the result of parametric study, it is clarified that the coefficient of friction is the most dominant factor, and it is possible to roughly match the actual phenomenon by changing this value.

vi. The multi-directional fixed crack model can be extended to masonry structures by a simple modification and transition model shows good applicability to the mortar joint.

vii. Using proposed model makes it possible to replace the joint element with the solid element and to improve the reliability of the evaluation of the mitigation effect by MMR.

## 7.2    Future tasks

The validity and effectiveness of the proposed model were exhibited for structural concrete that collapses beyond the scope of the existing model. However, several improvements have been identified as below.

Future Task 1: Establishment of the identification method of post-transition physical properties

Future Task 2: Verification of applicability to concrete with a wider range of strength

Future Task 3: Verification and sophistication of the model for the ground subjected to fault displacement

Regarding Task 1, as different values were identified for concrete and mortar, it is considered that the coefficient of friction after transition changes depending on the constituent materials. Moreover, a value similar to that of gravels consolidated under 0.5 kgf/cm$^2$ was tentatively set as a stiffness after graveling, and the confinement dependency of stiffness has not taken into account. Currently, these physical property values are back-estimated from structural analysis, but ideally they should be obtained from material testing. In addition, it is expected that the analysis accuracy will be improved by more strictly considering the confinement dependency after the transition.

Regarding Task 2, those with low strength down to the level of ground improvement materials are considered to exhibit properties similar to sand and clay from the beginning of the fracture. On the other hand, in high-strength concrete, since the crack surface is smooth, it is considered that graveling is unlikely to occur as shown in Fig. 7-1. In order for the proposed model to cope with these extreme cases, it is necessary to accumulate data on the fracture of concrete of various strengths under various restraint pressures.

Regarding Task 3, in order to accurately evaluate the post-peak behavior of underground structures, it is necessary to upgrade not only RC structures but also models of surrounding ground. For sand subjected to fault displacement, there was a room for improvement in the dilatancy model. Since advanced models have already been proposed for soil, it is expected that a more sophisticated analysis system will be constructed by combining these with advanced concrete models.

In this study, priority was given to the simplicity, but it is hoped that it will be upgraded little by little in the future in order to expand its versatility. As future applications, attention is being paid to rocks containing multiple crush zones and joints of concrete pavement. Especially, since rocks have a wide variety of strengths, constitutive models based on continuum elasto-plasticity or elasto-fracture plasticity have been mainly developed for soft rocks (Adachi and Oka, 1995), whereas models considering discontinuous surfaces has also developed for relatively hard rocks (Uno et al., 2002). The former is close to the uncracked concrete model assuming isotropy used in this study. On the other hand, some of the latter model the average behavior of rocks including discontinuous surfaces, similar to the model of cracked concrete (Sasaki et al., 1994; Tasaka et al., 2000). In recent years, seismic response analysis using these models has been conducted mainly for nuclear facilities (Ito et al., 2021; Yoshinaka et al., 2014). However, there is still no model that can simultaneously consider the softening behavior of intact rocks and local deformation at discontinuous surfaces. In this study, the concrete model was extended to masonry structures including joints, but it is possible to extend its applicability to rock mass including discontinuous surfaces in advance in the same way. It is expected that the proposed model will enhance the response evaluation of concrete structures coupled with rocks that undergo complex fractures.
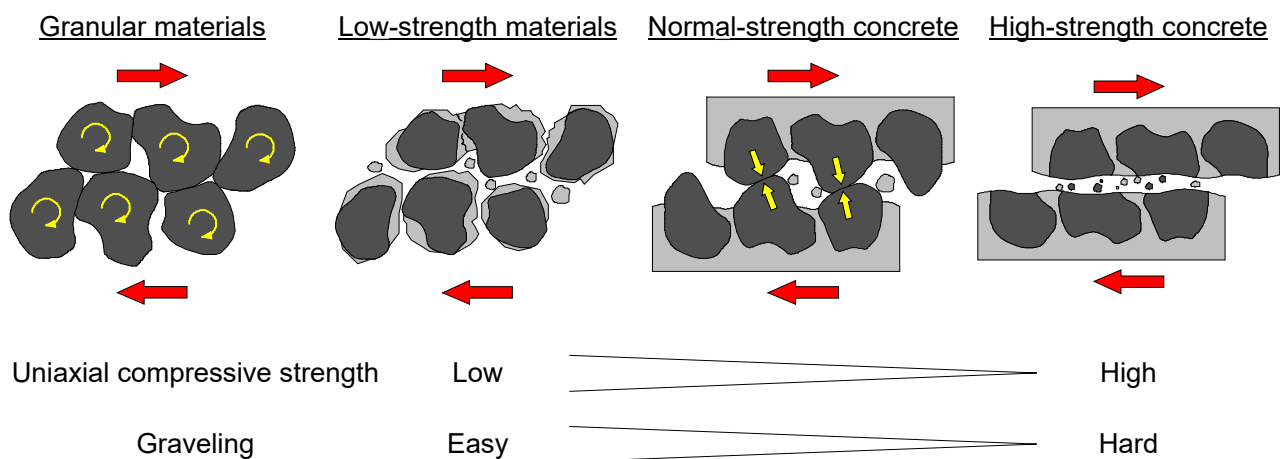


**Fig. 7-1　Changes in shear failure due to differences in strength**

References of Chapter 7

Adachi, T., Oka, F., 1995. An elasto-plastic constitutive model for soft rock with strain softening. *International Journal for Numerical and Analytical Methods in Geomechanics 19*, 233–247. https://doi.org/10.1002/nag.1610190402

Ito, K., Wani, M., Saito, S., Suzuki, S., Terada, K., 2021. Development and verification of seismic response analysis method of layered rock mass by using homogenization method. *Journal of Japan Society of Civil Engineers, Ser. A1 (Structural Engineering & Earthquake Engineering (SE/EE)) 77*, I_394-I_405. https://doi.org/10.2208/jscejseee.77.4_I_394

Sasaki, T., Yoshinaka, R., Nagai, F., 1994. A study of the multiple yield models on jointed rock mass by finite element method. *Doboku Gakkai Ronbunshu 1994*, 59–68. https://doi.org/10.2208/jscej.1994.505_59

Tasaka, Y., Uno, H., Ohmori, T., Kudoh, K., 2000. A joint and rock failure strain-softening model and its application to the excavation simulation of large-scale underground caverns. *Doboku Gakkai Ronbunshu 2000*, 73–90. https://doi.org/10.2208/jscej.2000.652_73

Uno, H., Ishida, T., Mizuta, Y., 2002. Historical changes of rock mass modelling and numerical technique and the features of those. *Shigen-to-Sozai 118*, 150–156. https://doi.org/10.2473/shigentosozai.118.150

Yoshinaka, R., Iwata, N., Sasaki, T., 2014. Seismic response analysis for foundation of large-scale structure on discontinuous rock -as a basic example used the 2011 off the pacific coast of Tohoku earthquake-. *Journal of Japan Society of Civil Engineers*, Ser. C (Geosphere Engineering) 70, 16–32. https://doi.org/10.2208/jscejge.70.16

# Acknowledgments

# List of Related Papers

*Journal*

Yamanoi, Y. and Maekawa, K., 2020. Shear bifurcation and graveling of low-strength concrete. *Journal of Advanced Concrete Technology 18*, 767–777. https://doi.org/10.3151/JACT.18.767

Yamanoi, Y., Miura, T., Soltani, M. and Maekawa, K., 2021. Multi-directional fixed crack model extended to masonry structures. *Journal of Advanced Concrete Technology 18*, 977-987. https://doi.org/10.3151/jact.19.977

Yamanoi, Y. and Maekawa, K., 2022. Disintegration of low and normal strength concrete in shear localized bands and its constitutive modeling. *Engineering Structures 266*, Elsevier. https://doi.org/10.1016/j.engstruct.2022.114593


*Conference paper (Peer-reviewed)*

山野井悠翔, 松尾豊史, 山口和英, 島村真介, 2019. 地盤断層と地中 RC ボックスカルバートの相互作用と損傷モード. *理論応用力学講演会 講演論文集 66*.

山野井悠翔, 前川宏一, 2022. 逆断層変位を受ける岩盤—RC—地盤連成系の実規模解析. *コンクリート工学年次論文集 41*.

Yamanoi, Y. and Maekawa, K., 2019. Interaction of shear band of rock/soil foundation and failure of underground RC ducts. *Proceedings of 3 rd International Conference on International Conference on Recent Advances in Nonlinear Design, Resilience and Rehabilitation of Structures, CoRASS 2019*, H. Barros, C. Ferreira, José M. Adam and Norb Delatte (Eds).

Yamanoi, Y. and Maekawa, K., 2022. Transient shear band and its kinetics around interfaces of cementitious materials and soil/rock foundation. *Computational Modelling of Concrete and Concrete Structures.* 381-388. https://doi.org/10.1201/9781003316404


*Conference paper (No Peer review)*

山野井悠翔, 前川宏一, 2018. 断層の直撃を受ける RC 構造の損傷モードと人工岩盤による損傷制御の可能性. *土木学会年次学術講演会講演概要集 73*.

山野井悠翔, 松尾豊史, 山口和英, 島村真介, 2021. 実規模解析による立坑を有する地中 RC ダクトの逆断層変位作用に対する損傷評価. *土木学会年次学術講演会講演概要集 76*.

山野井悠翔, 前川宏一, 2022. 断層変位を受ける地中 RC 構造物に対する人工軟岩材料の損傷抑制効果. *土木学会年次学術講演会講演概要集 77*.

# Appendix A: Stiffness of Cracked Concrete Derived from the Original Concrete Model

Regarding to the uncracked concrete, the original concrete model is based on the continuum mechanics and the three-dimensional elasto-plastic fracture model is adopted. In this state, the concrete deformation is divided into the volumetric part and deviatoric part and expressed as,

$$\sigma_{ij} = \delta_{ij} I_1/3 + s_{ij} = 3K_0 \varepsilon_{em} \delta_{ij} + 2G_0 K e_{eij} \qquad (A-1)$$

where, $K_0, G_0$ are the initial volumetric and shear stiffness; $K$ is the fracture parameter. The first term on the right side represents the volumetric component, and the second term represents the deviatoric one. As is clear from the equation, fracture is considered only in the latter, which represents resistance to changes in shape. In the proposed transition model, both the volumetric and deviatoric stress of gravels are added as the fracture parameter decreases. If the fracture function is set as Eq. (2-6), the deviatoric stress component shifts smoothly from concrete part to the sand part as,

$$s_{ij} = K \cdot s_{cij} + (1-K) \cdot s_{sij}, \qquad s_{cij} = 2G_0 e_{eij} \qquad (A-2)$$

where, $s_{ij}$ is the total deviatoric stress tensor; $s_{cij}, s_{sij}$ are the deviatoric tensor of concrete and sand part. On the other hand, as mentioned in **Chapter 2,** the volumetric stiffness increases when the fracture progresses.

After cracking, cracked concrete stress is calculated based on the local crack coordinate systems as illustrated in Fig. 2-6. Here, the orthogonal direction of the active crack plane is defined as x-axis, and y and z axis are allocated in the parallel direction. In the one-way cracking state, uniaxial compression-tension model is applied to the x-x component and the two-dimensional continuum elasto-plastic fracture model developed for concrete panels is applied to the y-y, z-z and y-z components. Shear transfer model gives the x-z and x-y components. In this anisotropic stage, the stiffness matrix becomes complex, and the volumetric stiffness is also no longer preserved.

When cracks occur in multi-directions, normal stresses (x-x, y-y and z-z components) are calculated assuming the uniaxial stress condition and expressed as,

$$\sigma_{ij} = E_0 K \omega_{ik} \varepsilon_{eki}, \qquad i,j,k \in \{x,y,z\}, \qquad i=j \qquad (A-3)$$

where, $\omega_{ij}$ is the reduction factor, which is the function of the largest tensile strain experienced in the past in the direction orthogonal to the crack plane. In the case of three dimensions, there are two orthogonal directions to one crack axis. The reduction factor representing one crack axis is represented by the geometric mean of the two. For example, the reduction factor for x-x direction is calculated as,

$$\omega_{xx} = \sqrt{\omega(\varepsilon_{ty,max}) \cdot \omega(\varepsilon_{tz,max})} \qquad (A-4)$$

where, $\varepsilon_{ty,max}$ and $\varepsilon_{tz,max}$ are the largest tensile strain experienced in the past in the direction y-y and z-z, respectively. Here, $\omega_{ij}$ $(i \neq j)$ is zero. In an isotropic compression stress and strain field, the following relationship holds.

$$I_1/3 = \frac{\sigma_{ii}}{3} = \frac{E_0 K}{3}(\omega_{ij} \varepsilon_{eij}), \qquad \varepsilon_{em} = \frac{\varepsilon_{eii}}{3} \qquad (A-5)$$

$$J_{2es} = 0, \qquad (1-\delta_{ij})\varepsilon_{eij} = 0 \qquad (A-6)$$

$$\sigma_{ij} = \sigma_{kl}, \qquad i=j, k=l \qquad (A-7)$$

Then, the following equation is derived from these relationships.

$$\varepsilon_{eij} = \sqrt{\frac{3|\omega_{kl}|}{\omega_{ij}\bar{\omega}}}\,\varepsilon_{em}, \qquad i = j, \qquad \bar{\omega} = \delta_{op}\omega_{op} \qquad (A-8)$$

where, $|\omega_{kl}|$ means the determinant of $\omega_{kl}$. By substituting Eq. (A-8) into Eq. (A-5), the following equation is obtained.

$$I_1/3 = E_0 K \sqrt{\frac{|\omega_{ij}|}{3\bar{\omega}}}\,\varepsilon_{em} \qquad (A-9)$$
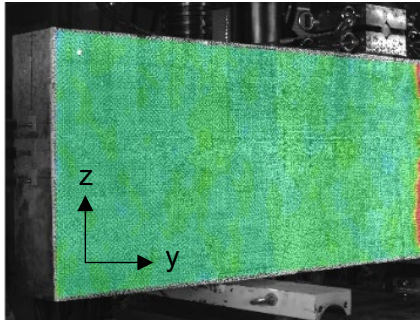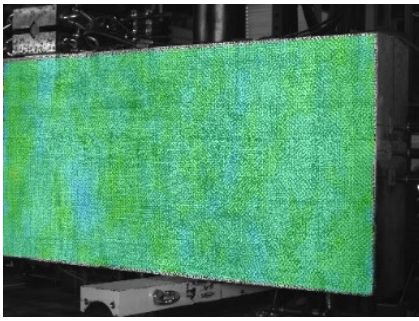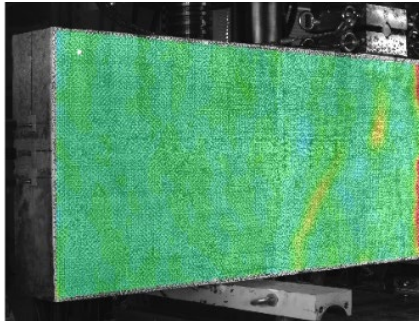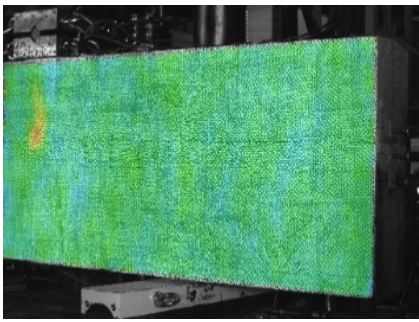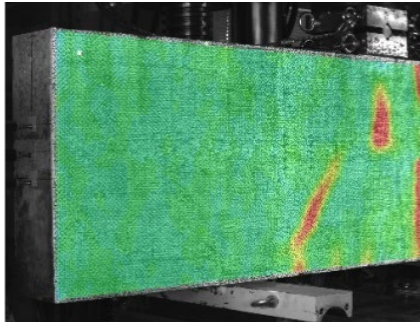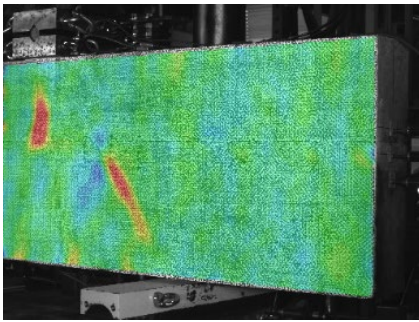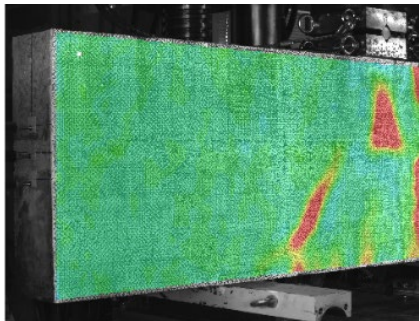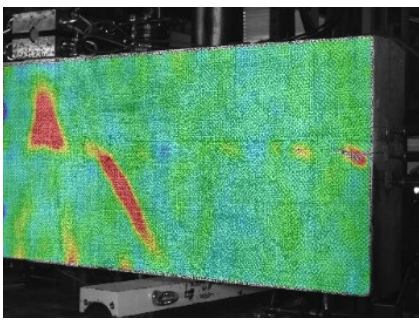
Finally, the volumetric stiffness of multi-directional cracked concrete cracked, $K_{o,crack}$, can be expressed as,

$$K_{0,crack} = E_0 K \sqrt{\frac{|\omega_{ij}|}{3\bar{\omega}}} \qquad (A-10)$$

Strictly speaking, the volumetric stiffness does not exactly match the value calculated by Eq. (A-10) because re-contact stress at the crack surface is also considered in the original model. However, there is a consistent tendency for volume stiffness to decrease as fracture parameters decrease. Shear stiffness also has a positive correlation with fracture parameters as it did before cracking. Therefore, in the transition model, both shear and volumetric stiffness shift from the material properties of concrete to that of sand according to the fracture parameter.

# Appendix B: The Strain Distributions Obtained from the Digital Image Correlation in the Experiment of Multi-Layer Composite Beams
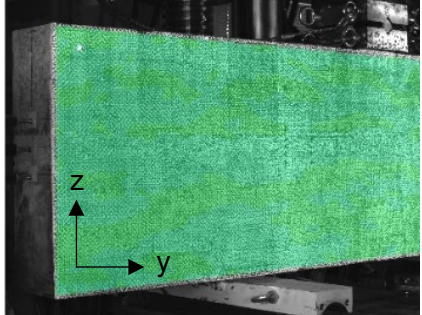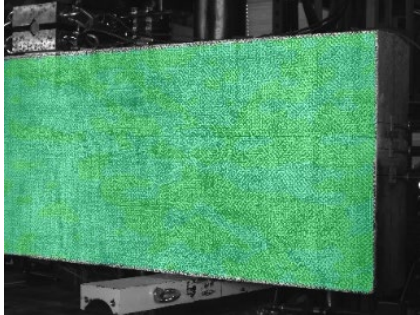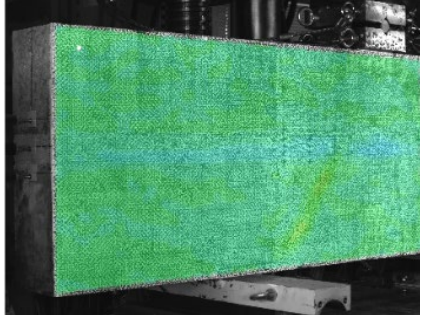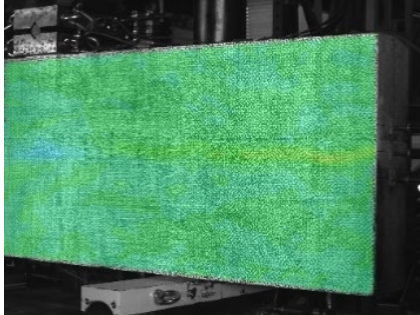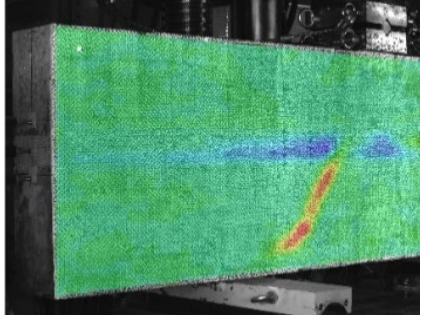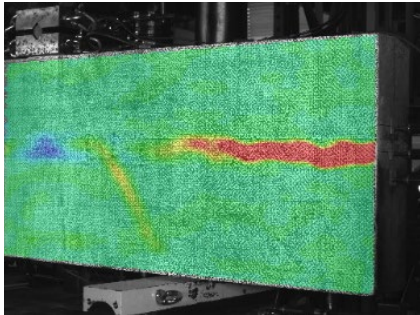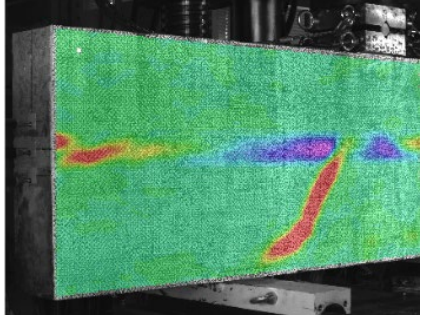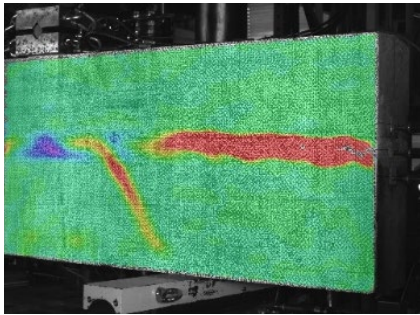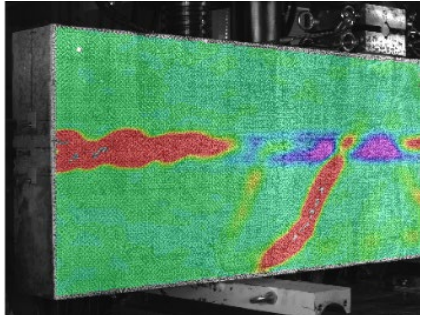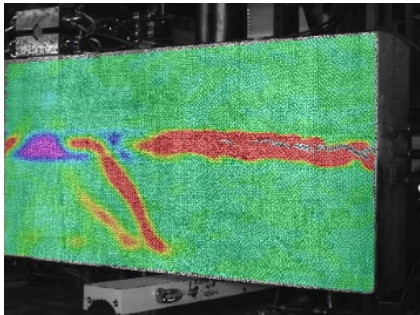
Here, the fracture process of the specimen predicted from the strain distribution obtained by the image correlation method is summarized. The results of FL-2C are shown in Fig. B-1 - B-3.

| Load | Left span | Right span | Memo |
|------|-----------|------------|------|
| 100 kN |  |  | - |
| 200 kN |  |  | Bending cracks in the normal strength layer and shear cracks in the high strength layer of the left span occurred. |
| 300 kN |  |  | Diagonal cracks also occured in the high-strength layer of the right span. |
| 400 kN |  |  | Weak layer damage was observed at the edges. |

| | | | |
|---|---|---|---|
| 500 kN |  |  | New diagonal cracks occured in the high-strength layer, and in the normal-strength layer of the left span. |
| 600 kN |  |  | - |
| 700 kN |  |  | - |
| 708 kN |  |  | Maximum load |

**Fig. B-1  The distribution of axial strain:$\varepsilon_{yy}$ in the case of FL-2C (Max: 0.5%, Min: -0.5%)**

| Load | Left span | Right span | Memo |
|------|-----------|-----------|------|
| 100 kN |  |  | - |
| 200 kN |  |  | Compressive strain was accumulated in the weak layer, and diagonal cracks occured in the left span. |
| 300 kN |  |  | An opening was observed in the weak layer at the end of the right span. Diagonal cracks also occured in the right span. |
| 400 kN |  |  | Compressive strain was accumulated inside diagonal cracks. |
| 500 kN |  |  | New diagonal cracks occured in the high-strength layer. |

| | | | |
|---|---|---|---|
| 600 kN |  |  | - |
| 700 kN |  |  | - |
| 708 kN |  |  | Maximum load |
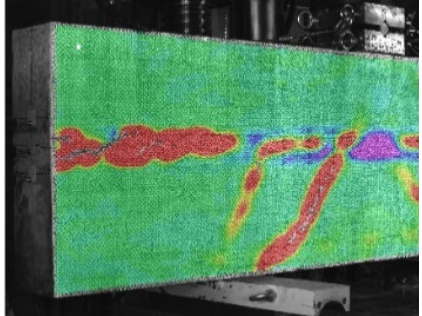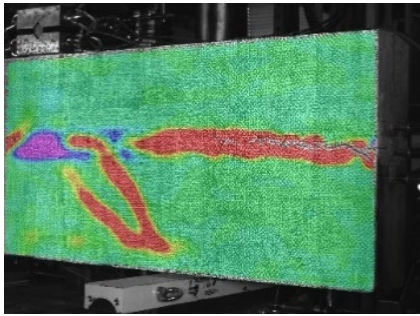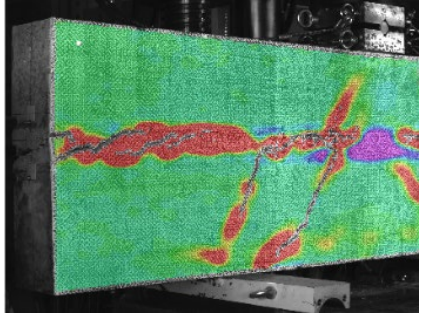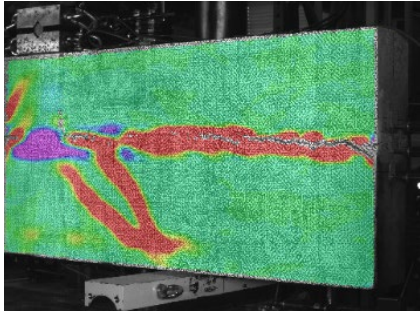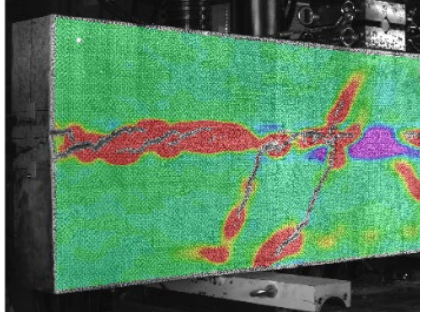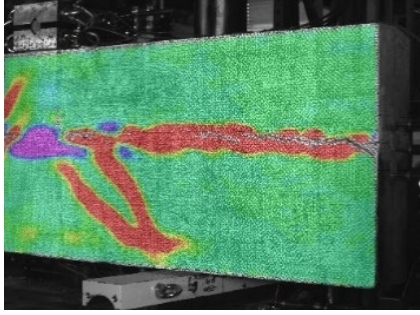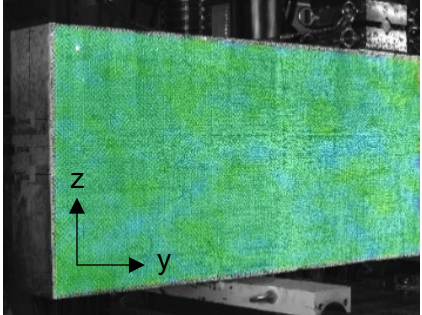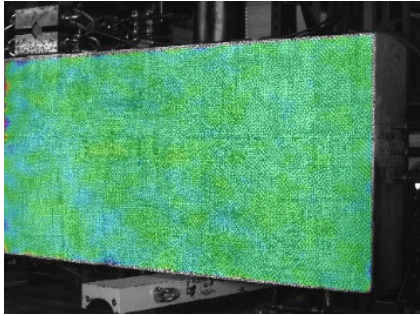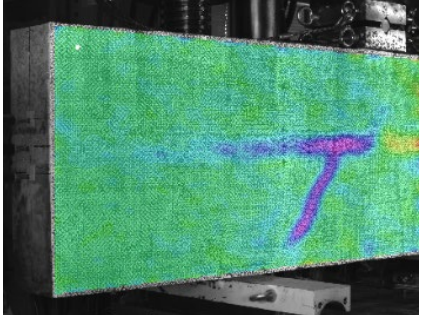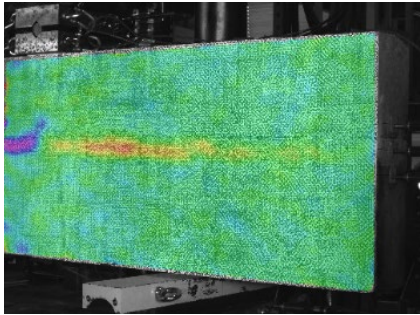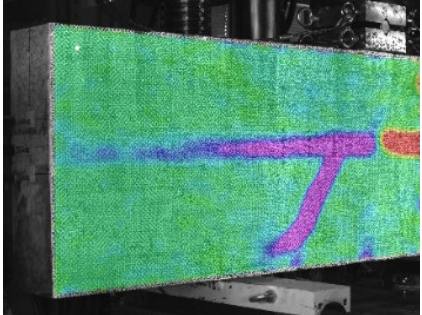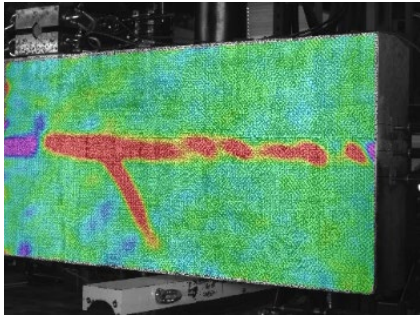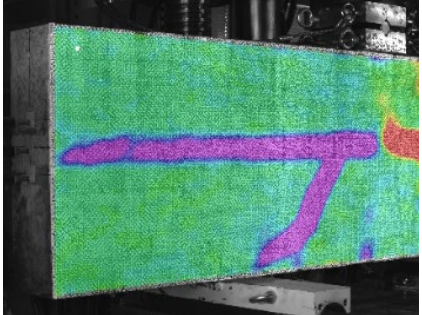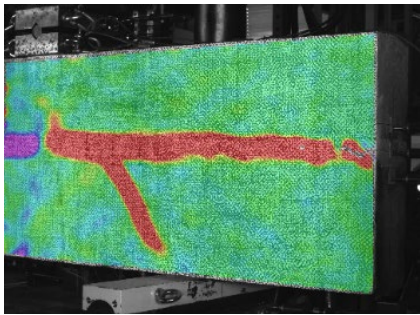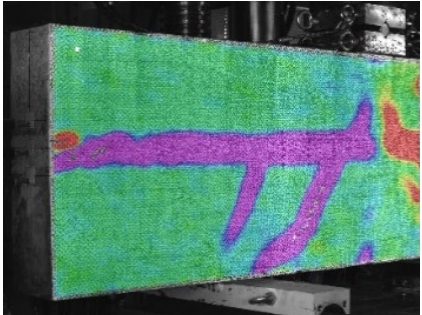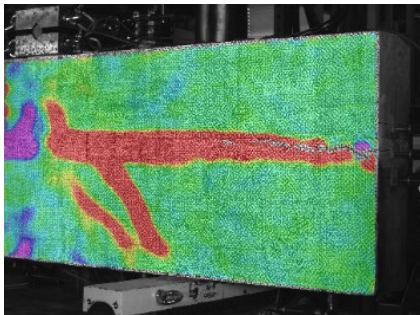
**Fig. B-2    The distribution of axial strain:$\varepsilon_{zz}$  in the case of FL-2C (Max: 0.5%, Min: -0.5%)**

| Load | Left span | Right span | Memo |
|---|---|---|---|
| 100 kN | | | - |
| 200 kN | | | Shear strain was accumulated in the weak layer, and diagonal cracks occured in the high-strength layer of the left span. |
| 300 kN | | | Diagonal cracks also occured in the high-strength layer of the right span. |
| 400 kN | | | - |
| 500 kN | | | New diagonal cracks occured in the high-strength layer. |

| | | | |
|---|---|---|---|
| 600 kN |  |  | - |
| 700 kN |  |  | - |
| 708 kN |  |  | Muximum load |
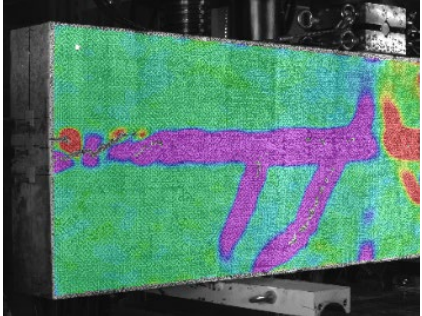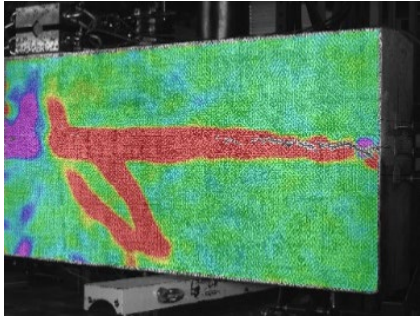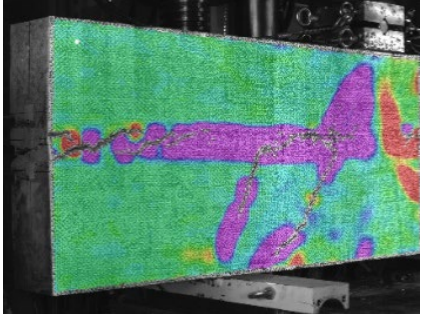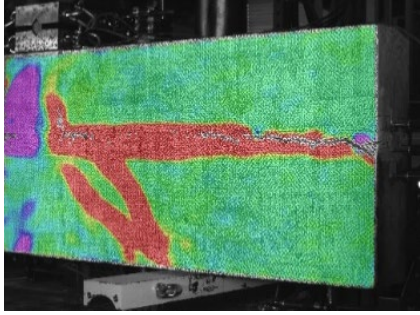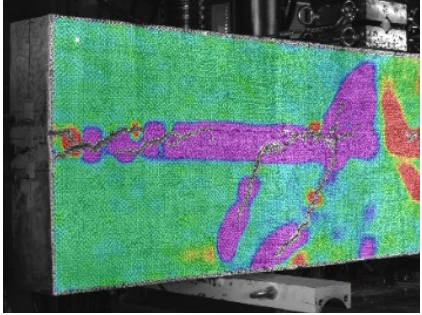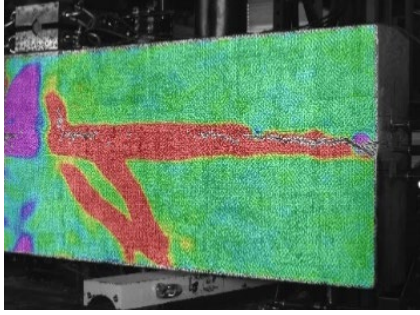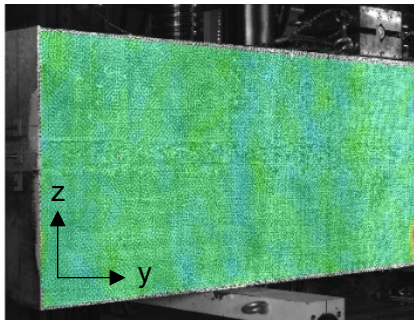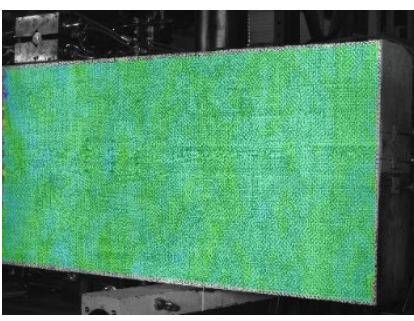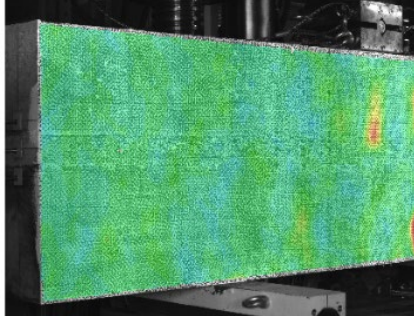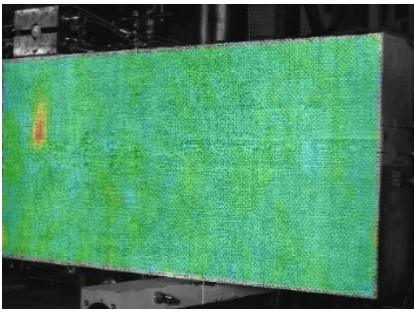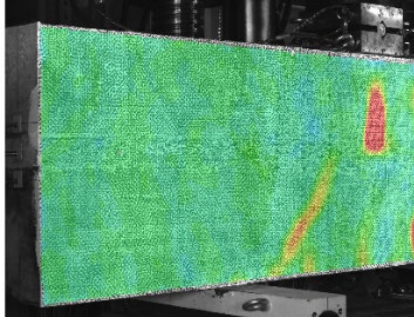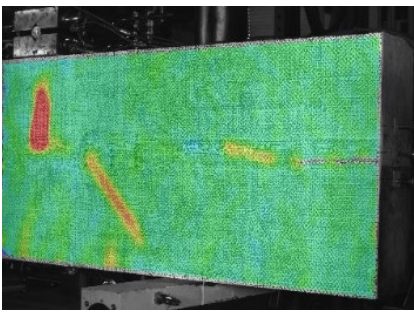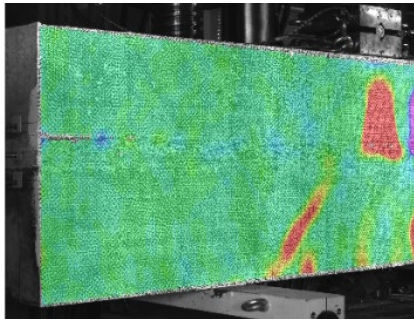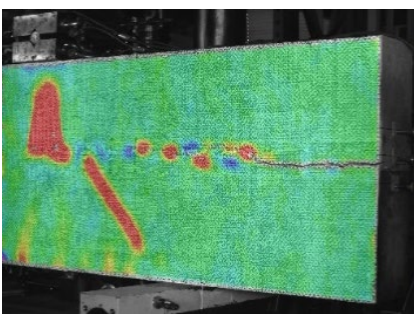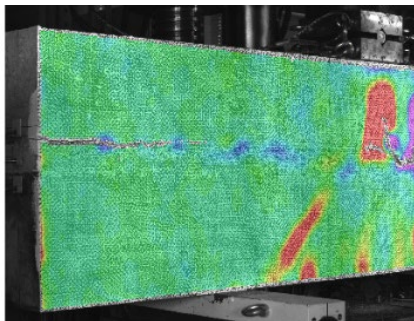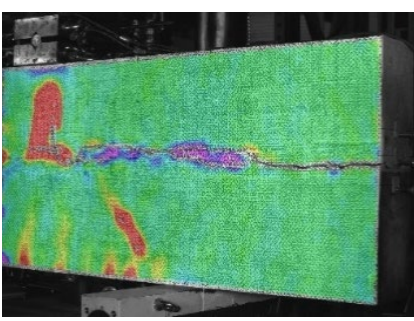
**Fig. B-3    The distribution of shear strain:$\varepsilon_{yz}$ in the case of FL-2C (Max: 0.2%, Min: -0.2%)**

The results of FL-2M are shown in Fig. B-4 – B-6.

| Load | Left span | Right span | Memo |
|---|---|---|---|
| 100 kN |  |  | |
| 200 kN |  |  | Bending cracks occured in the normal strength layer. |
| 300 kN |  |  | Diagonal cracks occurred in the high-strength layer, and damage to the weak layer was observed at the end of the right span. |
| 400 kN |  |  | Damage to the weak layer was also observed at the left end, and bending cracks were dispersed in the high-strength layer. |
| 500 kN |  |  | - |

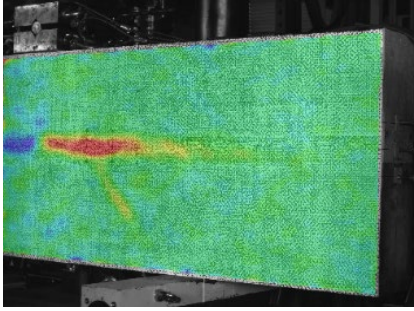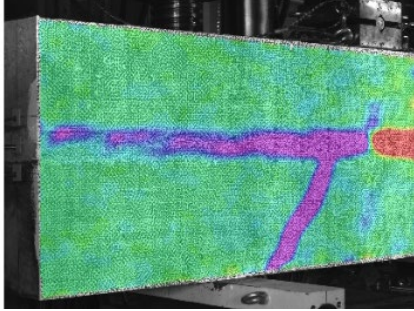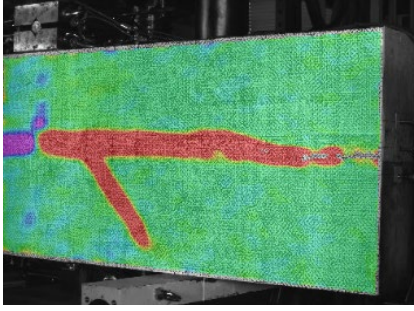| Load | Left span | Right span | Memo |
|------|-----------|-----------|------|
| 525 kN |  |  | Maximum load |
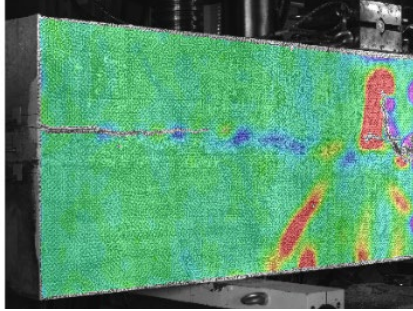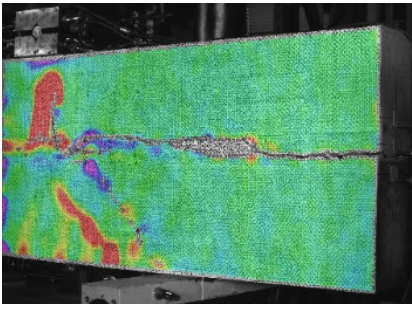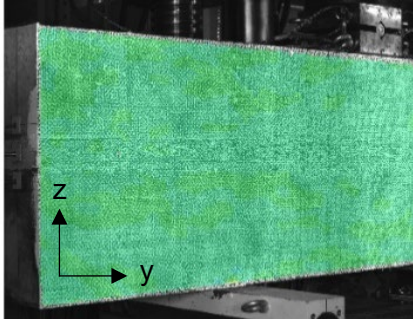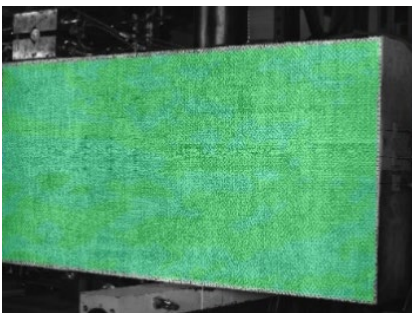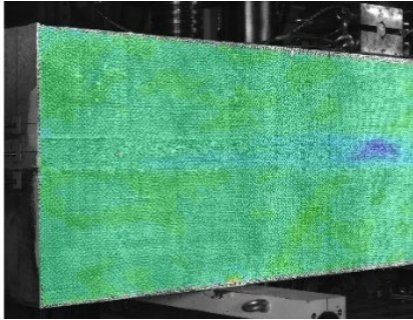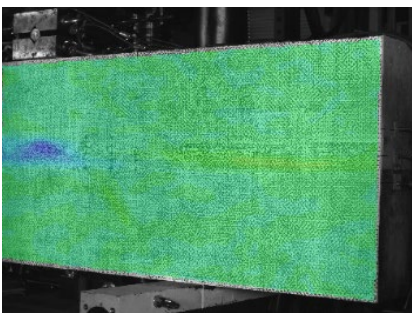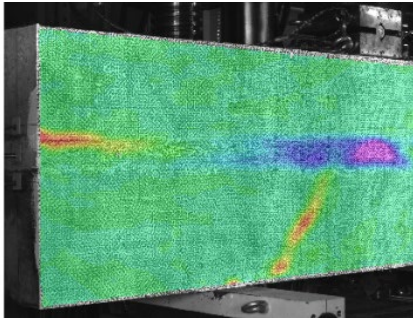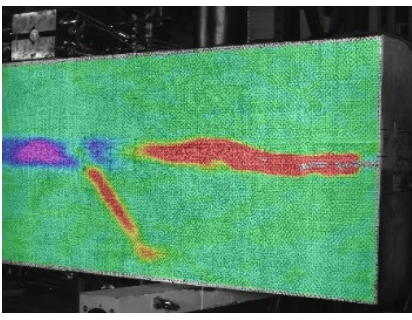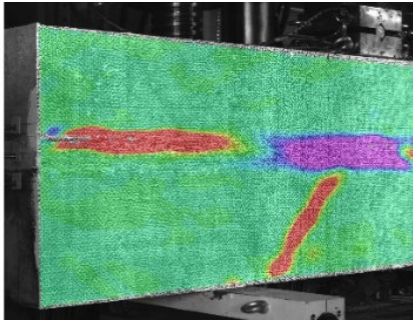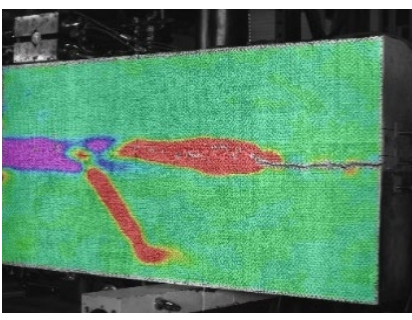
**Fig. B-4    The distribution of axial strain:$\varepsilon_{yy}$ in the case of FL-2M (Max: 0.5%, Min: -0.5%)**

| Load | Left span | Right span | Memo |
|------|-----------|-----------|------|
| 100 kN |  |  | - |
| 200 kN |  |  | Compressive strain was accumulated in the weak layer. |
| 300 kN |  |  | An opening was observed in the weak layer. Diagonal cracks occurred in the high strength layer. |
| 400 kN |  |  | The area of compressive strain expanded in the weak layer. |

| Load | Left span | Right span | Memo |
|------|-----------|-----------|------|
| 500 kN | | | - |
| 525 kN | | | Maximum load |
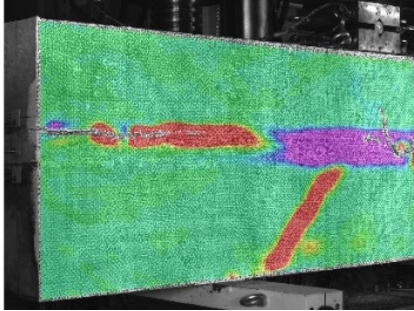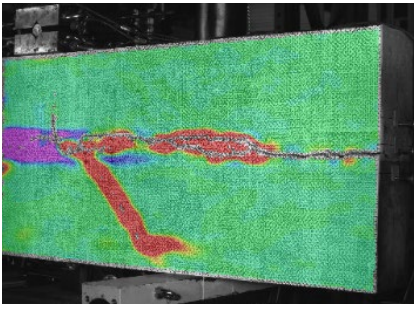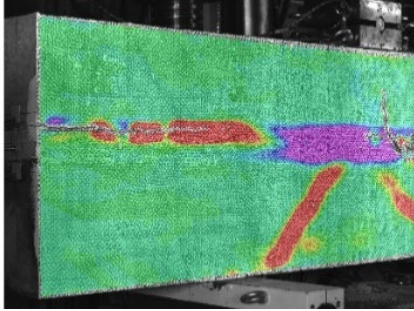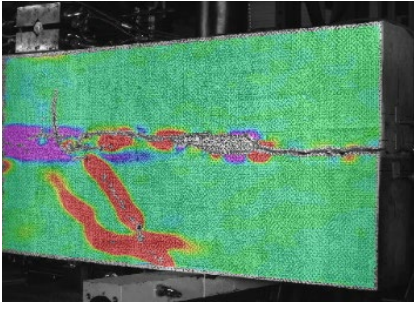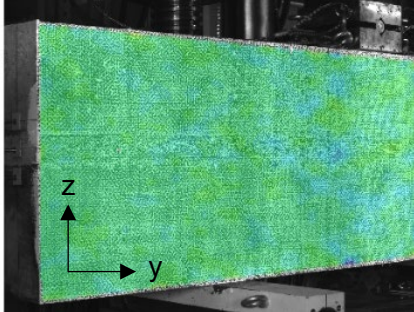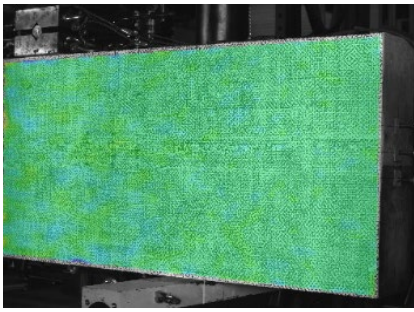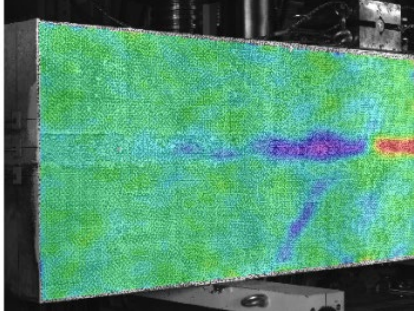
Fig. B-5    The distribution of axial strain:$\varepsilon_{zz}$  in the case of FL-2M (Max: 0.5%, Min: -0.5%)

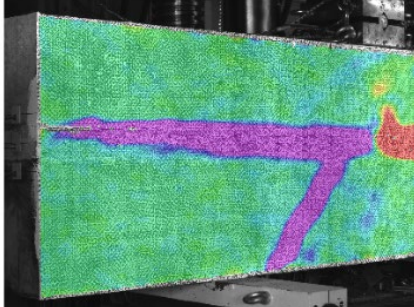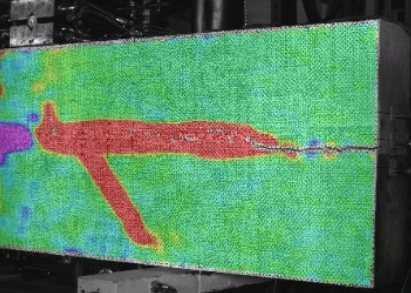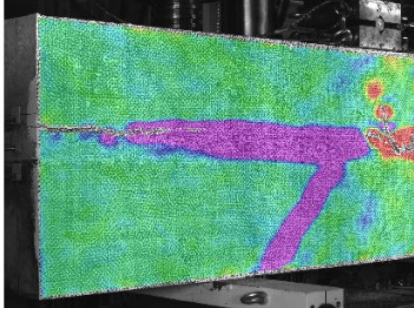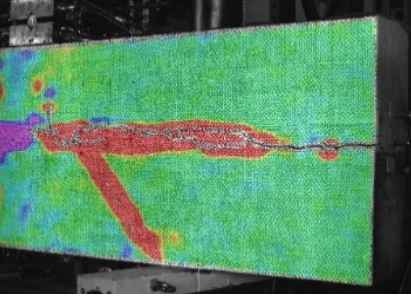| Load | Left span | Right span | Memo |
|------|-----------|-----------|------|
| 100 kN | | | |
| 200 kN | | | Shear strain was accumulated in the weak layer, and diagonal cracks occurred in the high-strength layer. |
| 300 kN | | | - |

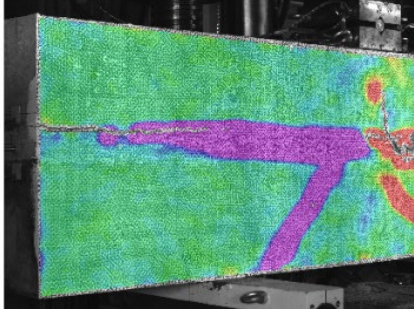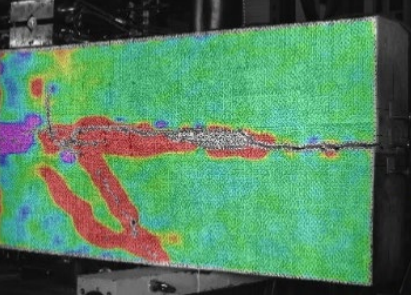| | | | |
|---|---|---|---|
| 400 kN |  |  | - |
| 500 kN |  |  | - |
| 525 kN |  |  | Maximum load |

**Fig. B-6    The distribution of shear strain:$\varepsilon_{yz}$  in the case of FL-2M (Max: 0.2%, Min: -0.2%)**